National Library of Canada

Acquisitions and Bibliographic Services Branch

395 Wellington Street
Ottawa, Ontario
K1A 0N4

Bibliothèque nationale du Canada

Direction des acquisitions et des services bibliographiques

395, rue Wellington
Ottawa (Ontario)
K1A 0N4

Your file Votre référence

Our file Notre référence

NOTICE

The quality of this microform is heavily dependent upon the quality of the original thesis submitted for microfilming. Every effort has been made to ensure the highest quality of reproduction possible.

If pages are missing, contact the university which granted the degree.

Some pages may have indistinct print especially if the original pages were typed with a poor typewriter ribbon or if the university sent us an inferior photocopy.

AVIS

La qualité de cette microforme dépend grandement de la qualité de la thèse soumise au microfilmage. Nous avons tout fait pour assurer une qualité supérieure de reproduction.

S'il manque des pages, veuillez communiquer avec l'université qui a conféré le grade.

La qualité d'impression de certaines pages peut laisser à désirer, surtout si les pages originales ont été dactylographiées à l'aide d'un ruban usé ou si l'université nous a fait parvenir une photocopie de qualité inférieure.

Canada

The Quantum Confined Stark Effect and Wannier Stark Ladders in $In_xGa_{1-x}As$ Quantum Wells and Superlattices

Kevin Gibb

A thesis submitted to the Faculty of Graduate Studies and Research in partial fulfillment of the requirements for the degree of Doctor of Science in Physics

Department of Physics
University of Ottawa
150 Louis Pasteur
Ottawa, Ontario
K1N 6N5

ISBN 0-315-80046-1

UNIVERSITÉ D'OTTAWA
UNIVERSITY OF OTTAWA

Abstract

The effects of an applied bias in the longitudinal or growth direction on four $In_xGa_{1-x}As$-GaAs strained single quantum wells and three strained layer superlattices have been studied using photocurrent and electroreflectance spectroscopy at liquid helium temperature. Weak applied electric fields on the quantum well samples gives rise to a red quadratic shift to the lowest interband transition between the first confined electron (E1) and heavy-hole (H1) levels, the quantum confined Stark effect (QCSE). The magnitude of the QCSE increases with well width. This field dependence becomes subquadratic at high applied fields due to carrier accumulation on the low energy side of the wells.

Superlattices with relatively small periods, ie. 10 nm, exhibit interwell coupling giving rise to a miniband structure under flatband conditions. The application of an electric field removes the interwell coupling giving rise to a ladder like progression in energy for the interband transition energies, called Wannier Stark ladders. The measured exciton transition energies follow a linear field dependence given by the product of the Stark ladder index, the superlattice period, and the electric field. The low field behaviour is more complex due to the Coulomb interaction between the electrons and heavy-holes.

The measured field dependent exciton transition energies for the quantum wells agree well with single particle model calculations, while for the superlattice samples the exciton Stark ladder calculations of Dignam and Sipe have yielded good agreement with the measured data.

Acknowledgments

The research carried out in this study involved the efforts of many people, without whose help, this study would not have been completed. I wish to acknowledge their contributions.

A.P. Roth and C. Lacelle for growing the $In_xGa_{1-x}As$-GaAs quantum well and superlattice samples used in this study.

P. Maigne, Z. Wasilewski, and A.P. Roth for performing and analyzing the x-ray diffraction measurements on the superlattice samples.

Q. Sun and M. Buchanan for processing the grown wafers into pin diode structures for both the quantum well and superlattice samples.

M.M. Dignam and J. Sipes for performing their exciton Stark ladder calculations for two of our samples.

G. Aers for lending me his numerical integration program, teaching me how to use it, and showing no end of patience when I called on for help.

A.P. Roth and E. Fortin for giving me a free reign in their labs in which to carry out my experiments, and providing the guidance necessary to see this work to fruition.

Financial support was generously provided by E.Fortin and A.P. Roth through NSERC grants.

Finally, I wish to thank Dr. Peter Dawson, Director Institute for Microstructural Science, NRC, for permitting me to work at the NRC laboratories, as well as providing financial support.

Table of Contents

Abstract		i
Acknowledments		ii
Table of Contents		iv
List of Figures		viii
List of Tables		xiii
List of Symbols		xiv

Overview of Thesis

i-i	Introduction	1
i-ii	Quantum confined Stark effect	5
i-iii	Excitons	6
i-iv	Wannier Stark ladders	7
i-v	Experimental methods	9
i-vi	Motivation	11
i-vii	Summary of thesis	11
i-viii	Thesis outline	12

Chapter 1

Modelling of the Quantum Confined Stark Effect, Wannier Stark Ladders, and Exciton binding energies.

1-1	Introduction	14
1-2	Bandgaps	14
1-3	Krönig-Penney model	18

1-4	The transfer Matrix Method	21
1-5	Quantum confined Stark effect (QCSE)	23
1-5-1	Transfer matrix method applied to the quantum well	23
1-5-2	Transformed Hamiltonian (Airy functions)	26
1-5-3	Perturbation and variational methods for the infinite quantum well	27
1-5-4	QCSE for Finite quantum wells	29
1-6	Wannier Stark ladders	31
1-6-1	General solution for tight binding method	35
1-6-2	Tight binding model at zero field	37
1-6-3	Tight binding model for applied fields	38
1-7	Tight binding model - Stark ladder oscillator strengths	41
1-8	Numerical integration method	42
1-9	Coulomb interaction-exciton binding energies	45
1-10	Summary	50

Chapter 2

Experimental Methods and Samples

2-1	Samples	52
2-2	Optical measurements	57
2-3	Apparatus	60

Chapter 3

Experimental Results for the Quantum Wells

3-1	Introduction	66a
3-2	Field dependent quenching of PL intensity	66a
3-3	Photocurrent spectroscopy data	68
3-4	Zero field exciton binding energy	72
3-5	Electric field dependence-QCSE	74
3-6	Variational calculation of the QCSE	77
3-7	Numerical calculation of the QCSE	80
3-8	Calculated field dependent exciton binding energies	82
3-9	Summary	87

Chapter 4

Experimental Results for the Superlattices

4-1	Introduction	88
4-2-1	Low field spectra for sample L121	91
4-2-2	Low field spectra - H145 and L073	95
4-3	Field dependent spectra - Wannier Stark ladders	99
4-3-1	PC and ER field dependent spectra for sample L121	99
4-3-2	PC and ER field dependent spectra for H145	103
4-3-3	PC and ER field dependent spectra for L073	106
4-4	Calculated Stark ladder intensities	109
4-5	Description of the measured field dependent Stark ladder energies	114
4-6	Calculated Stark ladder structures - single particle model	118
4-6-1	Electron Stark ladders	119

4-6-2	Heavy-hole ladders	122
4-7	Comparison between calculated interband and measured exciton transition energies	124
4-8	Calculation of the oblique exciton binding energy	126
4-9	Summary	128

Chapter 5

5-1	Exciton Stark ladders.	130
5-2	The peaks A and A'	135
5-3	End effects	136
5-4	Surface effect	137
5-5	Tamm states	139
5-6	Summary	142

Conclusions 144

References 147

List of Figures

Figure 1. Periodic potential for the $In_xGa_{1-x}As$-GaAs superlattice. 2

Figure 2. E-K miniband diagram for an $In_xGa_{1-x}As$-GaAs superlattice. 3

Figure 3. Single quantum well and eigenstates. 4

Figure 4. Photoluminescence of quantum well interband transition energies. A) Excitation and emission from quantum well. B) Spectral distribution of PL peak. C) Quadratic Stark shifting due to applied field. 6

Figure 5. A) Superlattice at zero field showing interwell coupling. B) Stark localization due to applied field. 8

Figure 6. A) Conduction and valence band profile for quantum well. B) Potential profile for superlattice. Several eigenstates are also indicated. 17

Figure 7. A) Quantum well under bias with potential steps used for transfer matrix calculations. B) Biased QW is the sum of isolated quantum well potential, and electric field perturbation. 24

Figure 8. The superlattice potential with an applied field A) may be expressed as the sum of the staircase potential B) and a triangle potential C). 34

Figure 9. Depiction of Wannier functions $|\Phi_n>$, and superlattice potential V_c. 36

Figure 10. $Al_xGa_{1-x}As$-GaAs superlattice with incident, reflected and transmitted wave functions. This arrangement is used in the numerical integration program. 43

Figure 11. A) Schottky diode structure. B) pin diode structure. 53

Figure 12. Photocurrent spectroscopy apparatus. 63

Figure 13. Electroreflectance apparatus. 64

Figure 14. Field induced quenching of PL intensity, and calculated electron tunnelling lifetimes. 68

Figure 15. Measured photocurrent spectra for M051 at increasing applied fields. 71

Figure 16. Exciton binding energies for $In_{.125}Ga_{.875}As$ quantum wells calculated using the variational function (equ. 56). 74

Figure 17. Measured exciton transition energies (symbols) and numerically calculated interband transition energies for the four $In_xGa_{1-x}As$-GaAs quantum wells M049-M052. 76

Figure 18. Variational Calculation of the QCSE for the four $In_xGa_{1-x}As$-GaAs single quantum wells using a linear prefactor (solid lines) and exponential prefactor (dotted lines). Only the well material parameters have been used where $m_e = .0663m_0$, $m_h = .346m_0$, $V_c = 93.3$ mV, $V_h = 49.7$ meV. 79

Figure 19. Exact numerical calculation of the QCSE for the four quantum wells. Both the well and barrier material parameters have been used to calculate these curves. Well depths and masses are the same as in Figure 18. Barrier

masses are now .0665 and .370m_0 for the electrons and heavy-holes respectively. 82
Figure 20. Calculated field dependent reduction to exciton binding energies for the $In_xGa_{1-x}As$-GaAs quantum wells. Calculations using linear prefactor are plotted as dashed lines, while results obtained with exponential prefactor are represented by the solid lines. 84
Figure 21. Measured and calculated exciton transition energies for the 5.5, 7.5 and 10 nm wide $In_xGa_{1-x}As$-GaAs quantum wells. 86
Figure 22. Energy diagram for L121 including observed interband transitions. 89
Figure 23. Superlattice potentials and interband transitions for A) H145, B) L073. 90
Figure 24. PL, PLE, PC, and ER spectra for L121. 93
Figure 25. Low field PC and ER spectra for H145. 96
Figure 26. Electroreflectance and photocurrent spectra for L073 taken near flatband conditions. 98
Figure 27. PC spectra for L121 versus applied bias. Bias steps are every 0.2V. 101
Figure 28. Bias dependence of ER spectra for L121 showing formation of Wannier Stark ladders. 102
Figure 29. Bias dependent photocurrent spectra for H145. Bias increment is 0.25V. 104
Figure 30. Bias dependence of ER spectra for H145. 105
Figure 31. Photocurrent spectra for L073. Bias increment is 0.2V. 108
Figure 32. Bias dependent electroreflectance spectra for L073. 109

Figures 33-35. Calculated oscillator strengths for the p=0,1 and 2 Stark ladders. Top previous page (fig. 33) L121, bottom of previous page (fig. 34) H145, above (fig. 35) L073. 112

Figures 36 and 37. Calculated interband transition energies (solid curves), and measured exciton transition energies for L121 in figure 36 previous page, and H145 figure 37 above. 117

Figure 38. Measured Stark ladder exciton transition energies (symbols) and calculated Stark interband transition energies (solid lines) for L073. 118

Figure 39. Calculated Wannier Stark ladder for electron levels in a five period superlattice. Transfer matrix calculations are plotted as solid lines, while tight-binding results are given by dashed lines. The bottom of the well is taken to be at 0 meV 121

Figure 40. Calculated electron Stark ladders for the 11 well structure. 122

Figure 41. Calculated heavy-hole Wannier Stark ladder using transfer matrix method. The bottom of the well is at 0 meV. 123

Figure 42. Calculated 'oblique' exciton binding energy versus superlattice period. 127

Figure 43. Plot of exciton Stark ladders for L121. Symbol size indicates relative Stark ladder oscillator strength. 133

Figure 44. Plot of exciton Stark ladders for H145. 134

Figure 45. End quantum well potential profile used to calculate effects of thick barrier width. Barrier height is 95.6 meV for H145. 137

Figure 46. Potential profile used to calculate the effects of a surface potential such as from a gold front contact. Calculations are performed as a function of the surface potential $V_{surface}$ for two GaAs cap layer thicknesses, 9 and 18 nm. 138

Figure 47. Calculated E1 quantum well eigenstate energy for the end quantum well as a function of the surface potential. A) 18 nm wide GaAs cap layer, B) 9 nm wide cap layer. C) 5 nm wide cap layer. 139

Figure 48. Potential profile used to calculate the effects of a Tamm state embedded at the $In_xGa_{1-x}As$-GaAs interface for L121. 141

Figure 49. Effect of a Tamm state potential on the E1 quantum well energy for L121. A) 0.1 nm, B) 0.2 nm, C) 0.5 nm Tamm state width. 142

List of Tables

Table 1.	Quantum well Structures, as fitted from PC data.	54
Table 2.	Superlattice Structures	55
Table 3.	Summary of Wafers Studied	65
Table 4	Exciton and Interband Transition Energies for L121 in meV.	94
Table 5	Exciton and Interband Transition Energies for H145. Calculations performed for $In_{.125}Ga_{.875}As$ with a 9 nm barrier and 2.5 nm well.	97
Table 6	Exciton and Interband Transition Energies for L073.	99

List of Symbols

a Well width, hydrostatic pressure shift, amplitude coefficient.

A Quantum well width, amplitude coefficient for wavefunction.

Ai(ξ) Airy function of argument ξ.

A_{well} Transfer matrix for well or barrier.

b Barrier width, uniaxial stress shift, amplitude coefficient.

B Barrier width, amplitude coefficient for wavefunction.

Bi(ξ) Airy function of argument ξ.

C Amplitude coefficient for wavefunction.

C_{ij} Elastic stiffness constants.

C_m Expansion coefficient.

d Superlattice period.

E Energy.

E_b Exciton binding energy.

E_g Energy gap of semiconductor.

E1 Energy of first electron eigenstate in quantum well.

E_{n0} Zero field eigenenergy for n^{th} eigenstate.

EΓ1 Energy at first electron miniband zone centre.

Eπ1 Energy at first electron miniband zone edge.

f Coefficient used in tight binding model.

f(z) quantum well wavefunction.

F Applied electric field.

h Planck constant.

H Hamiltonian.

$\mathbf{H}_1()$ Struve function.

H1 Energy of first heavy-hole eigenstate in quantum well.

HΓ1 Energy at first heavy-hole miniband zone centre.

Hπ1 Energy at first heavy-hole miniband zone edge.

$J_\rho()$ Bessel Function.

k_o Quantum well wavevector.

k_1 Wavevector.

$L\Gamma 1$ Energy at first light-hole miniband zone centre.

m Quantum well index for superlattice.

m_0 Electron rest mass.

m^* Effective mass of electron, heavy-hole, or light-hole.

m_a Effective mass in well layer

m_b Effective mass in barrier layer

n Quantum well index for superlattice.

N Total number of wells in superlattice.

$N_1()$ Neumann function.

$N(\beta)$ Normalizing coefficient.

p Quantum well index for superlattice, Stark ladder index.

P_x Momentum operator.

q Electron charge.

q_o Barrier wavevector.

R Reflectivity.

U(z) Periodic part of the Bloch function.

V Potential energy, voltage.

V_a Potential energy in well layer.

V_b Potential energy in barrier layer.

V_c Electron potential well depth.

V_h heavy-hole potential well depth.

x Alloy fraction, direction parallel to semiconductor surface.

y Alloy fraction, direction parallel to semiconductor surface.

$Y_\rho()$ Neuman function.

z Direction of growth of semiconductor epilayers.

α Absorption coefficient.

β Variational parameter.

Δ_{so} Spin orbit coupling to split-off band.

δE_H Hydrostatic pressure shift of semiconductor bandgap.

δE_u Uniaxial stress term.

δR Differential change in reflectivity.

ε Dielectric constant.

ε_{ij} Strain tensor elements.

κ Superlattice wave vector.

Γ Miniband Brillouin zone centre, lifetime broadening, parameter, Gamma function.

π Miniband Brillouin zone edge.

λ Variational parameter, 1/4 superlattice miniband-width.

$|\Psi\rangle$ Wavefunction.

$|\Phi\rangle$ Quantum well wavefunction, Wannier function.

θ Phase factor

ρ Radial extent of exciton, integer

μ Exciton reduced mass.

ν Photon frequency.

ω Angular frequency.

Overview of Thesis

i-i Introduction

This thesis reports on the study of the effects of a perturbing static electric field on the eigenstate energies of semiconductor quantum wells and superlattices. The quantum wells are an experimental realization of the particle in a box problem, while the superlattice provides an ideal Krönig-Penney type potential as discussed in many undergraduate text books in solid state physics or quantum mechanics. Not only can quantum structures be fabricated as desired, they can be probed by many techniques. Perturbation of their eigenstate energies can be easily achieved with electric or magnetic fields, while their responses can be measured via a number of electrical and optical probes.

The success of this is due to the ability to control the growth of semiconductor epilayers to within a monolayer of thickness, and alloy composition to better than 0.5%. This is a result of the development of molecular beam epitaxy (MBE), metalo-organic vapour phase epitaxy (MOVPE), and associated growth techniques over the last 20 years. Structures have been fabricated from numerous semiconductor families including; binaries such as AlAs-GaAs, ternaries which include $Al_xGa_{1-x}As$-GaAs, $In_xGa_{1-x}As$-GaAs and $In_xGa_{1-x}As$-InP, and even the quaternary $In_xGa_{1-x}As_yP_{1-y}$-InP.

The $In_xGa_{1-x}As$-GaAs strained layer structures studied in this work were grown using a low pressure organometallic vapour phase epitaxy reactor (MOVPE) at the National Research

Council, Ottawa. A typical structure consists of a thick undoped GaAs layer deposited onto an n+ GaAs substrate. This is followed by thin alternating layers of $In_xGa_{1-x}As$ (wells) and GaAs (barriers), followed by a GaAs cap layer. Strain arises from the lattice mismatch between the bulk $In_xGa_{1-x}As$ and GaAs layers, with $In_xGa_{1-x}As$ having a larger lattice constant. For sufficiently thin layers, the $In_xGa_{1-x}As$ layer grows with the same in-plane (xy plane) lattice constant as the GaAs layer, the strain being accommodated by an elongation of the $In_xGa_{1-x}As$ lattice constant in the perpendicular or z direction. This strain modifies the band structure of the $In_xGa_{1-x}As$ layer giving rise to distinct optical and electrical features.

The designation of well and barrier arises from the GaAs and $In_xGa_{1-x}As$ bandgaps. The heavy-hole bandgap for the strained $In_xGa_{1-x}As$ layer is less than that of the unstrained GaAs layer, creating $In_xGa_{1-x}As$ quantum wells and GaAs barriers. A periodic potential is depicted in figure 1 where the A layer represents the $In_xGa_{1-x}As$ wells, and B the GaAs barriers.

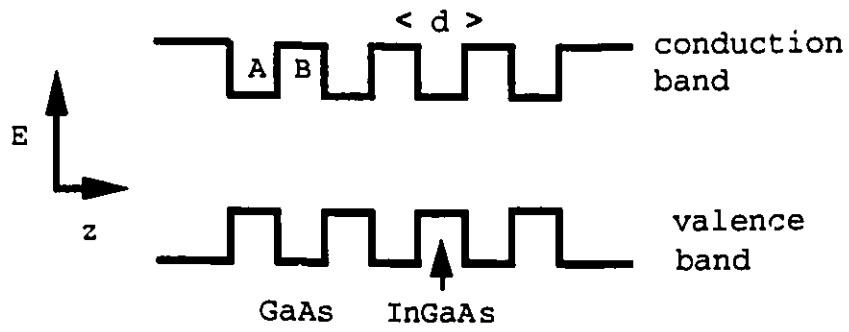

Figure 1. Periodic potential for $In_xGa_{1-x}As$-GaAs superlattice.

This profile is similar to the periodic atomic potential of the host semiconductor materials $In_xGa_{1-x}As$ and GaAs which gives rise to the bulk semiconductor band structures. However, structures such as the $In_xGa_{1-x}As$-GaAs superlattice are periodic in the one direction only (z or growth direction), so that their miniband structures can be easily modeled by the one dimensional Krönig-Penney model. Furthermore the 'lattice' constant (d) is now on the order of 10 nm with potential wells on the order of 100 mV. This gives rise to a series of minibands for the conduction and valence bands depicted below in figure 2.

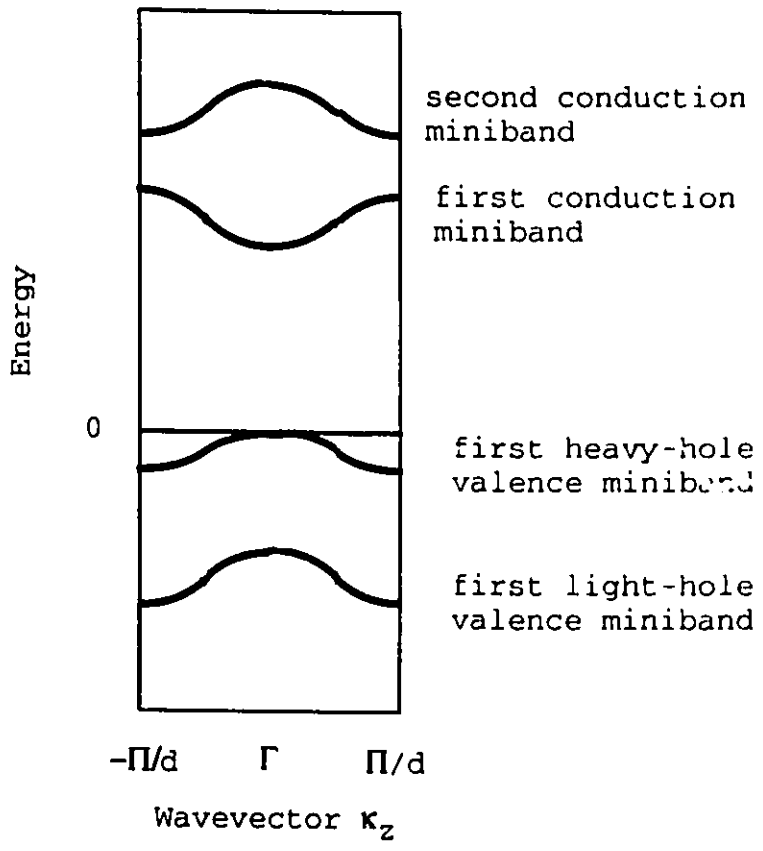

Figure 2. E-K miniband diagram for an $In_xGa_{1-x}As$-GaAs superlattice.

The finite quantum well can be thought of as a superlattice with infinite barrier widths. In practice the quantum wells can be realized by using wide barriers (greater than 50 nm) to decouple adjacent wells, as in multi-quantum wells. This causes the minibands to coalesce into a series of discrete eigenstate energies. Alternately a single well can be fabricated. The eigenstate energies can be calculated using the Krönig-Penney model with infinite barrier width, or solving for the particle in a finite quantum well problem. In both cases a series of eigenstate energies is obtained for the conduction and valence band wells, as depicted below in figure 3.

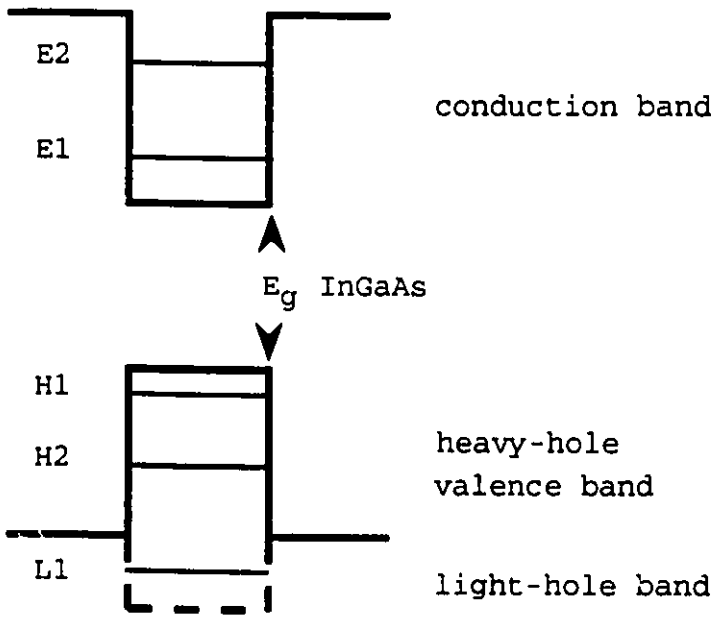

Figure 3. Single quantum well and eigenstates.

i-ii Quantum confined Stark effect

The application of a static electric field in the longitudinal (z or growth) direction of the single quantum well tilts its potential profile. The average potential of the quantum well remains constant, yet the electron and hole wavefunctions are red shifted to lower energy levels. This effect is termed the quantum confined Stark effect (QCSE) and is similar to the field induced Stark effect of the hydrogen atom. The magnitude of the Stark effect is greatly enhanced by the wide quantum well structures.

The energy shift is quadratic with respect to the applied electric field at weak and moderate field strengths. Carrier accumulation on the low energy sides of the quantum wells at large applied fields causes the energy shift to be less than quadratic. Early measurements of electric field dependent photoluminescence (PL) from $Al_xGa_{1-x}As$-GaAs quantum wells by Mendez et al. [1] hinted at this quadratic field dependence. The PL experiment involves optically exciting excess carriers into the quantum wells and measuring the spectral distribution of the emitted luminescence (PL). The peak intensity in the PL spectra gives a measure of the semiconductor bandgap plus quantum well energies, less the exciton binding energy. This experiment is depicted schematically below in figure 4. Absorption measurements performed by Miller et al. [2] also revealed a strong quadratic shift for an $Al_xGa_{1-x}As$-GaAs quantum well. The Stark shift has also been demonstrated by Van Eck et al. [3] for an InGaAs-GaAs quantum well.

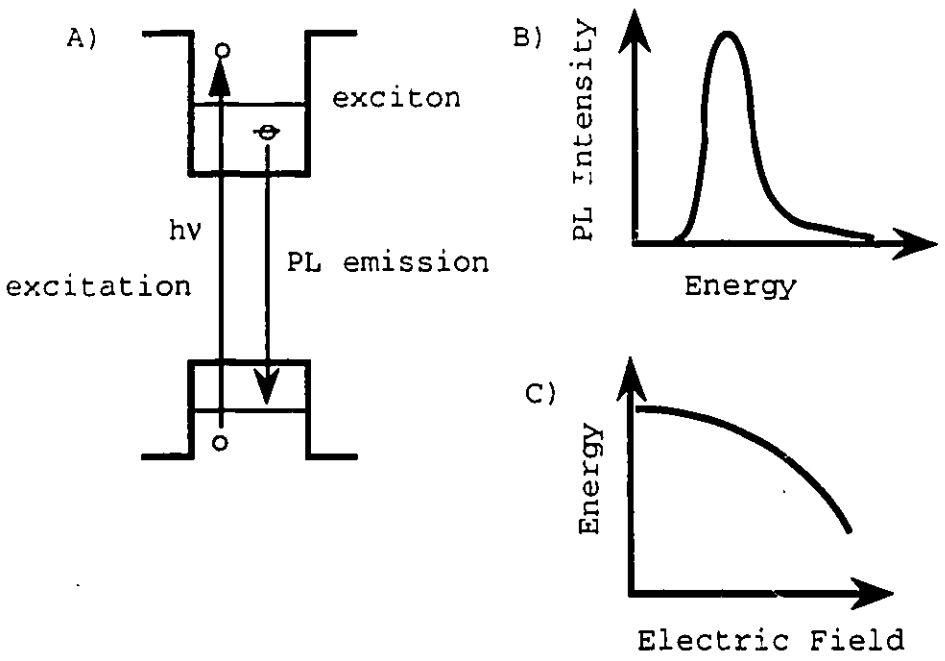

Figure 4. Photoluminescence of quantum well interband transition energies. A) Excitation and emission from quantum well. B) Spectral distribution of PL peak. C) Quadratic Stark shifting due to applied field.

i-iii Excitons

The free exciton arises from the Coulomb interaction between electrons in the conduction band and holes in the valence band. In bulk material the binding energy of the exciton may be calculated using the hydrogen atom model of a light electron orbiting around a massive hole. The free exciton in bulk $In_xGa_{1-x}As$ has a binding energy of about 3.5 meV. The confinement of the electrons and holes to the wells in quantum well structures increases this binding energy to about 8 meV. Other types of excitons include donor bound excitons, and acceptor bound excitons each with their own binding energy. The exciton binding energy is weakly reduced

by applied electric fields.

i-iv Wannier Stark ladders

At zero applied field the electrons and holes in the superlattice exist as extended states, giving rise to a miniband structure. The application of an electric field in the longitudinal or growth direction tilts the potential profile of the superlattice, causing the extended superlattice states to split into a series of quantum well like states, localised about each successive well. In the simplest tight-binding model these localised states are equivalent, though offset in energy by the average potential of each quantum well. This offset is determined by product of the applied electric field (F) and the superlattice period (d), ie. each state is separated in energy by qFd. The formation of the Wannier Stark ladders is depicted below in figure 5.

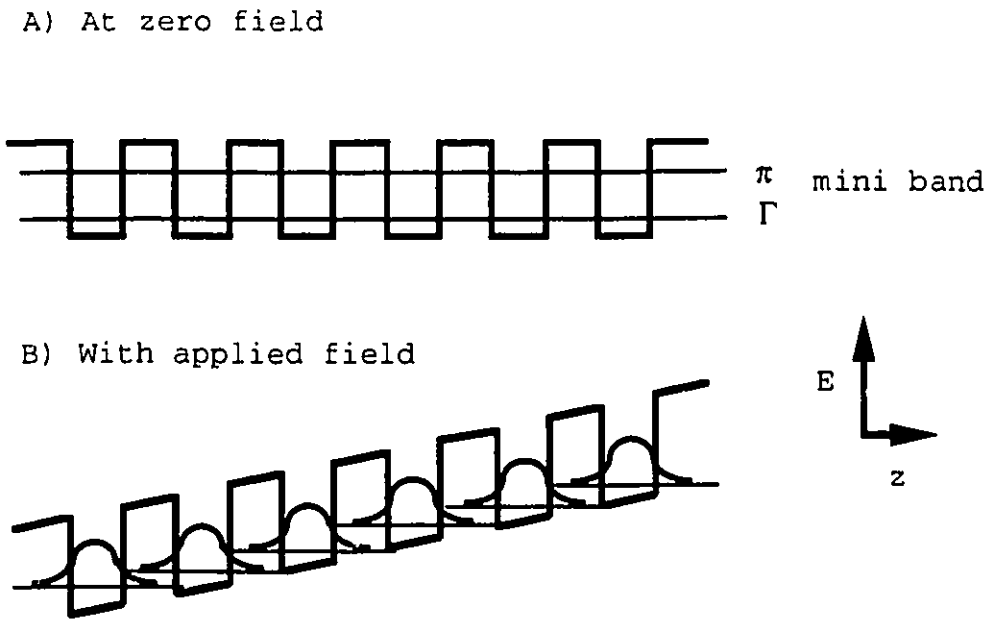

Figure 5. A) Superlattice at zero field showing interwell coupling. B) Stark localization due to applied field.

The ladder like progression in energy of the localised states (Wannier Stark ladder) was predicted by Wannier in a 1962 paper discussing the "Dynamics of Band Electrons in Electric and Magnetic Fields" [4] which described the behaviour of electrons in a bulk crystal lattice. Other papers followed also suggesting their existence: M. Saitoh [5], Fukuyama et al. [6], Bentosela et al. [7] among others. Experimental verification of the Stark ladders proved elusive until the advent of semiconductor superlattice structures. The first experimental verification appears to be that of Mendez et al. [8] (1988) who observed Stark localisation in $Al_xGa_{1-x}As$-GaAs superlattices using photoluminescence and photocurrent spectroscopy. This was followed by observations of Stark

ladders in: AlGaInAs-GaInAs superlattices by Bleuse et al. [9] (1998), K. Fujiwara (1989) in a GaAs-AlAs superlattice [10], Soucail et al. (1990) [11], and Gibb et al. (1990) [12] in $In_xGa_{1-x}As$-GaAs superlattices.

The experimental observation of the Wannier Stark ladders in the semiconductor superlattices is a result of their large lattice constant which is of the order of 10 nm, and their narrow miniband-widths of 10's of meV. This permits weak electric fields to displace adjacent quantum wells by a measurable amount. For example a weak 10 $kVcm^{-1}$ electric field applied to a 10 nm period superlattice causes the extended superlattice states to rapidly localize, and displaces the adjacent wells by a measurable 10 meV in potential energy. This is in contrast to bulk crystals where fields as large as 10^6 Vcm^{-1} displace adjacent atomic sites by less than 0.5 meV.

i-v Experimental methods

The interband transition energies for the $In_xGa_{1-x}As$-GaAs quantum wells and superlattices examined in this work range from 1.3 to 1.5 eV which is in the near-infrared spectrum, 820 to 950 nm. Both the $In_xGa_{1-x}As$ and GaAs materials have direct gaps at their lowest interband transition energies. These two features make the $In_xGa_{1-x}As$-GaAs structures amenable to several optical spectroscopic methods. A simple probe for measuring the lowest direct gap energy is photoluminescence which involves photo-injecting excess carriers into the conduction and valence bands. These excess carriers can then recombine radiatively (photoluminescence or PL) or

nonradiatively. The photoluminescence spectrum generated by the photo-excited semiconductor exhibits an easily measurable sharp peak associated with the lowest direct bandgap (k=0) transition. This energy gap for the $In_xGa_{1-x}As$-GaAs quantum well structures is given by the sum of the strained energy gap of the $In_xGa_{1-x}As$ layer at its Γ point, plus the first quantized energy levels for the electrons and holes, less the exciton binding energy.

Photocurrent spectroscopy (PC) of pin or Schottky diodes permits an electric field to be applied to the samples. This type of spectroscopy probes the sample with nearly monochromatic radiation. The measured spectral response (photocurrent) produced by the absorbed radiation yields spectral features similar to that of absorption spectroscopy, hence both indirect ($\kappa \neq 0$) and direct ($\kappa = 0$) interband transitions can be observed. This includes the lowest interband transition energy as well as higher energy transitions. The PC data reveals relatively sharp spectral features for each excitonic transition which are easily identified and measured.

Electroreflectance (ER), in contrast, is a derivative technique whereby the eigenstate energies of the quantum wells and superlattices are weakly perturbed by an oscillating electric field. The sample is again probed with nearly monochromatic light, but now the weak changes in the reflected light from the sample are readily detected. Very sharp derivative like features are observed for each interband transition. Electroreflectance while being a more sensitive probe of the interband transition energies than

photocurrent spectroscopy, yields data that is considerably more difficult to interpret. These two techniques are used to measure the Quantum confined Stark effect, and Wannier Stark ladders in our samples.

i-vi Motivation

Considerable theoretical work has been done on quantum wells and periodic potentials such as bulk semiconductors. It is only in the last 20 years that one dimensional potentials could be fabricated on a quantum scale. This permits the experimental study of the behaviour of electrons confined to quantum structures, as well as the effects of perturbing electric and magnetic fields. The objective of this work is to gain an understanding of the behaviour of the energy states of shallow quantum wells and superlattices when perturbed by a static electric field.

i-vii Summary of thesis

In the course of this research 25 wafers were grown by low pressure metalorganic vapour phase epitaxy. 260 pin and Schottky diodes were fabricated from these wafers and screened using current-voltage and photocurrent measurements. Four quantum well samples (M049-M052) and three strained layer superlattice samples (H145, L073, and L121) were selected for extensive examination using photoluminescence, photocurrent spectroscopy, and electroreflectance, all performed with the samples kept at liquid helium temperature. Results from these seven devices were subsequently analyzed, and these are presented in this thesis. The analysis was performed within the framework of the single band envelope

formalism of Bastard [13]. The key findings of this work are:

- Calculation of the field dependent reduction of the exciton binding energy associated with the lowest interband transition (E1H1) for the $In_xGa_{1-x}As$-GaAs quantum well.

- Experimental support for the validity of the single band approximation for calculating field dependent interband transition energies for $In_xGa_{1-x}As$-GaAs quantum well.

- First experimental observation of Wannier Stark localization in $In_xGa_{1-x}As$-GaAs superlattices.

- Calculation of electron and heavy-hole Wannier Stark ladders.

- Calculation of end effects including Tamm states.

i-viii Thesis outline

Chapter one reviews the physics and numerical methods used to calculate the eigenstate energies and effects of a perturbing static electric field. The experimental methods and samples are discussed in Chapter two. The experimental results for the quantum wells are presented and analyzed in Chapter three. The results and calculations for the superlattice samples, demonstrating the Wannier Stark ladders are

presented in Chapter four. Chapter five presents the exciton Stark ladder calculations by Dignam and Sipe for two of our samples, L121 and H145. Calculations for the end effects of the terminated superlattice, within the single-particle model, are discussed as well.

Chapter 1

Modelling of the Quantum Confined Stark Effect, Wannier Stark Ladders, and Exciton Binding Energies.

1-1 Introduction

This chapter reviews some of the analytic and numerical methods used in the literature to calculate the eigenstate energy levels for semiconductor quantum wells and superlattices. These include variational calculations for the quantum confined Stark effect (QCSE), field dependent exciton binding energies, and a tight binding analysis for the Wannier Stark ladders. Also reviewed are the Krönig-Penney model as applied to the superlattice in a one band or effective mass formalism, the transfer matrix method, and a numerical integration calculation using a Runge-Kutta algorithm. The latter is a computer program developed by Geof Aers at NRC, and is used extensively in this thesis.

1-2 Bandgaps

The semiconductor superlattices studied in this thesis comprise thin alternating layers of $In_xGa_{1-x}As$ (wells) and GaAs (barriers) with thicknesses of the order of 5 to 10 nm. The two binary constituents GaAs and InAs which make up the ternary alloy $In_xGa_{1-x}As$ have different lattice constants. In the absence of strain the lattice constant of the ternary $In_xGa_{1-x}As$ may be obtained as a linear interpolation of these two. Growth of $In_xGa_{1-x}As$ on a GaAs initially starts with the $In_xGa_{1-x}As$ layer being commensurate with the GaAs layer. The $In_xGa_{1-x}As$ lattice is biaxially compressed in the xy plane to

match the GaAs layer, while in the z or growth direction the $In_xGa_{1-x}As$ lattice expands. It becomes energetically favourable, at some point in growth, for the strained $In_xGa_{1-x}As$ layer to relax via the formation of dislocations. The onset of this relaxation signifies the critical thickness of the $In_xGa_{1-x}As$ epilayer and is dependent upon its relaxed lattice constant or alloy composition.

The distortion of the strained $In_xGa_{1-x}As$ layer modifies its band structure by splitting the light and heavy hole bands at the Γ point and by increasing its gap E_g. The strained energy gaps for the conduction band edge to heavy-hole and light-hole bands at the Γ point are given, to a first approximation by [14-15],

$$E_{CB-|hh\rangle} = E_g + \delta E_H + \frac{\delta E_S}{2} \tag{1}$$

$$E_{CB-|lh\rangle} = E_g + \delta E_H - \frac{\delta E_S}{2} - \frac{(\delta E_S)^2}{2\Delta_0} \tag{2}$$

where E_g is the unstrained $In_xGa_{1-x}As$ bandgap, Δ_0 is the spin-orbit coupling, while the hydrostatic pressure shift δE_H and uniaxial stress induced splitting δE_S are,

$$\delta E_H = 2a\varepsilon(C_{11} - C_{12})/C_{11} \tag{3}$$

$$\delta E_S = -2b\varepsilon(C_{11} + C_{12})/C_{11} . \tag{4}$$

a is the hydrostatic pressure potential, b the uniaxial deformation potential and C_{ij} are the elastic stiffness constants for the $In_xGa_{1-x}As$ layer. The in-plane biaxial

strain components of the strain tensor $\varepsilon=\varepsilon_{xx}=\varepsilon_{yy}$ are given by,

$$\varepsilon = (a_{GaAs} - a_{InGaAs})/a_{InGaAs} \qquad (5)$$

with the strain free lattice constant for the $In_xGa_{1-x}As$ layer being obtained as a linear interpolation from the two binaries,

$$a_{InGaAs} = 5.6536 + 0.4054(x) \quad (\text{Å}). \qquad (6)$$

The conduction band heavy-hole gap $E_{CB} - E_{|hh>}$ (equ. 1) is exact while the conduction band light-hole strained energy gap $E_{CB}-E_{|lh>}$ (equ. 2) is a series expansion of a quadratic root. The next term in the expansion is small being $-\frac{\delta E_S^3}{4\Delta_0^2}$, approximately 0.5 meV for $In_{.125}Ga_{.875}As$.

The strain free energy gap of $In_xGa_{1-x}As$ at the Γ point is less than that of GaAs resulting in a type I potential well for the electrons and heavy-holes which are confined in the $In_xGa_{1-x}As$ layer. The situation for the light-holes is less clear, and depending upon how the band offsets at the $In_xGa_{1-x}As$:GaAs interface are assigned, the light-holes may be confined to either the $In_xGa_{1-x}As$ or GaAs layer. We use a conduction band heavy-hole offset ratio of 65:35 which leaves the light-hole being localised in the GaAs layer. This is shown schematically below in figure 6. This value for the band offset ratio has yielded good agreement between the calculated and measured transition energies for the quantum wells and superlattices studied in this lab, though it is not universally accepted.

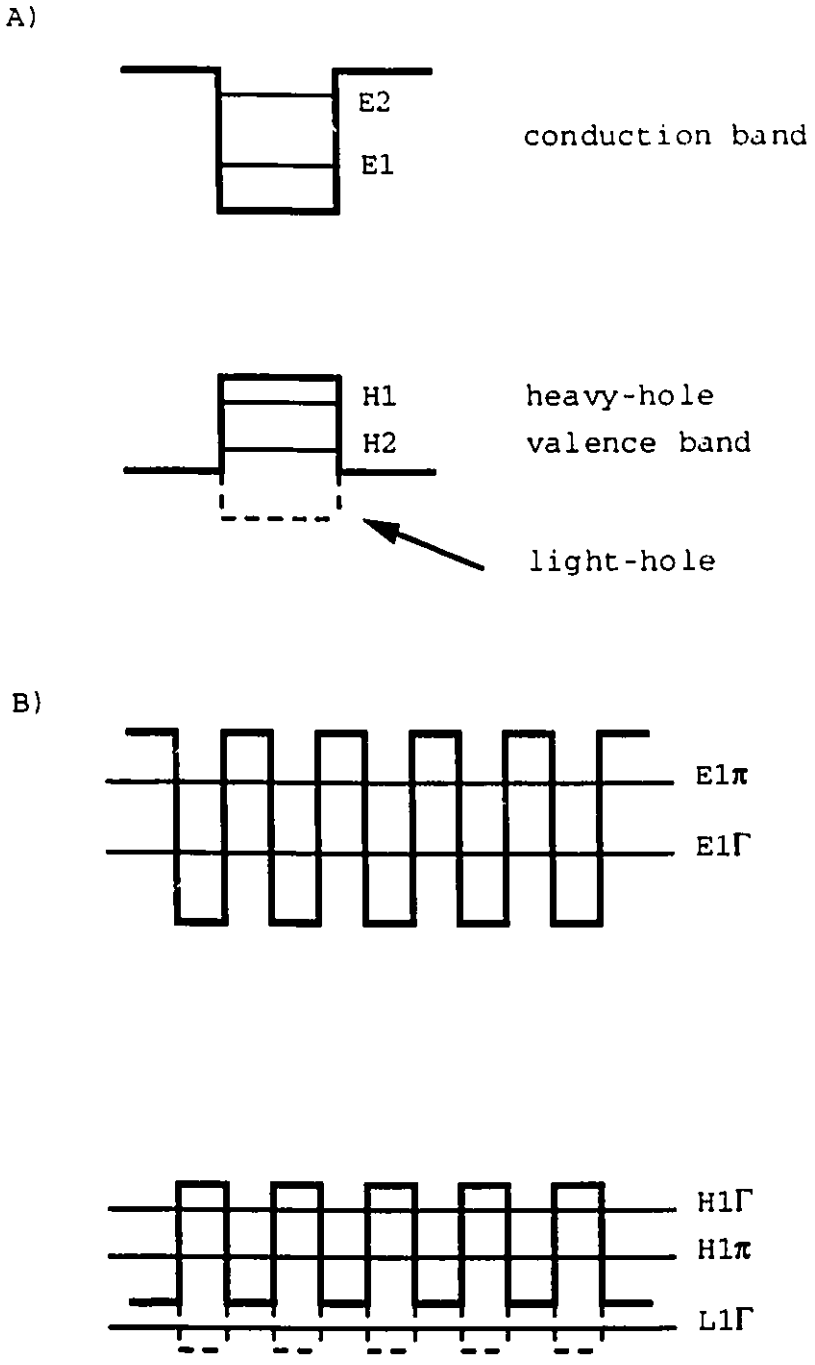

Figure 6. A) Conduction and valence band profile for quantum well. B) Potential profile for superlattice. Several eigenstates are also indicated.

Figure 6A) represents the quantum well structure where the electrons and heavy-holes are confined in the $In_xGa_{1-x}As$ layer. The first and second electron and heavy-hole levels are indicated. The superlattice structure Figure 6B) is a series of quantum wells separated by narrow barriers. For small period structures coupling between the quantum wells gives rise to a miniband structure for the electron, heavy-hole, and light-hole levels. An E-K diagram showing the Γ and Π points for the superlattice is shown in Fig.2 of the Introduction. The energy levels for both structures can be calculated using the single band Krönig-Penney model, or more rigorously with the two and three band models. The two band model includes coupling of the conduction band with the light hole valence band, while the three band model includes additional coupling to the split-off band.

1-3 Krönig-Penney model

The Krönig-Penney model has been successfully applied to the one dimensional superlattice potential using an envelope function formalism [13]. In the one band or effective mass model only the potentials and effective masses of the constituent layers are retained. Effects such as band non-parabolicity, differing lattice constants, and valence band coupling at the Γ points are ignored.

The electron or hole wave functions are written as the product of a plane wave term $\exp(i\kappa z)$ and a periodic part $U(z)$. The resulting Bloch function, $\Psi(z)=U(z)\exp(i\kappa z)$, now satisfies both Schrödinger's equation and the Bloch-Floquet theorem. $\Psi(z)$ is inserted into the Schrödinger equation

$$\frac{\hbar^2}{2m^*}\frac{\partial^2\Psi(z)}{\partial z^2}+\{E-V\}\Psi(z)=0 \qquad (7)$$

where m^*, V, are the appropriate effective masses and potentials for the well and barrier regions. The resulting differential equation retains terms only in U(z), the plane wave component exp(iκz) having been eliminated,

$$\frac{d^2U(z)}{dz^2}+2i\kappa\frac{dU(z)}{dz}+\left(\frac{2m^*}{\hbar^2}(E-V)-\kappa^2\right)U(z)=0. \qquad (8)$$

The resonant energy of the system for a given wave vector κ is obtained using the boundary conditions requiring continuity of U(z) and U'(z)/m at the interfaces, the latter being the conservation of probability current. The solution of (8) is tedious but results in the transcendental equation

$$\cos(\kappa d)=\cos(k_0a)\cosh(q_0b)+\frac{1}{2}\left(\frac{m_a}{m_b}\frac{q_0}{k_0}-\frac{m_b}{m_a}\frac{k_0}{q_0}\right)\sin(k_0a)\sinh(q_0b)$$

$$k_0=\sqrt{\frac{2m_a(E-V_a)}{\hbar^2}}$$

$$q_0=\sqrt{\frac{2m_b(V_b-E)}{\hbar^2}}, \qquad (9)$$

where m_a and m_b are the well and barrier effective masses, and V_a and V_b are the well and barrrier potentials respectively. a and b are the well and barrier widths of the superlattice.

This one band or effective mass model becomes identical to the usual Krönig-Penney result when the well and barrier masses are made equal ($m_a=m_b$).

More complicated models have been presented such as the two band model which includes coupling between the conduction and light-hole bands and the three band model which includes additional coupling to the split-off band [16], both of which provide a more accurate calculation of the higher energy levels. All three models give similar results for the lowest lying energy levels which are of concern in this work.

The single quantum well eigenenergies can be extracted from the above dispersion relationship by letting the barrier thicknesses tend to infinity. This causes the hyperbolic functions $\sinh(q_0 b)$ and $\cosh(q_0 b)$ to diverge. Setting equality of the dispersion relationship (9) to zero now requires,

$$0 = 1 + \frac{1}{2}\left(\frac{m_a}{m_b}\frac{q_0}{k_0} - \frac{m_b}{m_a}\frac{k_0}{q_0}\right)\tan(k_0 a). \tag{10}$$

This transcendental equation contains the product of both the even and odd solutions to the single quantum well [17],

$$\tan\left(\frac{k_0 a}{2}\right) = \frac{m_a}{m_b}\frac{q_0}{k_0} \tag{11}$$

$$\tan\left(\frac{k_0 a}{2}\right) = -\frac{m_a}{m_b}\frac{q_c}{k_0}. \qquad (12)$$

The equations (9) through (12) still rely on the one band or effective mass model, being most accurate for the lower lying levels. Energies of the states lying near the top of the wells are less precisely known due to our neglecting band non-parabolicity, band mixing, among other effects. The single band Krönig-Penney model (equ. 9, 11, and 12) is used for all the zero-field calculations performed in this thesis.

1-4 The transfer matrix method

An alternate but equally valid approach for calculating the superlattice and quantum well eigenenergies makes use of Floquet's theorem [18] which is a restatement of the Bloch condition in a matrix formulation. Here the wave function $\Psi(z)$ and its derivative $\Psi'(z)$ are related to their values at any point in the structure by a transfer matrix,

$$\begin{bmatrix}\Psi(z)\\ \Psi'(z)\end{bmatrix} = \mathbb{A}\begin{bmatrix}\Psi(0)\\ \Psi'(0)\end{bmatrix}. \qquad (13)$$

Only two transfer matrices are required to describe the superlattice potential analyzed with the Krönig-Penny model,

$$A_{well} = \begin{bmatrix} \cos(k_0 a) & \frac{m_a}{k_0}\sin(k_0 a) \\ \frac{-k_0}{m_a}\sin(k_0 a) & \cos(k_0 a) \end{bmatrix} \qquad (14)$$

$$A_{barrier} = \begin{bmatrix} \cosh(q_0 b) & \frac{m_b}{q_0}\sinh(q_0 b) \\ \frac{q_0}{m_b}\sinh(q_0 b) & \cosh(q_0 b) \end{bmatrix}. \qquad (15)$$

These matrices contain the orthogonal solutions Ψ and Ψ' to Schrödinger's equation for the well and barrier regions. The effective mass formalism for matching Ψ'/m across the interface is included.

Flocquet's theorem or the Bloch condition is invoked by noting that for a full period of translation the values of Ψ and Ψ' are retained

$$\begin{bmatrix} \Psi(z+d) \\ \Psi'(z+d) \end{bmatrix} = e^{i\kappa d} \begin{bmatrix} \Psi(z) \\ \Psi'(z) \end{bmatrix}. \qquad (16)$$

The eigenstate energies for the superlattice are obtained from the dispersion relationship as,

$$2\cos(\kappa d) = \mathrm{Trace}\left\{A_{well} \times A_{barrier}\right\}. \qquad (17)$$

The analytic expression of (equ. 17) for the superlattice potential is identical to the Krönig-Penney model (equ. 9). The transfer matrix method is not restricted to using the barrier and well widths as the basis set for the matrices. These wells and barriers may be broken up into thin segments ie. 0.5 nm, with a transfer matrix for each segment. The dispersion relation is now given by the trace of the product

of these matrices,

$$2\cos(\kappa d) = \text{Trace} \prod_n A_n \, . \tag{18}$$

This formulation allows one to consider structures other than square wells, such as: triangular potentials, step, asymmetric, and parabolic wells [16], or structures with an applied bias [19]. This latter problem is of interest in calculating the quantum confined Stark effect (QCSE) and Wannier Stark ladders.

1-5 Quantum confined Stark effect (QCSE)

1-5-1 Transfer matrix method applied to the quantum well

The transfer matrix method is readily used to determine the QCSE for the isolated quantum well which is treated as a potential well clad by thick barriers. The electric field is incorporated into the transfer matrices as a series of potential steps [19] which are added onto the unperturbed potential of the quantum well as shown in Figure 7 below.

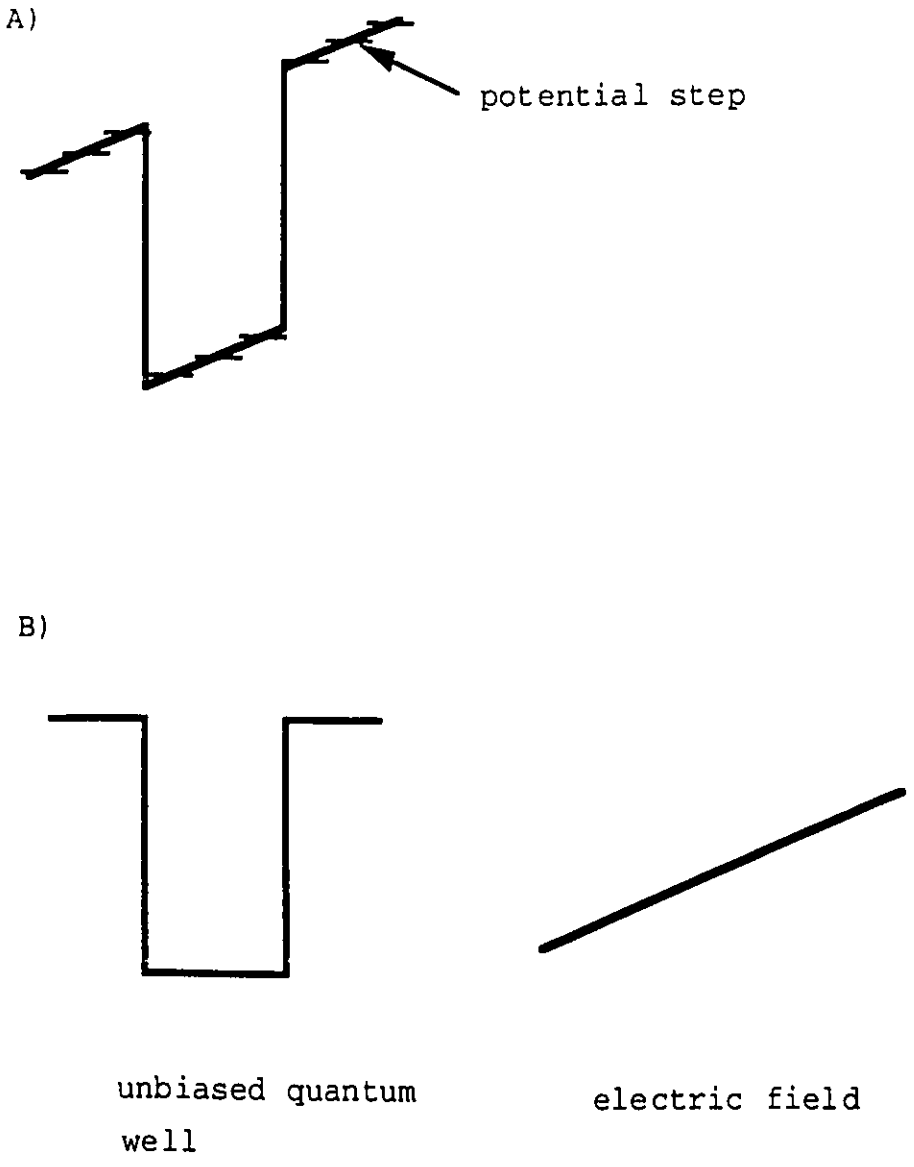

Figure 7. A) quantum well under bias with potential steps used for transfer matrix calculations. B) Biased QW is the sum of isolated quantum well potential, and electric field perturbation.

It often is necessary to make the segments quite thin (0.2 to 0.5 nm) in order to obtain accurate calculations of the QCSE. The potential used in each slice is the quantum well potential plus the average field potential for the slice. The field dependent wavevectors are

$$k = \sqrt{\frac{2m_a^*}{\hbar^2}\left(E - qFz - V_a\right)}$$

$$q = \sqrt{\frac{2m_b^*}{\hbar^2}\left(V_b - E + qFz\right)}. \qquad (19)$$

It should be noted that the electric field operator qFz is unbounded, diverging as z tends to infinity. This causes computational difficulties on the high energy side of the field perturbed quantum well where the hyperbolic terms diverge at large values of z. Additionally, the electrons and holes eventually tunnel out on the low energy side of the wells to become free particles. The basis sets described in equations (14 and 15) do not describe this carrier tunnelling. While it is rigorously incorrect to treat the particle as being in a bound state even at weak fields, the weak field approximation (ie. quasibound particles) and the basis sets (equ. 14 and 15) yield a fair approximation to the true QCSE. Carrier tunnelling can be included by allowing energy to be a complex quantity.

The use of real energies yields eigenenergies that are only approximate at large fields for shallow quantum wells. This

is especially true for the $In_xGa_{1-x}As$-GaAs quantum well heavy-hole levels where the transfer matrix calculations fail at fields as low as 30 $kVcm^{-1}$. The calculation is more suited to the deeper $Al_xGa_{1-x}As$-GaAs quantum wells, where the argument for quasibound carriers is stronger.

1-5-2 Transformed Hamiltonian (Airy functions)

There is no a-priori requirement to use the orthogonal basis functions given by (equ. 14 and 15) in solving for the QCSE. An alternate formulation for the quantum well under the influence of an applied electric field involves a change in variable in Schrödingers equation. The Hamiltonian may be transformed into the linear second order differential equation

$$\frac{d^2\xi}{d\xi^2} - \xi\Psi(\xi) = 0$$

$$\xi = -\left(\frac{2m^*qF}{\hbar^2}\right)^{\frac{1}{3}}\left(z + \frac{E-V}{qF}\right). \qquad (20)$$

This differential equation has solutions given by the orthogonal Airy functions,

$$\Psi(\xi) = aAi(\xi) + bBi(\xi) \ . \qquad (21)$$

The coefficients a, and b are obtained by matching Ψ and Ψ'/m at the interfaces of the quantum well, and noting that Ψ is an oscillatory wave outside the well on the low energy side, and tends to zero on the high energy side inside the barrier.

Several methods for obtaining the eigenstate energies have been employed including phase-shift analysis [20-21], or tunnelling lifetimes [22].

This formulation gives an accurate description of the tunnelling of carriers out of the well, and is valid for high fields. It suffers though from the requirement to numerically obtain the values for $Ai(\xi)$ and $Bi(\xi)$ which are inherently calculation intensive functions. The computational expenditure can be reduced by the use of lookup tables and interpolation schemes to obtain $Ai(\xi)$ and $Bi(\xi)$.

This method has been incorporated into the transfer matrix method to calculate the QCSE as well as the Wannier Stark ladders. Here the Hamiltonian is divided up into well and barrier regions, each having unique solutions in the form of (equ. 21). A transfer matrix is generated for each. The eigenstate energies are calculated using the dispersion relationship given by (equ. 18) [16, 23], or calculated from resonance conditions [24-25].

1-5-3 Perturbation and variational methods for the infinite quantum well

The quantum confined Stark effect may be calculated for the infinitely deep quantum well using either perturbational or variational methods. Both serve a pedagogical purpose of demonstrating the quadratic nature of the QCSE for the square well. Second order perturbation theory gives for the field dependent eigenstate energies,

$$E_n = E_{n0} + \langle \Psi_n | qFz | \Psi_n \rangle + \sum_{m \neq n} \frac{|\langle \Psi_m | qFz | \Psi_n \rangle|^2}{E_m - E_n} \quad . \tag{22}$$

The first term is the field free infinite quantum well energy for the n^{th} level. The second term describes the linear field dependence to $E_n(F)$ which is identically zero due to the odd nature of the integrand. The last term generates the quadratic field dependence. This is the lowest order expansion term to generate a field dependence, and for the ground state level it is given by Bastard et al. [26] as

$$E(F) = E_0 - \frac{1}{24\pi^2}\left(\frac{15}{\pi^2} - 1\right)\frac{m^* q^2 a^4 F^2}{\hbar^2} \quad . \tag{23}$$

The QCSE may also be calculated using variational methods. Here the ground state function is modified by a prefactor to describe the effects of the perturbing field. Two common prefactors are $(1-\beta z)$ and $\exp(-\beta z)$. The first being the Taylor series expansion of the exponential function, and is the simplest expression that yields the quadratic field dependence. The QCSE in the low field limit using the linear prefactor for the ground state is

$$E(F) = \frac{\langle (1-\beta z)\Psi^0 | H_0 + qFz | (1-\beta z)\Psi^0 \rangle}{\langle (1-\beta z)\Psi^0 | (1-\beta z)\Psi^0 \rangle} \quad , \tag{24}$$

having the solution

$$E(F) = E_0 - \frac{2m^* q^2 F^2 \langle z^2 \rangle_0^2}{\hbar^2} \quad , \tag{25}$$

where

$$\langle z^2 \rangle_0 = \frac{a^2}{2}\left\{\frac{1}{6} - \frac{1}{\pi^2}\right\} \quad . \tag{26}$$

This result is identical to the Stark shift for the infinite quantum well when the exponential trial function is used,

$$E(F) = \frac{\langle \exp(-\beta z)\Psi^0 | H_0 + qFz | \exp(-\beta z)\Psi^0 \rangle}{\langle \exp(-\beta z)\Psi^0 | \exp(-\beta z)\Psi^0 \rangle} \quad . \tag{27}$$

This result is to be expected since the exponential prefactors are also Taylor series expanded, retaining the leading order quadratic term, during the minimization process to obtain an analytic expression for β [26].

1-5-4 QCSE for finite quantum wells

The finite quantum well is of more interest due to the ability to realize experimental structures from a number of semiconductor families. The perturbation series calculation (equ. 22) again reveals zero linear field dependence to the Stark shift. A quadratic field dependence is predicted, though the calculation of its magnitude proves cumbersome since the summation is over all the bound states within the well and the extended states lying above the barriers.

Variational calculations of the QCSE based upon the trial

functions $(1-\beta z)\Psi^0$ and $\exp(-\beta z)\Psi^0$ prove adequate in the weak field limit, giving a quadratic field dependence. These trial functions are also used to calculate the overlap integrals for the optical absorption coefficient, as well as determining exciton binding energies.

An analytic expression for the QCSE using the linear variational trial function $(1-\beta z)\Psi^0$ with Ψ^0 being the zero field, ground state, finite well wave function is readily obtained using (equ. 24) and having the solution given by equation (25). The second moment $\langle z^2\rangle_0$ is now a more complicated function dependent upon the size of the quantum well being studied. It is given by [26]

$$\langle z^2\rangle_0 = \frac{\frac{a^2}{2}\left[\frac{1}{6}+\frac{\sin(k_0a)}{2k_0a}+\frac{\cos(k_0a)}{(k_0a)^2}-\frac{\sin(k_0a)}{(k_0a)^3}+\frac{1}{q_0}\cos^2\left(\frac{k_0a}{2}\right)\left\{1+\frac{2}{q_0a}+\frac{2}{(q_0a)^2}\right\}\right]}{\left[1+\frac{\sin(k_0a)}{k_0a}+\frac{2\cos^2\left(\frac{k_0a}{2}\right)}{q_0a}\right]} \qquad (28)$$

This value for the second moment $\langle z^2\rangle_0$ converges to the infinite square well value as the barrier height (V) is increased. In the limit that V tends to infinity, q_0a also goes to infinity and k_0a tends to π. $\langle z^2\rangle_0$ for the finite quantum well is always greater than its value for the infinite quantum well. This can be interpreted as the extent of spreading of the electron and hole wave functions into the

barrier regions. $\langle z^2 \rangle_0$ can also be loosely interpreted as an equivalent infinite quantum well width as Miller et al. [27] have done in their calculations of the QCSE and exciton binding energy. The exponential trial functions $\exp(-\beta z)\Psi^0$ do not yield analytically tractable solutions for the finite well QCSE (equ. 27), though numerical calculations give similar results as the linear variational trial wave function [26]. These two variational methods are used to obtain the field dependent electron and heavy-hole wave functions needed to calculate the field dependent reduction to the exciton binding energies.

These calculations apply to both the electron, heavy-hole and light-hole states confined to the conduction and valence band potential wells. The ground state energies are now labelled E1, H1, and L1 for the electrons, heavy-holes, and light-holes respectively, and replace E_0 in equations (23 and 25). The field dependent interband transition energies for the quantum wells are given by the sum of the strained $In_xGa_{1-x}As$ energy gaps (equations 1 and 2), and the field perturbed eigenstate energies for both the electrons and holes equations (23 or 25).

1-6 Wannier Stark ladders

The following calculations for the Wannier Stark ladders are performed within the single particle model. This model treats the electrons and heavy-holes as separate entities, coupled by the Coulomb interaction. This model is further simplified by treating the Coulomb interaction as a separable term in the Hamiltonian, ie. as a constant. This term is

then ignored for the calculation of the electron and hole energy levels, and hence interband transition energies. The $In_xGa_{1-x}As$-GaAs superlattices studied in this work exhibit strong interwell coupling for the electrons, with little coupling for the heavy-holes. This is due to the small electron and large heavy-hole masses. Hence, the heavy-hole states may be modelled as single quantum well functions. The electrons, at zero applied field in contrast, are distributed in energy as described by the Krönig-Penney model.

The application of a longitudinal electric field causes a weak Stark shift of the heavy-hole levels, but has a profound effect on the electrons. The applied unbounded electric field operator removes the translational symmetry of the conduction band periodic potential. This causes the extended superlattice states to coalesce into states localized about each successive quantum well, with energies given to first order by the isolated quantum well states which make up the superlattice. This results in a ladder like progression of eigenstate energies being displaced by the potential difference of the successive wells qFd, where d is the superlattice period and F the electric field.

The existence of the Wannier Stark ladders was initially derived for the periodic potential of bulk material [4-6], however conclusive experimental verification was prevented by the short lattice constants, and large allowed conduction bands of bulk semiconductors. These combined to prevent the observation of the Stark ladders for fields less than 10^6 Vcm^{-1}, in the region of avalanche breakdown. Experimental verification was delayed until the advent of semiconductor

superlattices [8,10-11,28-30], having superlattice periods and miniband-widths on the order of 10 nm and 50 meV respectively . McIlroy [23] provided the earliest calculation of the superlattice Wannier Stark ladders using the coordinate transformed Hamiltonian (equ. 20) for each well and barrier region of the superlattice.

Emin and Hart [31] showed that the field perturbed superlattice potential could be rearranged as the sum of a staircase and a periodic sawtooth potential shown below in figure 8. The staircase potential gives rise to the Wannier Stark ladders, while the periodic sawtooth potential may be absorbed into a Bloch like function yielding a weak quadratic red QCSE shift for each level.

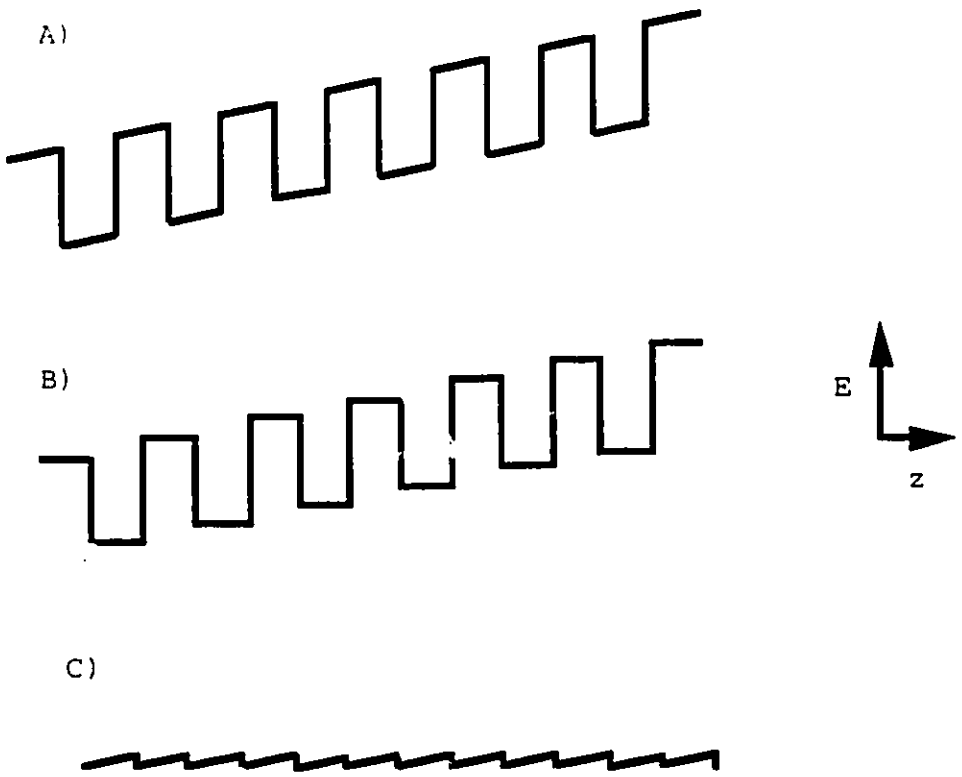

Figure 8. The superlattice potential with an applied field A) may be expressed as the sum of the staircase potential B) and a triangle potential C).

The rearranged potential also permits the use of the sin(ka), cos (ka), sinh(qb), cosh(qb) basis sets (equ. 14 and 15) in a transfer matrix calculation to obtain the Wannier Stark ladders. A transfer matrix is generated for each well and barrier, with the electric field potential qFz being incorporated as the average potential for each layer. The superlattice structure of N periods can be built up with 2N+2 transfer matrices. The residual 2 matrices represent the buffer layers at each end of the superlattice. The field

limitation mentioned earlier of 30 kVcm^{-1} is reduced somewhat by the increased size of the whole superlattice, however, the Wannier Stark localization and the appearance of the Stark ladders also occur at these weak fields. The transfer matrix turns out to be an effective method for calculating the Stark ladder energies, which are obtained from resonances in the trace of the product of the well and barrier matrices (equ.18).

1-6-1 General solution for the tight binding method

Voisin et al. [32], Bleuse [33], and Bleuse et al. [34] have used a tight binding method to obtain an analytic expression for the Stark ladder energies and wave functions suitable for calculating the superlattice absorption constant as a function of electric field. This model is used to calculate the field dependence of the Stark ladders, as well as estimate their oscillator strengths. The following analysis is for the conduction and periodic potential, the solution for the valence band is the same. However, the high effective masses of the heavy-holes result in these states being strongly localised even at zero electric fields, hence they can be treated as single quantum well like states.

A premise is made that the envelope function $|\chi\rangle$ for the superlattice can be built up as a superposition of states localised about each successive well, $|\chi\rangle = \Sigma a_n \Phi_n\rangle$. These localised states $|\Phi_n\rangle$ are assumed to be orthogonal to each other $\langle\Phi_m|\Phi_n\rangle = \delta(m,n)$ and normalized, ie. Wannier type functions. $|\Phi_n\rangle$ is the Wannier function located at the n^{th} site of a 2N+1 well superlattice. The superlattice

Hamiltonian in the absence of the Coulomb interaction is expressed as the sum of the kinetic energy operator, the periodic square well potential, and the applied electric field.

$$H_H = \frac{P_z^2}{2m^*} + \sum_{p=-N}^{N} V_c(z - pd) + qFz \quad . \tag{29}$$

The eigenstate energies for the superlattice are obtained by operating on the Wannier functions over all of the well potentials as shown schematically below in Figure 9.

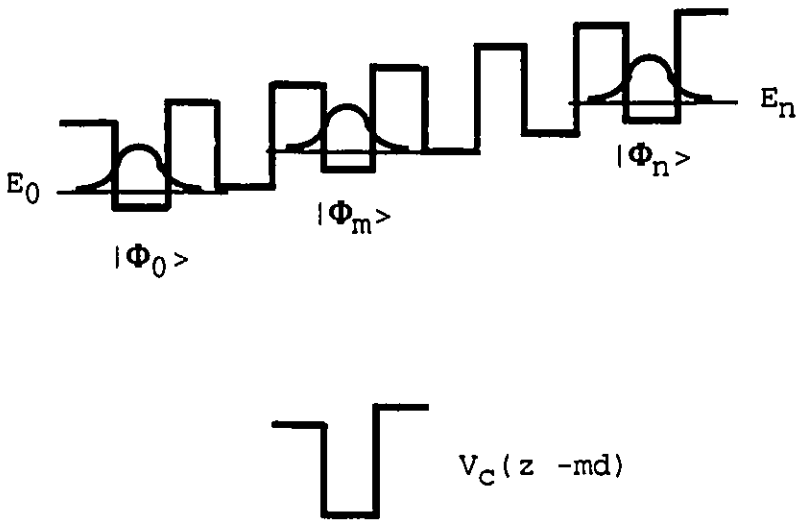

Figure 9. Depiction of Wannier functions $|\Phi_n\rangle$, and the superlattice potential V_c.

The energy E_m for the m^{th} site Wannier function is,

$$E_m = \langle \Phi_m | H_N | \Phi_n \rangle = \left\langle \Phi_m \left| \frac{P_z^2}{2m^*} + V_c(z - pd)_{p \neq n} \right| \Phi_n \right\rangle + \sum_{p \neq n} \langle \Phi_m | V_c(z - pd)_{p=n} | \Phi_n \rangle$$

$$+ \langle \Phi_m | qFz | \Phi_n \rangle , \qquad (30)$$

or

$$E_m = E_0 \delta(m,n) + \sum_{p \neq n} \langle \Phi_m | V_c(z - pd) | \Phi_n \rangle + \langle \Phi_m | qFz | \Phi_n \rangle \ . \qquad (31)$$

1-6-2 Tight binding model at zero field

Voisin et al. [32], and Bleuse [33] first examined the zero field case (F=0), where $|\Phi_m\rangle$ is taken to be located at the m^{th} site and the overlap integrations are carried out over all the well potentials $V_c(z-pd)$ and Wannier functions $|\Phi_n\rangle$. The well potentials are taken to be $-V_c$ in the wells and zero outside, hence all of the overlap integrals $\langle \Phi_m | V_c(z-pd) | \Phi_n \rangle$ where $p = n \neq m \pm 1$ are greatly reduced allowing them to be ignored. The remaining overlap integrals $\langle \Phi_m | V_c(z-(m \pm 1)d) | \Phi_{m \pm 1} \rangle$ describe the nearest neighbour interactions,

$$\langle \Phi_m | H_N | \Phi_n \rangle = E_0 \delta(m,n) + \langle \Phi_m | V_c(z - (m-1)d) | \Phi_{m-1} \rangle + \langle \Phi_m | V_c(z - (m+1)d) | \Phi_{m+1} \rangle \ . \qquad (32)$$

These overlap integrals are equivalent,

$$|\lambda| = -\left\langle \Phi_m \middle| V_c\left(z-(m\pm 1)d\right) \middle| \Phi_{m\pm 1} \right\rangle \quad . \tag{33}$$

The quantity $4|\lambda|$ is the zero field miniband-width of the superlattice.

1-6-3 Tight binding model for applied fields

The electric field potential term in the site energy equation (30), $\langle \Phi_m | qFz | \Phi_n \rangle$, can be transformed by using the translational symmetry of the Wannier functions $|\Phi_m\rangle$,

$$\left\langle \Phi_m \middle| qFz \middle| \Phi_n \right\rangle = \left\langle \Phi_{m-n} \middle| qFz \middle| \Phi_0 \right\rangle + mqFd\left\langle \Phi_m \middle| \Phi_n \right\rangle \quad . \tag{34}$$

The first term is identically zero for m=n due to the odd nature of the integrand, while for $m \neq n$ it is taken to be small due to the weak fields under consideration. The second term is nonzero for m=n yielding for the m^{th} site energy,

$$E_m = E_0\delta(m,n) - |\lambda|\{\delta(m,n-1) + \delta(m,n+1)\} + mqFd\delta(m,n) \quad . \tag{35}$$

The allowed energies for each of the localized states $|\Phi_n\rangle$ is obtained from the solutions to this recursion relationship which is rewritten using $(E_m - E_0) = \rho|\lambda|f$ and $qFd = |\lambda|f$ to give,

$$[\rho - m]\delta(m,n) = \frac{1}{f}\{\delta(m,n-1) + \delta(m,n+1)\} \tag{36}$$

which is in the form of the standard recursion formula,

$$[\rho - m]C_m = \frac{1}{f}\{C_{m-1} + C_{m+1}\} \quad . \tag{37}$$

This has the general solution,

$$C_m = AJ_{m-\rho}(-2/f) + BY_{m-\rho}(-2/f) \qquad (38)$$

where J_υ and Y_υ are the Bessel and Neumann functions of order υ.

The allowed values that ρ may have are obtained by applying boundary conditions to the system. Fukuyama et al. [6] applied both rigid wall boundaries at each end of the superlattice structure, as well as periodic boundary conditions to obtain the Stark ladder energies. The rigid wall boundaries require the wave functions to stop at each end of the structure, ie. $C_{-N-1} = C_{N+1} = 0$ leading to the eigenvalue equation,

$$J_{-N-1-\rho}(-2/f)Y_{N+1-\rho}(-2/f) - J_{N+1-\rho}(-2/f)Y_{-N-1-\rho}(-2/f) = 0 \ . \qquad (39)$$

The high field limit where $1/f << 1$, results in the Wannier functions $|\Phi_n\rangle$ being tightly localised to each potential well. This permits to first order the expansion of the Bessel and Neumann functions resulting in the eigenvalue equation,

$$(f)^{2(N+1)}\frac{\Gamma(N+1-\rho)}{\Gamma(-N-\rho)} - \left(\frac{1}{f}\right)^{2(N+1)}\frac{\Gamma(N-1-\rho)}{\Gamma(N+2-\rho)} = 0 \ . \qquad (40)$$

This is dominated by the first term where the Gamma function has poles for negative integer arguments. Hence for ρ being

an integer the Stark ladder energies are obtained,

$$E_m = E_0 + pqFd \quad . \tag{41}$$

Where p refers to the site index for the Stark ladder. E_0 is the eigenenergy for the centre of the superlattice. The heavy-holes are confined to the same layer as the electrons, type I superlattice, resulting in an electron to heavy-hole interband transition energy being given by,

$$E = E_{(CB-|hh)} + E1 + H1 + pqFd \quad . \tag{42}$$

The light-holes are confined to the GaAs layers, resulting in a type two superlattice. The light-holes are now offset from the electron states by half the superlattice period yielding Stark ladders with slopes of (p + 1/2)qFd. The electron to light-hole interband transition energy is given by,

$$E = E_{(CB-|lh)} + E1 + L1 + \left(p + \frac{1}{2}\right)qFd \, . \tag{43}$$

Fukuyama et al. [6] have extended their analysis of the Stark ladders to both intermediate and low fields. They obtain weak deviations from the Stark ladder behaviour for sites near the band edges at intermediate fields, while at low fields the Stark ladder structure becomes more complex.

Dignam and Sipe [35,36] have expanded on this type of analysis by including the Coulomb interaction between the electron and hole superlattice states. Their calculations

follow a tight binding analysis with a basis set being generated from separable electron, hole quantum well wave functions, and a simple 1-S like hydrogenic exciton term. They obtain the Wannier Stark ladders with a more complex low field ($F<5$ kVcm^{-1}) behaviour than predicted by Bleuse [33]. This is to be expected since the simple tight binding scheme presented earlier considers the high field case where the electrons and holes are strongly localised, and neglects the Coulomb interactions. Dignam and Sipe [36] have also determined the field dependence of the superlattice exciton binding energies for several of the Stark ladder levels, along with their optical absorption strengths and wave functions.

1-7 Tight binding model - Stark ladder oscillator strengths

Bleuse's tight binding model [33] permits the calculation of the oscillator strengths of the Wannier Stark ladders which determine the absorption and emission spectra of the superlattices. This calculation neglects the electron-hole Coulomb interaction so that only a general picture of the absorption spectrum for the superlattice is obtained.

The total conduction band Wannier superlattice wave function is obtained as a superposition of the isolated quantum well functions

$$|\chi_n\rangle = \sum_{\rho=-N}^{N} J_{n-\rho}\left(\frac{-2|\lambda|}{qFd}\right)|\Phi_\rho\rangle \ , \qquad (44)$$

where $J_{n\,\rho}(-2|\lambda|/qFd)$ is the Bessel function of order n-ρ, and $|\Phi_\rho>$ is the single quantum well wavefunction. A similar expression is obtained for the valence band. Bleuse obtains the optical absorption constant as the overlap integral over the conduction and valence band Wannier functions,

$$\alpha = \alpha_0 \sum_{m=-N}^{N} \sum_{n=-N}^{N} \Upsilon\left(\hbar\omega - \left\{E_g + (m-n)qFd\right\}\right) \left|\langle \chi_m | \chi_n \rangle\right|^2 \quad , \tag{45}$$

where $\Upsilon\left(\hbar\omega - \left\{E_g + (m-n)qFd\right\}\right)$ is the unit step function. The relative strengths of each of the Stark ladders can be calculated as

$$\left|\langle \chi_m | \chi_n \rangle\right|^2 \approx \left| \sum_{\rho=-N}^{N} J_{n-\rho}\left(\frac{-2|\lambda_c|}{qFd}\right) J_{\rho-n}\left(\frac{-2|\lambda_v|}{qFd}\right) \right|^2 \quad . \tag{46}$$

Letting the summations ρ = -N to N extend to infinity results in the simplified expression,

$$\left|\langle \chi_m | \chi_n \rangle\right|^2 \approx \left\{ J_p\left(\frac{-2\left[|\lambda_v| + |\lambda_c|\right]}{qFd}\right)\right\}^2 \quad , \tag{47}$$

where p is the ladder index and $4|\lambda|$ is the zero field miniband-with. This last equation is used to calculate the Stark ladder oscillator strengths.

1-8 Numerical integration method

One of many numerical methods for calculating the QCSE and Wannier Stark ladders was implemented by Geof Aers at NRC. $Al_xGa_{1-x}As$-GaAs resonant tunnel diodes embedded in GaAs were

one of the early devices to be studied. This method treats the resonant tunnel devices as a transmission problem, making use of Schrödinger's equation. A travelling wave in a momentum state defined by the wavevector k_1 is incident and partially reflected at the left most GaAs-$Al_xGa_{1-x}As$ interface, with a travelling wave being transmitted at the right most $Al_xGa_{1-x}As$-GaAs interface with wave vector k_2 as shown below,

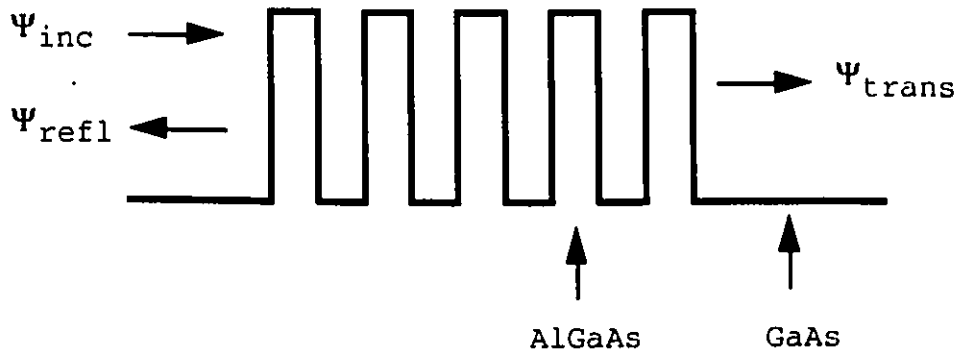

Figure 10. $Al_xGa_{1-x}As$-GaAs superlattice with incident, reflected and transmitted wave functions. This arrangement is used in the numerical integration program.

The total wave function in the GaAs layer at the left GaAs-$Al_xGa_{1-x}As$ interface and its derivative are given by,

$$\Psi_L(z) = \exp\{i(k_1 - \omega t)\} + B\exp\{-i(k_1 - \omega t)\} \tag{48}$$

$$\Psi_L'(z) = ik_1\exp\{i(k_1 - \omega t)\} - ik_1 B\exp\{-i(k_1 - \omega t)\}\ , \tag{49}$$

where the amplitude of the incident wave is normalized to unity, and the amplitude B of the reflected wave is the same for both Ψ and Ψ'. Eliminating B from both equations and evaluating at the GaAs-$Al_xGa_{1-x}As$ interface yields,

$$\Psi_L(0) + \frac{\Psi_L'(0)}{ik_1} - 2 = 0 \quad . \tag{50}$$

The transmitted wave from the last $Al_xGa_{1-x}As$-GaAs interface is again a free particle,

$$\Psi_R(z) = C\exp\{i(k_2 z - \omega t)\} \quad , \tag{51}$$

and using the boundary conditions for Ψ and Ψ' at the interface leaves,

$$\Psi_R(0) = C$$

$$\Psi_R' = ik_2 C \quad . \tag{52}$$

The wavevector $k = \sqrt{\frac{2m^*(E-V)}{\hbar^2}}$ is given an initial arbitrary value with E being a complex quantity. The wave functions Ψ and Ψ' are propagated back through the structure from right to left using Schrödinger's equation in a Runge-Kutta algorithm. The potential profile of the structure along with the continuity conditions for Ψ and Ψ'/m are used. The differential equation (50) is evaluated using values for the wave functions at the left interface, Ψ_L and Ψ_L', with the transmission coefficient C being adjusted to obtain equality. New values for the complex energy E are used until a resonance condition is obtained in the transmission

coefficient C.

The $In_xGa_{1-x}As$-GaAs structures examined in this thesis are also embedded in GaAs, however, these layers are now barriers. The incident, reflected, and transmitted wave functions are now evanescent waves. Their wavevectors k are now given by $k = \sqrt{\frac{2m^*(V-E)}{\hbar^2}}$ with E still being complex.

The program implemented by Geof Aers evaluates the potential profiles and automatically selects the correct form for the wavevector k. The back propagation of the wave functions using the Runge-Kutta algorithm is not unique and several transfer matrix methods work equally well. The variational and transfer matrix calculations presented earlier work well for deep potential wells, and for the shallow $In_xGa_{1-x}As$-GaAs wells at weak applied electric fields. However, their accuracies are reduced at large fields. Hence, this numerical algorithm is used extensively in this work to calculate the field dependent eigenstate energies.

1-9 Coulomb interaction-exciton binding energies

The calculated interband transition energies have so far ignored the Coulomb attraction between the electrons and holes confined in the quantum wells and superlattices. The free exciton binding energy for bulk semiconductors is relatively simple to calculate, being given by the hydrogen atom model using the dielectric constant for the semiconductor. These binding energies are of the order of 3 meV, in contrast to quantum well exciton binding energies which are more than double this. This enhancement is due to

the confinement of the carriers in the wells in the longitudinal or growth direction.

The calculation of the exciton binding energy for the quantum well or superlattice is complicated by the reduced symmetry of the system. The electrons and holes are relatively free to move in the in-plane or transverse direction, i.e. the planes formed by the quantum wells. The motion in the longitudinal direction is restricted due to the confining potentials. This asymmetry of the potential profile experienced by the electrons and holes suggests that the Hamiltonian be written in a centre of mass picture, assuming nondegenerate isotropic bands [37],

$$H = \frac{P_{z_e}^2}{2m_e^*} + \frac{P_{z_h}^2}{2m_h^*} + \frac{P_x^2 + P_y^2}{2(m_e^* + m_h^*)} + \frac{P_x^2 + P_y^2}{2\mu} - \frac{q^2}{4\pi\varepsilon\varepsilon_0\sqrt{x^2 + y^2 + (z_e - z_h)^2}} \quad . \qquad (53)$$

The centre of mass motion of the excitons may be neglected, permitting the Hamiltonian to be rewritten in cylindrical coordinates,

$$H = \frac{P_{z_e}^2}{2m_e^*} + \frac{P_{z_h}^2}{2m_h^*} - \frac{\hbar^2}{2\mu}\left[\frac{1}{\rho}\frac{\partial}{\partial\rho}\rho\frac{\partial}{\partial\rho} + \frac{1}{\rho^2}\frac{\partial^2}{\partial\phi^2}\right] - \frac{q^2}{4\pi\varepsilon\varepsilon_0\sqrt{\rho^2 + (z_e - z_h)^2}} \quad , \qquad (54)$$

where μ refers to the reduced electron-hole mass in the transverse or in-plane motion, and $\rho^2 = x^2 + y^2$.

This Hamiltonian is solved variationally using trial wave functions either separable or nonseparable in x, y, and z. The nonseparable trial functions provide the correct binding energies in the limit of zero and infinite well width [37],

while the separable function provides a simpler solution that is reasonably accurate for well widths ranging from 5 to 15 nm. This latter solution is also used for determining the electric field dependence of the exciton binding energies.

The nonseparable trial function is given by

$$\Psi = f(z_e)f(z_h)\exp\left(-\frac{1}{\lambda}\sqrt{\rho^2 + (z_e - z_h)^2}\right)$$

$$f(z) = \Psi^0 = A\exp(-|k_0 z|) \qquad |z| = a/2$$

$$= B\cos(q_0 z) \qquad -a/2 \le z \le a/2 \ , \qquad (55)$$

where f(z) is the zero field finite quantum well wave function, λ is the variational parameter used to minimize for the exciton binding energy. The nonseparable trial function has been used to calculate the electric field free exciton binding energies for the infinite quantum well [37], finite quantum wells in $Al_xGa_{1-x}As$-GaAs [38-39], as well as for the $In_xGa_{1-x}As$-GaAs system [40-41].

The separable trial function is given by

$$\Psi = \frac{1}{\lambda}\sqrt{\frac{2}{\pi}}f(z_e)f(z_h)\exp\left(-\rho/\lambda\right) \ . \qquad (56)$$

The exponential term, $\exp(-\rho/\lambda)$, describes the 1-S hydrogen like exciton. This latter trial function has been used for the infinite quantum well [37], and for determining the

electric field dependence of the exciton binding energy [42-45] in finite quantum wells. The exciton binding energy is calculated as the difference between the field dependent electron and heavy hole levels E1(F) and H1(F) and the total energy,

$$E_b = E1(F) + H1(F) - \langle \Psi | H_{TOT} | \Psi \rangle \quad , \tag{57}$$

or

$$E_b = \frac{q^2 \left\langle \Psi \left| \sqrt{\rho^2 + (x^2 + y^2)} \right| \Psi \right\rangle}{4\pi\varepsilon\varepsilon_0} - \frac{\hbar^2}{2\mu\lambda^2} \quad . \tag{58}$$

This latter equation uses the separable trial function (equation 56). The integration of equation (58) is over the radial extent of the exciton, θ and ρ, and the displacement of both the electron and hole, z_e and z_h. Two approaches are used to perform the integrations, Brum et al. [42] expanded the Coulomb term as a Fourier series then integrated, alternately the function can be first integrated analytically over the radial extent, θ and ρ, leaving a double integral over z_e and z_h,

$$E_b = \frac{\pi q^2}{4\varepsilon\varepsilon_0} \iint f^2(z_e) f^2(z_h) \left[\mathbf{H}_1\left(2\gamma/\lambda\right) - \mathbf{N}_1\left(2\gamma/\lambda\right) + \frac{\pi}{2} \right] dz_e dz_h - \frac{\hbar^2}{2\mu\lambda^2} \quad , \tag{59}$$

where $\mathbf{H}_1(2\gamma/\lambda)$ and $\mathbf{N}_1(2\gamma/\lambda)$ are the Struve and Neuman functions, $\gamma = |z_e - z_h|$. The functions $f(z_e)$ and $f(z_h)$ are normalized.

The inclusion of the electric field to determine the field dependence of the exciton binding energy involves modifying the functions $f(z_e)$ and $f(z_h)$ to account for the field induced charge separation. Hong and Singh [44] solve numerically for the quantum confined Stark effect and use the resulting wave functions in the double integration of (equ. 59). Alternatively, the ground state quantum well wave functions can be modified by either the linear or exponential variational functions used to calculate the QCSE discussed earlier,

$$f(z) = N(\beta)(1-\beta z)\Psi^0 \quad , \tag{60}$$

or

$$f(z) = N(\beta)\exp(-\beta z)\Psi^0 \quad , \tag{61}$$

where $N(\beta)$ is the normalizing term. Both of these trial functions give accurate results for deep quantum wells typical of the $Al_xGa_{1-x}As$-GaAs system. The results are less precise for the shallower $In_xGa_{1-x}As$-GaAs quantum wells, though both trial functions (equations 60 and 61) are used to calculate the field dependence of the quantum well exciton binding energies.

The superlattice exciton binding energy at zero field has only been recently calculated in a single particle model [46] and more completely by Dignam and Sipe [36,47] who include the presence of electric fields. A particularly simple model for calculating the "oblique exciton" ($p=\pm1$ ladders) was presented by Soucail et al. [48]. The 'oblique' exciton refers to the Coulomb interaction between electrons and holes localized in adjacent wells in the superlattice. This model

considers the high field case where the Stark ladder states are completely localised in the wells. The single quantum well wavefunctions then provide good trial wave function which can be used in equation (59) to calculate the exciton binding energies. The p=±1 or oblique exciton binding energies are calculated by offsetting the electron and hole wave functions by the translation of the function by one period of the superlattice.

1-10 Summary

A number of mathematical models have been reviewed in this chapter that are used to calculate the eigenenergies for quantum wells, superlattices and excitons. All the models so far discussed consider the electron, hole, and excitons to be single particle like in their behaviour. Additionally the three valence bands, light-hole, heavy-hole, and split-off, are assumed to be noninteracting.

The interpretation of the experimental results for the four quantum wells and three superlattices makes extensive use of the models presented in this chapter. In particular the quantum well and superlattice structures are determined from an analysis of their optical spectra x-ray data, and growth conditions, using the Krönig-Penney model and band calculations discussed in sections 1-2, and 1-3. This analysis also includes the exciton binding energy calculations outlined in 1-9.

The measured field dependent exciton transition energies for the quantum wells are analysed using the variational

calculations for the quantum confined Stark effect outlined in section 1-5-4, as well as by the numerical integration method discussed in 1-8, and the variationally calculated exciton binding energies, section 1-9. The measured Stark ladder exciton transitions are analysed using either Bleuse's tight-binding model, the transfer matrix calculations, or by numerical integration.

Chapter 2

Experimental Methods and Samples

2-1 Samples

26 wafers comprising single and multiple quantum wells, as well as superlattices were grown using a low pressure MOVPE growth system during the course of this work. Both pin diode and Schottky diodes were subsequently fabricated from the grown material and examined using an applied electric field as a perturbation. A brief summary of all the material studied is presented in Table 3 at the end of the Chapter. Seven samples yielded field dependent photocurrent spectra suitable for detailed analysis, including 4 $In_xGa_{1-x}As$-GaAs quantum wells grown as pin diodes, and 3 superlattices grown using a Schottky diode structure. Both structures were grown on (100) oriented n$^+$ GaAs substrates. The superlattice samples using the Schottky diode structure consisted of a 0.5 to 2 μm thick undoped GaAs buffer layer, followed by a 10 period $In_xGa_{1-x}As$-GaAs strained layer superlattice, a 10 to 205 nm thick undoped GaAs cap layer. The quantum well samples utilizing the pin diode structure incorporated a 1.8 μm thick undoped GaAs buffer layer, followed by the $In_xGa_{1-x}As$ single quantum well. This was followed by a 60 nm undoped GaAs buffer layer, and a 60 nm p-doped GaAs cap layer. The structures are shown below in figure 11.

A)

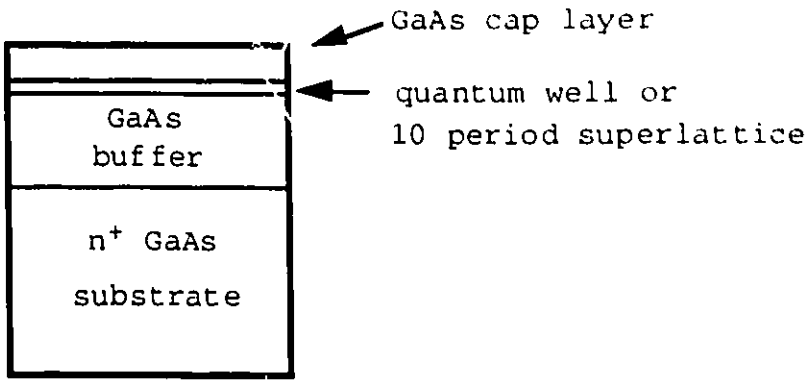

B)

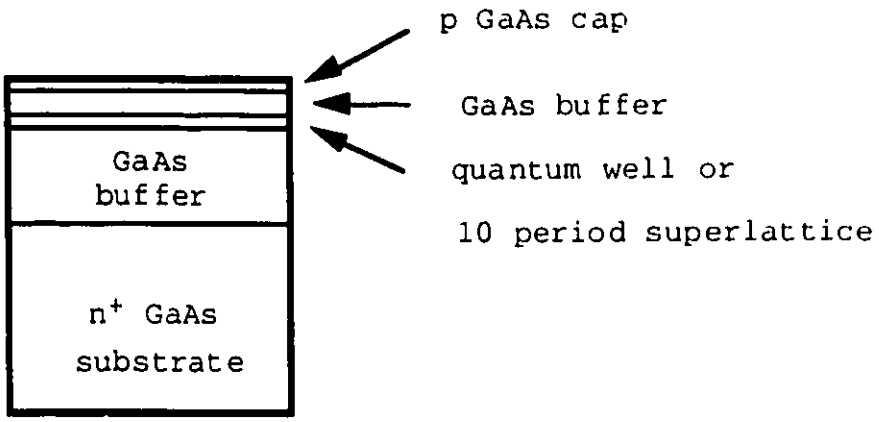

Figure 11. A) Schottky diode structure. B) pin diode structure.

The grown layers were examined using low temperature photoluminescence to confirm that the quantum well or superlattice layer thicknesses, and alloy compositions were close to the target values. Several measurements were made across the surface of each wafer to check for material

uniformity. Wafers yielding good PL intensity and uniformity, as well as having composition and layer thicknesses close to target values were selected for processing into diodes. The quantum well widths and alloy composition for the 4 samples based upon a growth calibration are, 2.5, 5.0, 7.5, and 10 nm and 15% indium fraction. The sample structures for the four quantum wells as determined from fitting their photocurrent spectra are listed in table 1.

Table 1. Quantum well structures, as fitted from PC data.

Sample	well width (nm)	In (%)
M049	2.5	12.5
M050	5.5	12.5
M051	7.5	12.5
M052	10.0	12.5

The superlattice samples were also examined using PL to determine their structures. X-ray measurements were also performed on the three superlattice structures to determine their superlattice periods to within 0.2 nm, and alloy compositions to within 1%. Both the nominal and measured alloy compositions and layer thicknesses for the superlattice samples, as determined from x-ray measurements, are listed in table 2.

Table 2 Superlattice structures

parameter	H145		L121		L073	
	growth	x-ray	growth	x-ray	growth	x-ray
buffer (μm)	1.8		0.68		0.5	
well (nm)	3.0	2.5	5.5	6.0	5.0	5.1
Well In (%)	12	13	13	16.2	7.0	6.5
Barrier (%)	0	0	0	2.2	0	0
barrier (nm)	10.0	9.0	5.5	5.9	5.0	5.0
cap (nm)	10		205		120	

The as-grown epilayers for the Schottky diode structures were then processed. The wafers were cleaved to yield nominally 3 mm x 6 mm chips. These were then degreased in the sequence of boiling chloroform, boiling acetone, and boiling chloroform. Back contacts were then formed by alloying indium into the n$^+$ substrates under a heated argon-HCl atmosphere. Semi-transparent gold front contacts were evaporated onto the front surface using a shadow mask to define the contact area. The semi-transparent front contacts were nominally 2 mm x 5 mm large and 15 nm thick. Leads were soldered directly to the back indium contact, and epoxied to the front gold contact with silver epoxy. This prevented the front contacts from being made smaller than 2 mm x 5 mm.

The room temperature I-V characteristics for the Schottky diodes using a curve tracer indicated a built-in potential near 0.8V, and a reverse breakdown voltage ranging from 2 to 6V. The I-V characteristics could not be fitted to the common transport models for Schottky diodes, thermionic

emission or diffusion, in a meaningful fashion. The reverse I-V characteristics strongly indicated transport being dominated by defects. However, many of the diodes generated a photocurrent when exposed to light, and the leakage currents were sufficiently reduced at liquid helium temperatures so that photocurrent measurements could be made for bias voltages less than 5V. The superlattice samples were examined at applied fields less than 30 $kVcm^{-1}$,-3V bias, so that the Schottky structures were adequate. All of the superlattice structures used in this study were grown and fabricated as Schottky diodes.

The quantum well structures required bias voltages extending to 20V, electric fields approaching 80 $kVcm^{-1}$, which precluded the use of the 2 mm x 5 mm Schottky diode contacts. These samples were therefore processed as pin diodes using a mesa structure to define their size, 400 µm diameter. An ohmic ring contact to the p-cap layer was made by evaporating layers of titanium, platinum, and gold. Layers of nickel, germanium-gold, were used to obtain ohmic contacts on the n^+ substrates. 1 cm x 1 cm pieces were scribed and cleaved from the wafer, containing about 15 diodes, and mounted onto 12 pin headers. The diodes were then wire bonded to the header pins. The fabricated pin diodes were tested for room temperature reverse leakage currents. A selection criteria for acceptable devices was reverse leakage currents I_R less than 100 nA @ 15V and room temperature, and sensitivity to light. Leakage currents higher than this resulted in excessive shot noise being generated by the diodes which interfered with the measurement of the photocurrent signal. A yield of 30% was obtained, or 3 to 4 good diodes per header

which could be used for photocurrent experiments.

2-2 Optical measurements

The exciton transition energies of the quantum well and superlattice structures can be precisely measured by a number of optical techniques including, transmission [3,49-50], photocurrent [8-12,51-56], photoluminescence [1,19,57-59], photoluminescence excitation [12,52,60], as well as by the derivative techniques of electroreflectance, and photoreflectance [33,61-65]. The work in this study involves perturbing the quantum states with an applied electric field to the samples fabricated as Schottky or pin diodes. The diode configuration allows the sample to be used as a photodetector, the photocurrent being related to the absorption coefficient. The diode structure also lends itself to highly sensitive electroreflectance measurements, whereby an AC modulation is superimposed upon the DC bias applied to the sample. The excitonic transitions are observed as changes to the sample's reflectivity in response to the AC modulation.

The $In_xGa_{1-x}As$-GaAs quantum well and superlattice structures are embedded in the intrinsic region of pin or Schottky diodes. The GaAs cap and buffer layers surrounding the quantum well structures have larger bandgaps and are transparent to the incident light used to probe the quantum structures. The photocurrent, for incident energy less than the GaAs bandgap, is related to the absorption coefficient giving rise to spectral features at energies due to excitonic

transitions between the quantum well and superlattice conduction and valence band states. These are observed as sharp peaks in the photocurrent signal with the photon energies being measured at the photocurrent maxima. However, at energies approaching the GaAs bandedge, absorption due to the cap and buffer layers increasingly dominates the photocurrent signal.

The direct relationship between the measured photocurrent and absorbed radiation assumes that the photogenerated carriers are collected and measured as a photocurrent before they recombine, a valid assumption at moderate and large fields. This is not the case under weak field conditions where the confining potentials of the quantum well structures inhibit the escape of the photogenerated carriers. Indeed under flatband conditions, the photocurrent becomes vanishingly small as the photogenerated carriers recombine as opposed to being transported out of the wells.

Electroreflectance (ER) permits the observation of the excitonic transitions over a larger range of applied biases, including flatband conditions. This technique involves perturbing the semiconductor with a small oscillating electric field which induces differential changes to the semiconductor's reflectivity. The small changes to the semiconductor's reflectivity can be measured using a phase sensitive detection method as provided by a lock-in amplifier. The differential nature of the electroreflectance signal suppresses the broad spectral reflectivity of the semiconductor and enhances structures localized about critical points. Features as weak as 1 part in 10^4 in the reflectance or photocurrent signal are easily resolved using

derivative techniques such as electroreflectance. The ER method also permits the observation of transitions above the GaAs bandedge, where the PC signal is dominated by the GaAs absorption.

While the energies for transitions observed in photocurrent spectra can be easily determined, the same is not true for the derivative methods such as electroreflectance which exhibit several peaks for each transition. The ER spectra reveals either a first derivative lineshape, third derivative lineshape, or even a mixture of the two for each transition. A third derivative electroreflectance signal with respect to the photon energy is observed when the electrons and holes are accelerated by the modulating electric field, such as in bulk semiconductors or the superlattices biased near flatband. Electrons and holes bound to quantum wells are not as easily accelerated by the oscillating electric fields. Their eigenenergies and lifetimes are modified by the Stark effect, as well as by the Coulomb interaction which is perturbed by the field induced charge separation [60]. This gives rise to a first derivative like spectrum. Perturbation to the Coulomb interaction is also expected to result in first derivative like spectra for excitonic transitions.

The precise determination of the energies of these structures involves fitting the ER spectra with a lineshape function of the form,

$$\frac{\delta R}{R} = \mathrm{Re}\left(e^{i\theta}\left(E - E_i + i\Gamma\right)^{-m}\right) \quad , \tag{62}$$

where E_j is the energy gap, Γ is the lifetime broadening parameter and θ is a phase factor. m depends upon the order of the derivative as well as the critical point type [61].

2-3 Apparatus

Low temperature photocurrent and electroreflectance measurements were made using the same apparatus at NRC, while a similar system for doing PC measurements was used at the University of Ottawa. The NRC system is described below and shown schematically in figures 12 and 13.

A 50 W halogen lamp is focused via a mirror onto the entrance slit of a 3/4 m Spex grating spectrometer. The incident white light first passes through a red long pass filter and is then chopped by a mechanical chopper at approximately 220 Hz for the PC measurements. The filter and chopper are not used in the electroreflectance measurements.

The emergent, nearly monochromatic light ($\Delta\lambda$= 0.5 nm FWHM for 0.5 mm slit width) from the spectrometer is then focused by a mirror onto the sample contained inside an Oxford Instruments continuous flow helium cryostat. The superlattice samples were attached to a copper cold finger using vacuum grease, while the pin diode samples were silver epoxied to glass headers which were then inserted into a socket mounted on a copper cold finger. This method of attachment does not appear to strain the samples upon cooling, as the GaAs exciton peaks are observed to be at 1514 meV, within a meV of the expected 1515 meV. The samples were oriented so that the light is incident on their front contacts. DC bias to the

Schottky and pin diodes is obtained from a potentiometer connected to a battery. This bias is applied to the diode in series with a 300 kΩ load resistance. The AC voltage generated across this resistance, due to the photocurrent generated by the pin or Schottky diode, is fed into a lock-in amplifier referenced to the mechanical chopper.

The ER apparatus shown in figure 13 makes use of a square wave oscillator (50 mV PP @ 280 Hz) capacitively coupled to a DC bias voltage to provide the AC modulation and DC bias which is applied to the sample. A 10 kΩ load resistance in series with the diode provides current limiting protection. The reflected light from the sample is focused onto a silicon pin photodiode. The photodiode, in parallel with a 1MΩ load resistance, is connected to the lock-in amplifier. The weak perturbations to the sample's reflectivity (electroreflectance signal) are then synchronously detected with respect to the reference output of the square wave oscillator. The analog output signal from the lock-in for both the photocurrent and electroreflectance measurements is digitized and collected by a customized XT computer.

The photoluminescence (PL) spectra were taken at 4K using either an argon ion laser, Krypton laser, or a Ti:Sapphire laser operating in the wavelength region of 850 to 950 nm. The excitation power was varied between 10 and 30 mW. The laser radiation was focussed to a small spot at a 45 degree angle incidence to the semiconductor surface. The photoluminescence generated by the sample was then focussed onto the entrance slit of the same spectrometer as used in the PC and ER experiments. The dispersed light from the spectrometer was then detected by a photomultiplier tube, and

recorded by the XT computer. Initial screening of the as-grown InGaAs-GaAs waters was performed using the 10 mW emission from the Ar^+ or Kr lasers, while the Ti:Sapphire laser was used to study the superlattice samples.

The system used at the University of Ottawa is the same except for the cryostat and the data collection. The University of Ottawa system makes use of a Janis Instruments immersion type cryostat, and the output signal from the lock-in amplifier is fed directly to an XY plotter. The data analysis for the quantum wells and superlattices is described in detail in chapters 3 and 4.

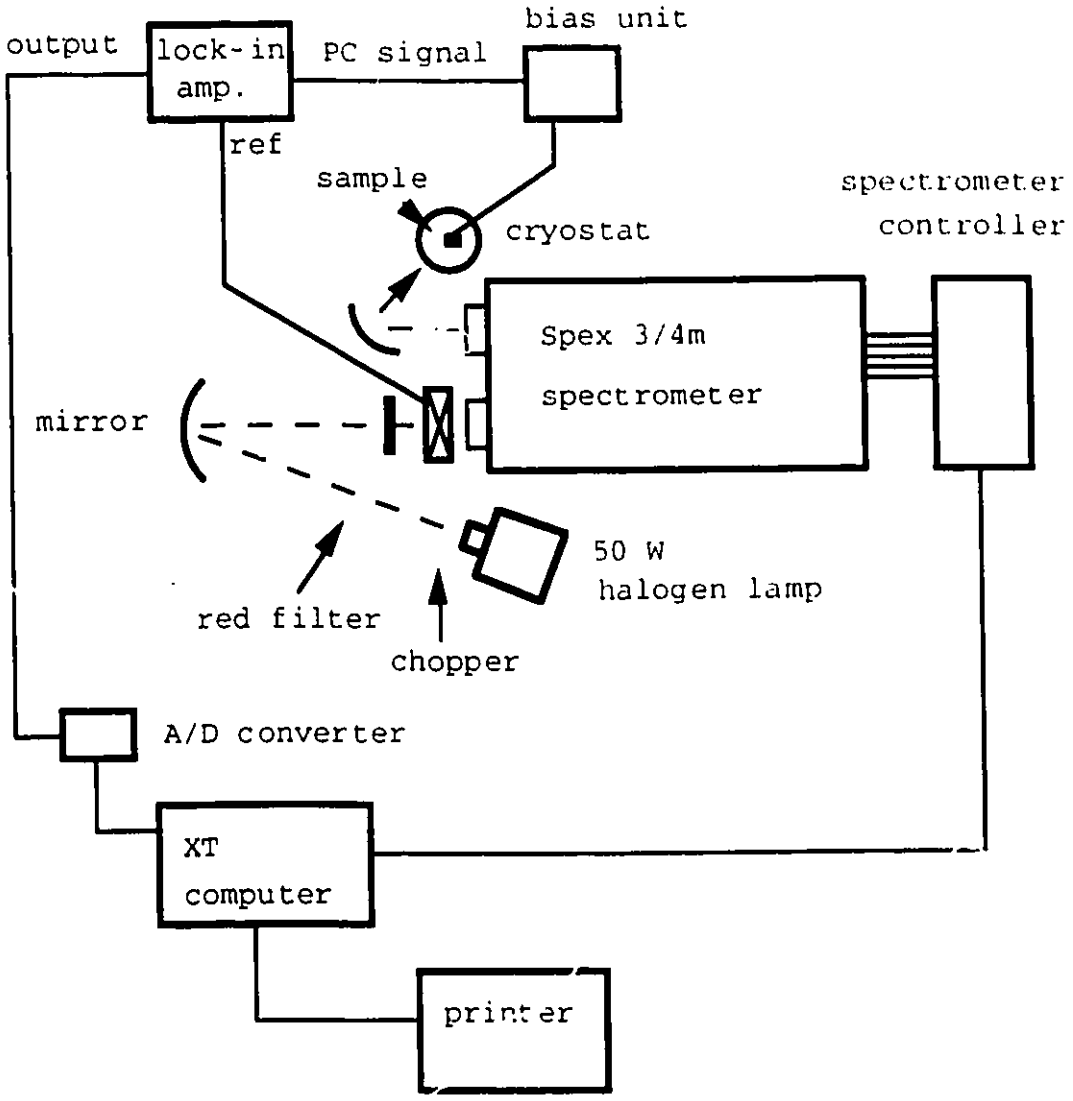

Figure 12. Photocurrent spectroscopy apparatus.

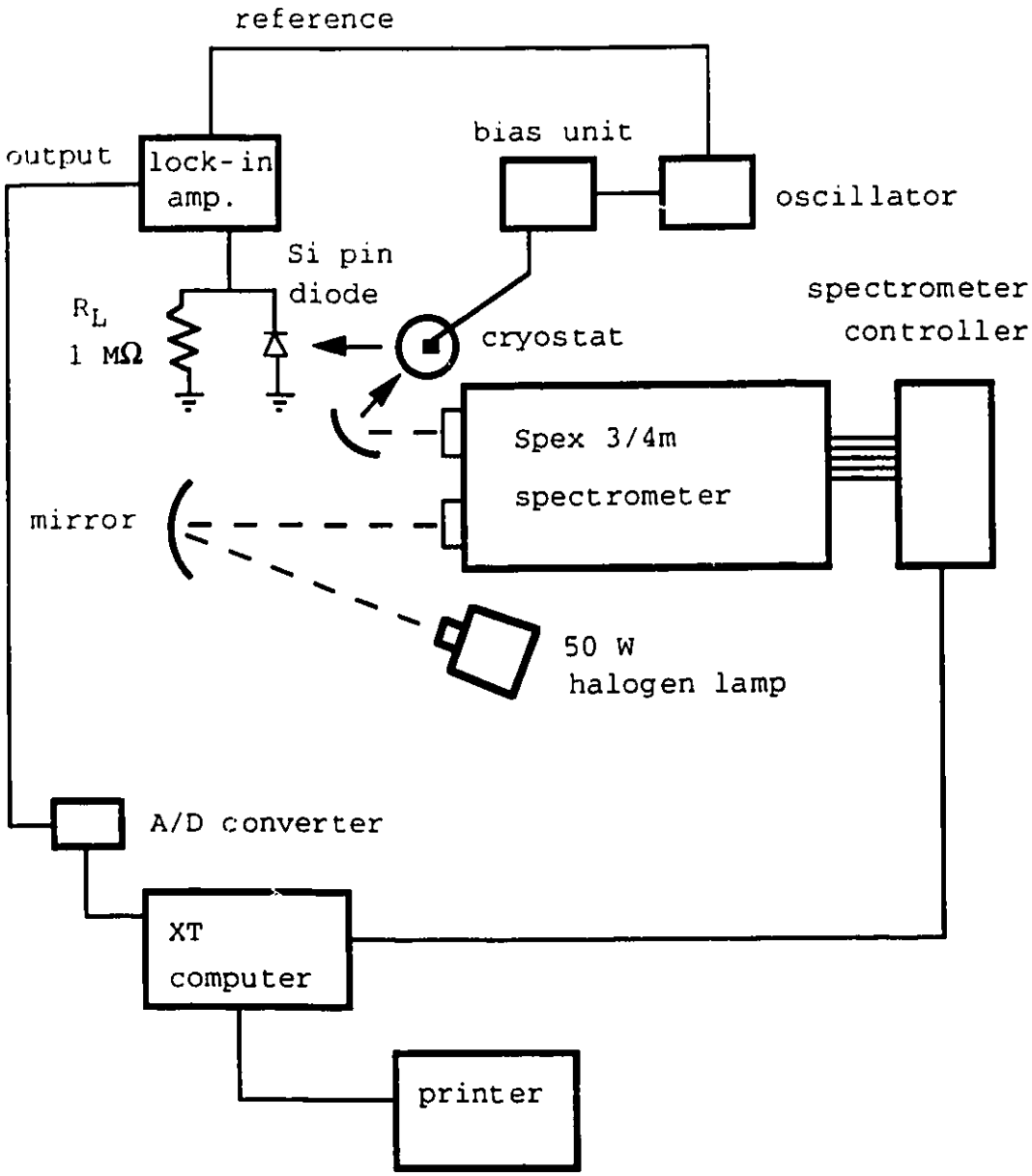

Figure 13. Electroreflectance apparatus.

Table 3. Summary of wafers studied

Sample #	Structure†	Comments††
H027	QW, 5nm, 12%, Sch diode	Weak QCSE
H140	SLS, 5nm, 10nm, 13%, Sch	Stark ladder not seen
H145	SLS, 2.5nm, 9nm, 13%, Sch	Good Stark Ladders
H146	QW, Schottky diode	Unable to fit spectra
I112	SLS, 7nm, 7nm, 16.5%, Sch	Stark ladders not seen
I113	SLS, 7nm, 7nm, Schottky	Stark ladders not seen
I122	QW, 10nm, 13.5%, Schottky	Shows good QCSE
L073	SLS, 5nm, 5nm, 7.3%, Sch	Strong Stark ladders
L074	SLS, 5nm, 5nm, pin diode	Strong Stark ladders
L118	QW, 5nm, 15%, Schottky	noisy
L119	MQW, 5.1nm, 50nm, 15%, Sch	noisy
L120	SLS, 5nm, 5nm, 15%, Sch	noisy
L121	SLS, 5nm, 5nm, 16%, Sch	Stark ladders seen
L122	SLS, 5nm, 10nm, 15%, Sch	Not studied
L123	SLS, 5nm, 10nm, 15%, Sch	Not studied
M045	QW, 2nm, 15%, Schottky	noisy
M046	QW, 5nm, 15%, Schottky	noisy
M047	QW, 7.5nm, 15%, Schottky	noisy
M048	QW, 10nm, 15%, schottky	noisy
M049	QW, 2.5nm, 12.5%, pin	Good QCSE
M050	QW, 5nm, 12.5%, pin diode	Good QCSE
M051	QW, 7.5nm, 12.5%, pin	Good QCSE
M052	QW, 10nm, 12.5%, pin	Good QCSE
P008	SLS, 4nm, 3nm, 15%, pin	High background PC
P009	SLS, 4nm, 5nm, 15%, pin	High background PC
P010	SLS, 4nm, 7nm, 15%, pin	High background PC
P011	SLS, 4nm, 10nm, 15%, pin	High background PC
P012	SLS, 6nm, 2nm, 15%, pin	High background PC

Summary of wafers continued.

Sample #	Structure	Comments
P013	SLS, 6nm, 3.5nm, 15%, pin	High background PC
P014	SLS, 6nm, 4.5nm, 15%, pin	High background PC
P015	SLS, 6nm, 6nm, 15%, pin	High background PC

† Notation for the wafers follows as: device type quantum well (QW), strained layer superlattice (SLS), well width, barrier width, well alloy composition, device structure either Schottky diode or pin diode. Layer thicknesses and alloy compositions are nominal.

†† Noisy devices were a result of high reverse leakage currents when the bias voltage is increased past -4V generating too much shot noise. 2 mm x 5 mm semi transparent evaporated gold front contacts were used to form the Schottky diodes. The high reverse leakage currents are believed to be due to defects, reducing the size of the contacts to less than a 0.2 mm^2 resulted in good pin diodes. The same result is expected for the Schottky diodes.

The high background PC from the samples P008-P015 appears to be associated with the GaAs absorption edge. Weak structures due to the superlattice exciton transitions showed little Stark shifting with an applied bias, suggesting the absence of an electric field in the intrinsic region of the diode. ER data confirmed the absence of the electric field. The cause of this is not known.

Chapter 3

Experimental Results for Quantum Wells

3-1 Introduction

The effects of a perturbing static field on four quantum wells, in the pin diode configuration, were examined using photoluminescence (PL) and photocurrent (PC) spectroscopy. The samples were silver epoxied to glass headers and then inserted into a socket on a cold finger inside the cryostat maintained between 4 and 7 K. Incident radiation from a Kr laser (15 mW) for PL measurements, or nearly monochromatic light from a grating spectrometer (0.5 nm FWHM) for the photocurrent measurements was focused at near normal incidence to the samples. The measured photoluminescence generated by the quantum well interband transitions was rapidly quenched by the electric field, preventing the measurement of the QCSE by PL. Photocurrent measurements, in contrast, showed good visibility for the interband transition peaks for large fields and yielded measurable Stark shifts. The PC data are used in the analysis for the QCSE and field dependence of the exciton binding energy.

3-2 Field dependent quenching of PL intensity

Photoluminescence versus applied bias measurements were performed on the four quantum well samples M049 through M052. Their structures are listed in Chapter 2 Table 1. The PL intensities for the four quantum wells were strong under flatband conditions (V_{bias}=1.2V) with narrow linewidths of less

than 5 meV FWHM. The application of an applied bias (electric field in the longitudinal direction) rapidly quenched the peak PL intensity by two orders of magnitude for fields as weak as 15 $kVcm^{-1}$, but with negligible linewidth broadening. The field dependence of the PL quenching for the 7.5 nm and 10 nm quantum wells is plotted in figure 14 (symbols). One mechanism for PL quenching is field induced tunnelling of the carriers from the quantum wells through the barrier layers. The calculated electron tunnelling lifetimes obtained from numerical calculations, Chapter 1 section 8, are plotted as solid curves in figure 13. The electron tunnelling lifetimes are an order of magnitude smaller than the heavy-hole tunnelling lifetimes, both of which are too large to be the cause of the PL quenching. Tunnelling lifetimes for the second confined heavy-hole level H2 are much less and may be the cause of the observed rapid quenching. Nevertheless, the rapid quenching of the PL intensity with the applied field makes this a difficult method for measuring the QCSE.

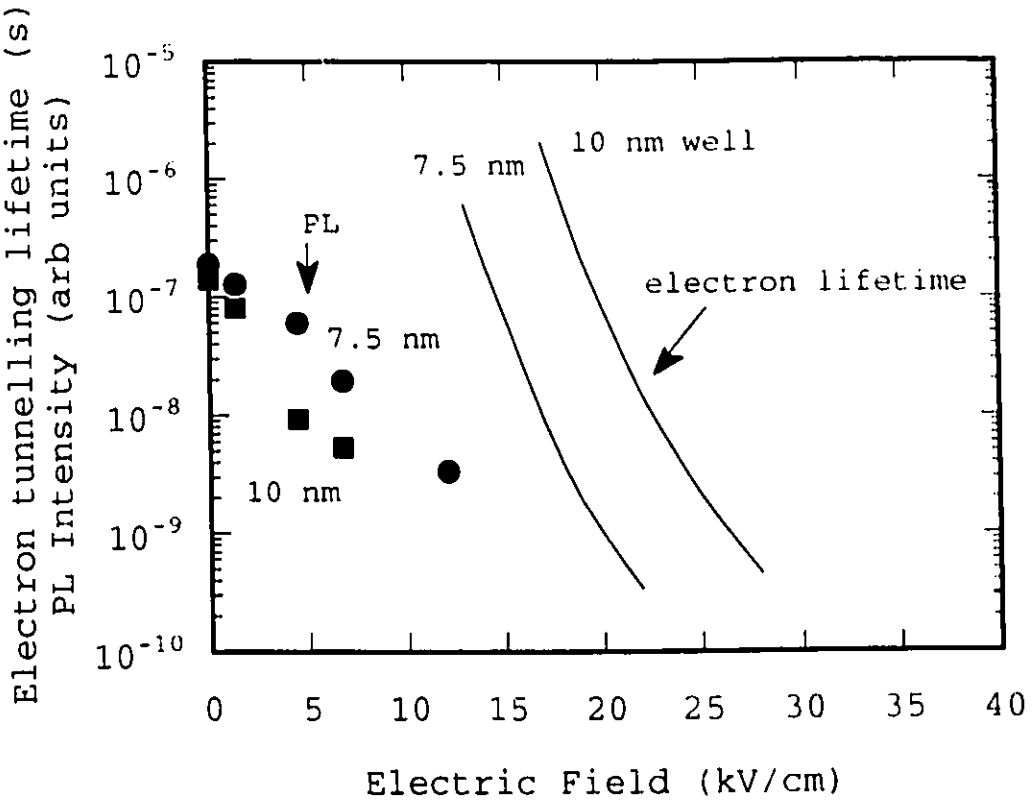

Figure 14. Field induced quenching of PL intensity, and calculated electron tunnelling lifetimes.

3-3 Photocurrent spectroscopy data

Photocurrent spectra for the four quantum wells were measured at 6K for applied biases ranging from 3 to 80 $kVcm^{-1}$. The spectra for the 7.5 nm quantum well at several reverse bias voltages is plotted in figure 15. The electric field, for a fully depleted pin diode, is calculated as the difference between the flatband voltage (1.2V) and the applied bias divided by the undoped layer thickness of 1.86 μm. The 3 $kVcm^{-1}$ bias spectrum shows a strong excitonic character for the low-field interband transition in the undoped GaAs buffer

layer at 1515 meV. The narrow exciton linewidth, 2.8 meV, reflects the high quality of the grown epilayers. The quantum well transitions are not visible for applied fields less than 12 kVcm^{-1} because the electrons and heavy-holes have insufficient energy to escape from the wells.

The sharp GaAs exciton transition is quickly washed out as the electric field is increased to 7 kVcm^{-1}. The product of this electric field and the zero field Bohr radius (a_0) of the exciton (15 nm) yields a bulk exciton binding energy $E_b=qFa_0$ [8] or 10 meV which is about double the accepted value for bulk GaAs. This suggests that for weak fields that the pin diode may not be fully depleted, leaving a weak residual field in the quantum well. However, at larger biases the diodes seem be fully depleted and the above calculation for the electric field appears be valid.

The symmetry allowed electron to heavy-hole transition (E1H1) at 1414 meV is just visible for the spectrum taken at the 12 kVcm^{-1} bias. At 39 kVcm^{-1} the E1H1 transition is clearly visible with a narrow linewidth of 4 meV indicating good quality growth for the quantum well. A small shoulder, labelled 'A' is visible at 1425 meV and may be the E1H1 interband transition. The energy difference between the E1H1 exciton transition and the shoulder 'A' suggests an exciton binding energy of 11 meV, higher than the calculated values near 8.5 meV (fig. 16). The E1H2, which is just discernible in the 17 kVcm^{-1} spectrum, is quantum mechanically forbidden at zero bias due to the odd symmetry of the overlap integral between the E1 and H2 levels. The application of a bias

distorts the zero field wavefunctions, resulting in a nonzero overlap integral. This results in a relaxation of the selection rules for the quantum well transitions permitting the E1H2 exciton transition to be observed. The oscillator strength for this forbidden transition should increase with the applied field, however the GaAs absorption edge masks this transition at the higher fields.

The E1H1 transition strengthens and reveals a red shift as the bias increases due to the quantum confined Stark effect. At fields larger than 65 $kVcm^{-1}$ the E1H1 interband transition begins to be quenched owing to the electron and heavy-hole levels no longer being confined in the quantum well. The field induced separation of the electron and hole wave functions reduces the overlap integral for the optical transition resulting in a weakened oscillator strength as well as broadening the photocurrent peak.

The measured E1H1 excitonic transitions at near flatband conditions for the four quantum wells were used to determine their well widths and alloy compositions. These measured excitonic transition energies were compared to the calculated values, with the alloy and well widths being adjusted in the calculations to obtain agreement. The four quantum wells were grown as a series using the same growth conditions, this allowed for a common alloy composition of 12.5% In to be determined to within 0.3% for the four wells. Similarly the epilayer thicknesses were obtained from a growth calibration of a thick epilayer. The calculated excitonic transition energies were obtained as the sum the E1 and H1 quantum

levels, the strained quantum well energy gap, less the exciton binding energy. The calculation for the eigenstate energies E1 and H1 is just the particle in a box problem, while the calculation of the zero field exciton binding energy is discussed below. The material parameters used in these calculations are taken from Landolt and Bornstein [66].

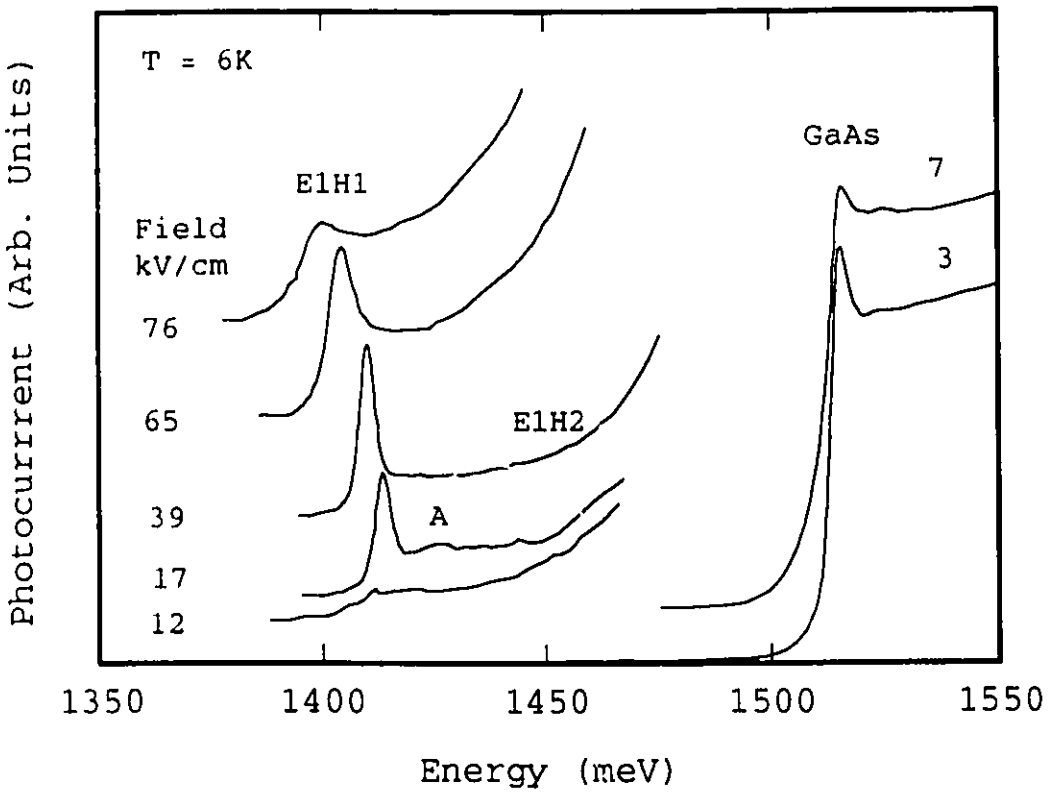

Figure 15. Measured photocurrent spectra for M051 at increasing applied fields.

3-4 Zero field exciton binding energy

The procedure for calculating the zero field exciton binding energy as a function of well width was outlined in Chapter 1. The separable trial function (equ. 56) is used in equation (59). Only the well materials are used in this calculation. This is necessary due to the integration of the Coulomb term over all space using the well dielectric constant, where decoupling this term to account for the differing well and barrier dielectric constants would add considerable difficulty. The use of the well masses for both the well and barrier regions shifts the ground state eigenenergies a few meV, however the shapes of the wave functions used in the calculation of the binding energy are not significantly altered.

The binding energy calculations are quite sensitive to both the dielectric constant ε and the reduced mass of the exciton μ. The dielectric constants for the well and barrier materials differ by less than 2% while there is considerable uncertainty in the value for the reduced mass. To first order the exciton binding energy E_b varies as $-2\delta\varepsilon/\varepsilon$ and $\delta\mu/\mu$. Perhaps the single greatest contribution to the uncertainty of the binding energy calculation is the reduced mass of the exciton, which is given by,

$$\frac{1}{\mu} = \frac{1}{m_e} + \frac{1}{m_0}(\gamma_1 + \gamma_2) \tag{63}$$

where γ_1 and γ_2 are the Luttinger parameters. This yields an exciton reduced mass of $0.038m_0$ when the heavy-hole mass of $0.08m_0$ at the Γ point is used. However, the heavy-hole mass

increases up to nearly $0.2m_0$ away from the Γ point, so that a more realistic average value of $0.16m_0$ is chosen in agreement with experimental results [67]. The conduction band is also distorted by the compressive strain in the $In_xGa_{1-x}As$ layer which modifies the in-plane effective mass of the electron. This results in a reduced mass for the exciton of $\mu=0.0469m_0$ which was used by Trzeciakowski and Roth [40] in their calculation of the exciton binding energy for a 12% $In_xGa_{1-x}As$-GaAs quantum well. The indium fraction for the four quantum wells, M049-M052, is 12.5% which is nearly the same, so a value of .0469 is used in these calculations.

The separable trial functions do not yield correct asymptotic values for the exciton binding energy either in the limit of zero or infinite well width, but do provide accurate values for the binding energy for well widths in the range of 3 to 15 nm. The binding energies in figure 16 are only slightly lower than those previously calculated by Trzeciakowski and Roth [40] who used a nonseparable trial function of the form (40), and agree well with recent magnetoluminescence data [41,68]. This variational method places a lower bound to the binding energy and hence the nonseparable trial function (equ. 55) provides a more accurate result.

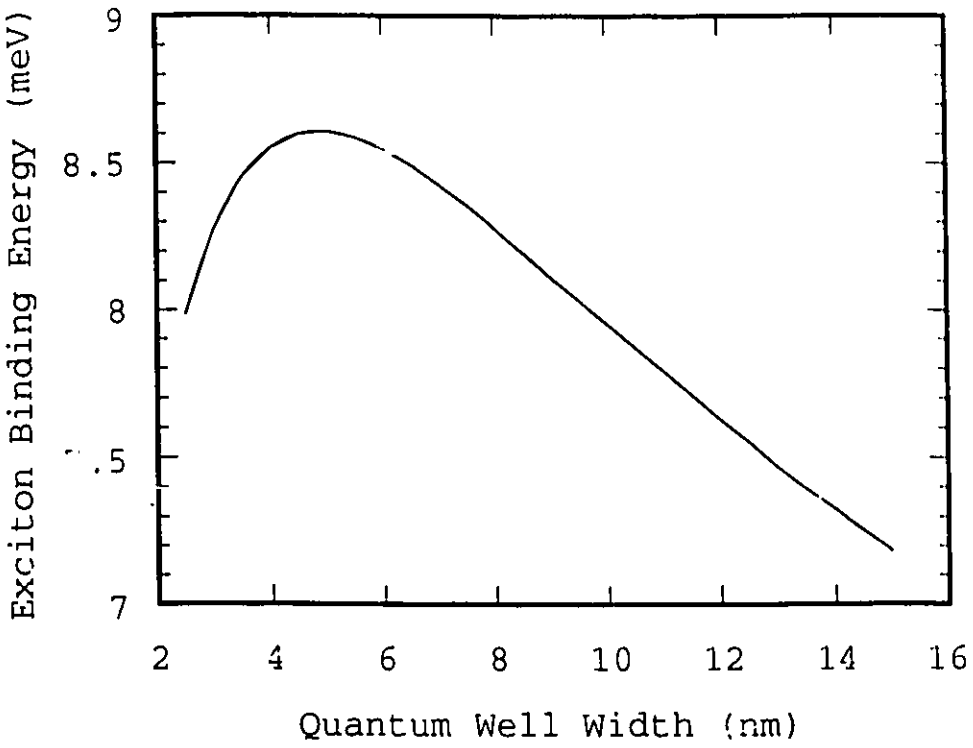

Figure 16. Exciton binding energies for the $In_{.125}Ga_{.875}As$ quantum wells calculated using the variational function (equ. 56).

3-5 Electric field dependence-QCSE

The measured excitonic transition energies, for the four quantum wells as a function of the applied field are plotted in figure 17. The calculated interband transition energies have been plotted as well (fig. 17 solid curves), their calculation is discussed in the next sections. All four samples show a quadratic field dependence for the quantum

confined Stark effect at weak fields. The 10 nm wide quantum well, M052, exhibits the strongest field dependence, with progressively weaker field dependences being observed for the narrower quantum wells. The spectra for the 2.5 nm quantum well was rapidly quenched by the applied field, preventing a reliable measure of its Stark shifting. A levelling off of the quadratic field dependence for the Stark shifted excitonic transition energy is observed for the 7.5 nm well at fields greater than 60 $kVcm^{-1}$, as well as for the 5.5 and 2.5 nm wells but now at weaker fields. This is attributed to the accumulation of carriers on the low energy side of the quantum wells.

The weak oscillator strength for the forbidden transition E1H2, in the 7.5 and 10 nm quantum wells, prevented a reliable measure for its field dependence. However an examination of the perturbational treatment for the infinite quantum well (eq. 22) suggests that the second heavy-hole level H2 should be weakly blue shifted, while the electron level E1 should be quadratically red shifted. The net field dependence of the E1H2 exciton transitions is the sum of these and may be either blue or red shifted with increasing applied fields.

The Stark effect was also observed for the E1H1 and E1H2 excitonic transitions for a 10 nm $In_{.135}Ga_{.865}As$-GaAs quantum well by Fortin et al. [69]. Van Eck et al. [3] using transmission measurements also observed a field dependent shift of the E1H1 excitonic transition for a 10 nm $In_{.13}Ga_{.87}As$-GaAs quantum well. Their transmission data was

later analyzed by Coffey [70] using a numerical calculation for the absorption coefficient, obtaining a nearly quadratic field dependence. P.W. Yu et al.[71] measured and calculated the Stark shifting of several exciton transitions in two 15 nm $In_xGa_{1-x}As$-GaAs quantum wells. Both quadratic and subquadratic field dependencies are visible for the lowest interband transition (E1H1) in their data. Higher order transitions between the allowed E2H2 and forbidden E1H2 and E2H1 levels revealed a more complex behaviour.

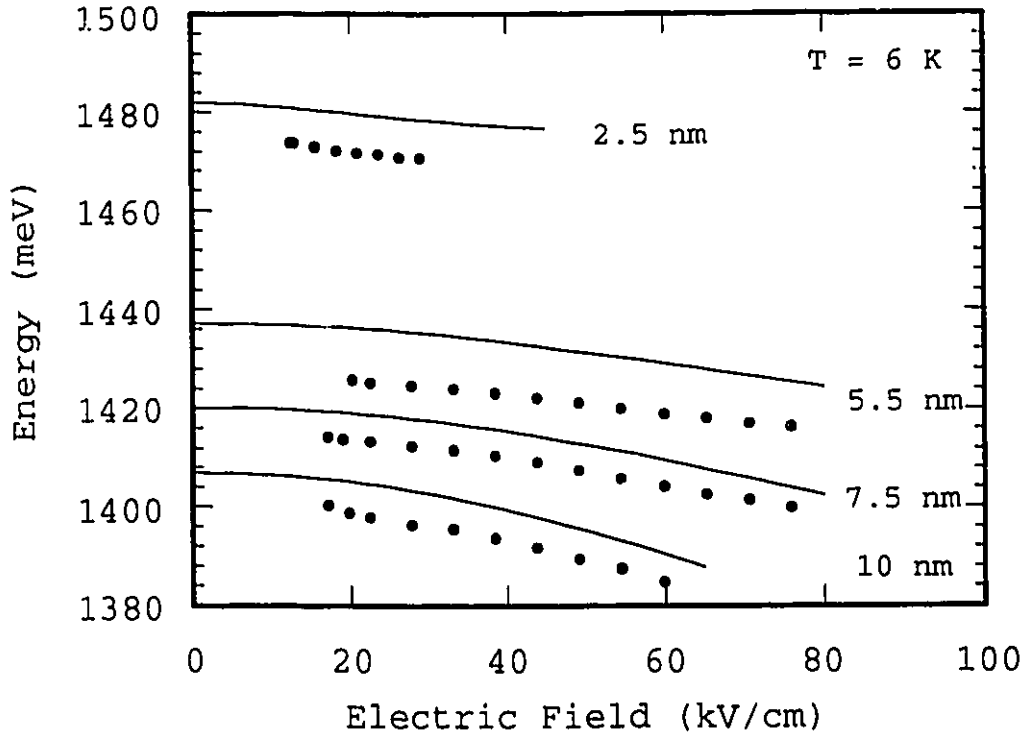

Figure 17. Measured exciton transition energies (symbols) and numerically calculated interband transition energies for the four $In_xGa_{1-x}As$-GaAs quantum wells M049-M052.

3-6 Variational calculation of the QCSE

The quantum confined Stark effect is calculated for the lowest lying electron and heavy-hole levels, E1 and H1 respectively, for four quantum wells using the two variational methods and the numerical integration methoddescribed in the Chapter 1, section 8. The variational trial function utilizing the linear prefactor (equ. 24) yields an expected quadratic electric field dependence (equ. 25) but with the second moment $\langle z^2 \rangle_0$ now being given by equation (28). The calculated QCSE dependencies for the four quantum wells M049-M052 are plotted in Figure 18 (solid curves). The quadratic field dependence is expected due to the odd nature of the trial function. This variational calculation also yields a nearly fourth power well-width dependence of the QCSE for wells wider than 6 nm. At narrower widths, the electron and hole wave functions increasingly extend outside the wells enhancing the QCSE. This can be shown using equation (28) in Chap. 2 where the second moment $\langle z^2 \rangle_0$ diverges as the well width is reduced towards zero. This results in a QCSE that is large for narrow and wide wells, having a minimum for wells of 6 nm width.

The QCSE was also calculated for the four quantum wells using the exponential prefactor in the trial wavefunction (equ. 27). The QCSE was solved by numerically integrating the overlap integrals in equation (27) and using the variational parameter β as a free variable to obtain a minimum energy. The calculations performed for the 7.5 and 10 nm wide quantum wells using the exponential prefactor give nearly identical

results (Figure 18 dotted curves) to those obtained with the linear prefactor (Figure 18 solid curves).

Only the well material parameters are used in the two variational calculations in order to permit comparison between the two methods. The use of the well material parameters shifts the zero field eigenstate energies by several meV, though the impact on the magnitude of the field dependence of the QCSE is minimal. The quantum well masses are obtained by linearly interpolating the electron and heavy-hole masses of the two binaries GaAs and InAs. An electron mass of $m_e^*=.0663m_0$ and heavy-hole mass of $m_{hh}^*=.346m_0$. are obtained for the quantum wells. The 65:35 band offset ratio gives electron and heavy-hole potential wells of V_e=93.3 mV and V_h=49.7 mV respectively.

The variational method using the linear prefactor was also used for the second confined levels E2 and H2 using the sine function, first excited state, instead of the cosine ground state wave function. The QCSE obtained using this trial function is too large when compared to the numerically calculated QCSE. The assumption that the field perturbation to the zero field wave function being small may no longer be valid, and this variational method yields erroneous results.

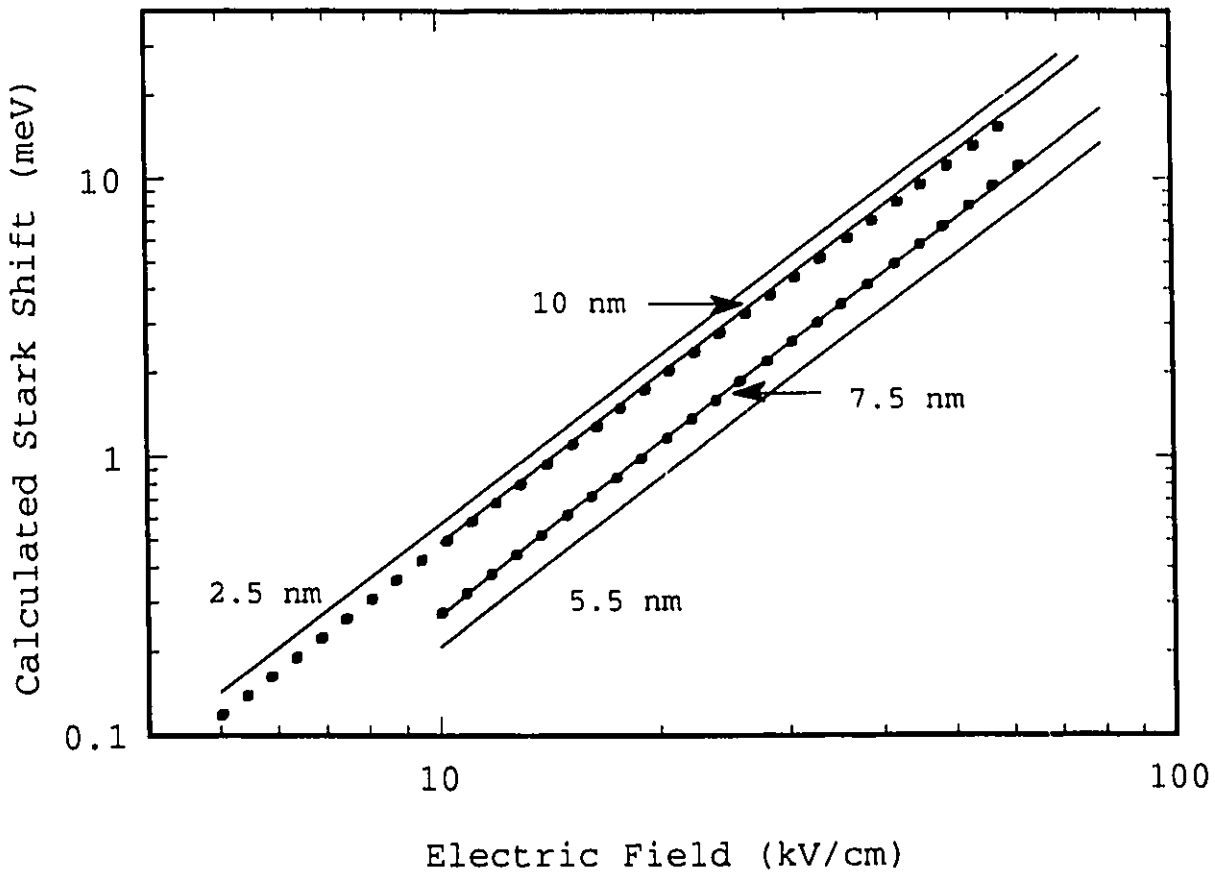

Figure 18. Variational Calculation of the QCSE for the four $In_xGa_{1-x}As$-GaAs single quantum wells using a linear prefactor (solid lines) and exponential prefactor (dotted lines). Only the well material parameters have been used where $m_e = .0663m_0$, $m_h = .346m_0$, $V_e = 93.3$ mV, $V_h = 49.7$ meV.

3-7 Numerical calculation of the QCSE

The variational trial functions are most accurate for weak fields and wide wells. To extend solutions for the quantum-well problem to high electric fields the numerical integration method described in Chapter 1, section 8 is used. This algorithm calculates the field-dependent quantum levels using complex wave functions for both well and barrier regions. Both the well and barrier material parameters are used in these calculations to obtain the exact QCSE plotted in figure 19. Good qualitative agreement is achieved between the numerical solution for the QCSE and the variational calculations for the wide wells and weak fields. This agreement breaks down at high fields and is most strongly displayed for the 2.5 nm well. Whereas the variational calculations both predict a quadratic field dependence, the numerical calculation shows a more complex behaviour, with the eigenstate energy tending to saturate. This same effect is obtained for the wider wells, becoming progressively weaker. This reduction in field dependence of the QCSE is due to carrier accumulation at the low energy side of the quantum wells [17].

The calculated interband transition energies plotted as the solid curves in figure 17 are the zero field eigenstate energies E1 and H1 less the numerically calculated Stark shifts. These calculated curves show good agreement with the measured excitonic transition energies. In particular, both reveal the high field saturation to the quadratic field dependence to the QCSE.

The calculated interband energies plotted in figure 17 are the sum of the strained $In_xGa_{1-x}As$ bandgap (equ. 1), plus the field dependent eigenstate energies for the electron and heavy-hole states as calculated using the numerical integration algorithm. The measured and calculated field dependencies for the exciton (fig. 17 symbols) and interband (fig. 17 solid curves) transition energies are quite similar. The energy differences between the two is due to the exciton binding energy which ranges from 6 to 10 meV for these samples, in good agreement with the calculated value of 8.5 meV as plotted in figure 16.

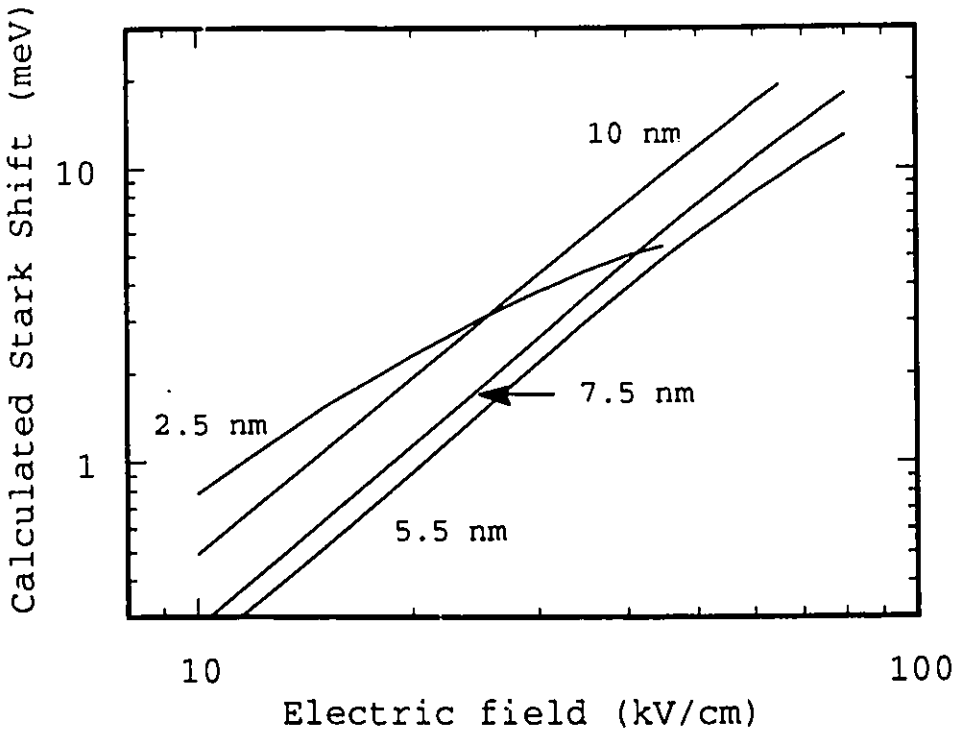

Figure 19. Exact numerical calculation of the QCSE for the four quantum wells. Both the well and barrier material parameters have been used to calculate these curves. Well depths and masses are the same as in Figure 18. Barrier masses are now .0665 and .370m_0 for the electrons and heavy-holes respectively.

3-8 Calculated field dependent exciton binding energies

The energy differences between the calculated interband transition energies and the measured excitonic transitions in figure 17 yield a measure of the field dependent exciton

binding energies. Alternately the field dependent exciton transition energies may be obtained using the calculated interband transition energies plotted in figure 17 less the calculated field dependent exciton binding energies.

The process for calculating the field dependent exciton binding energies is the same as for the zero field case except for the addition of the variational prefactors used to account for the electric field. The trial functions (equ. 60 and 61) are used in the double integration of equation (59) to obtain the field dependent exciton binding energies. These calculations are performed for the 5.5, 7.5 and 10 nm wide quantum wells with the calculated energies plotted in figure 20.

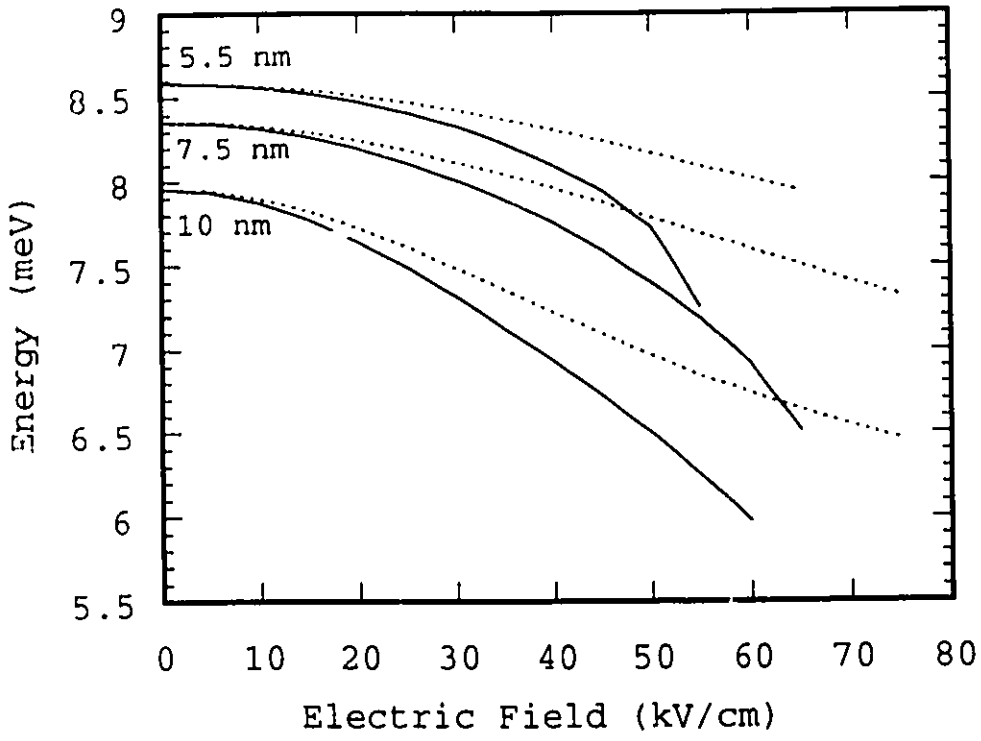

Figure 20. Calculated field dependent reduction to exciton binding energies for the $In_xGa_{1-x}As$-GaAs quantum wells. Calculations using linear prefactor are plotted as dashed lines, while results obtained with exponential prefactor are represented by the solid lines.

The calculated binding energies utilizing the linear trial function (figure 20 dashed curve) are weakly reduced by the electric field. The exciton binding energy for the 5.5 nm well is reduced by 0.5 meV at an applied field of 65 $kVcm^{-1}$. The same field reduces the exciton binding energy for the 10 nm well by 1.3 meV. This field dependent reduction to the binding energy seems to saturate at large fields greater than

60 kVcm^{-1}. The exponential trial function, in contrast, shows a continuous reduction in the binding energy (fig. 20 solid curves) of nearly 2 meV for fields approaching 60 kVcm^{-1}. This increased field dependence obtained with the exponential trial function is due to the small barrier heights of the potential wells confining the electrons and heavy holes in the $In_xGa_{1-x}As$ quantum wells. The reduced confining potentials enhance the polarizability of the excitons making their binding energies sensitive to applied fields [42].

The minimization process used to obtain the field dependent binding energies is first done with respect to β_z and β_ρ to obtain the QCSE, and then over λ. The maximum value for E_b is sought for in each calculation. This process does not give any indication as to whether the linear or exponential trial function is more valid, since the three parameters are not simultaneously minimized. A comparison between the shapes of the trial wave functions and the numerically solved wave functions gives a better agreement to the exponential trial function (61). These trial functions were used to calculate the field dependent exciton binding energy for a series of $Al_xGa_{1-x}As$-GaAs quantum wells by Gibb and Roth [45] showing good agreement with the results of Brum and Bastard [42] and Hong and Singh [44].

The calculated and measured exciton transition energies for the 5.5, 7.5, and 10 nm $In_xGa_{1-x}As$-GaAs quantum wells are plotted in figure 21. The excitonic energies are calculated as the sum of the field dependent quantum well eigenstate

energies, the strained $In_xGa_{1-x}As$ bandgap, less the calculated exciton binding energies using the exponential trial function. The results for the 10 nm quantum well agree extremely well, while the measured excitonic energies for the 5.5 and 7.5 nm wells differ by about 2 meV from the calculated values

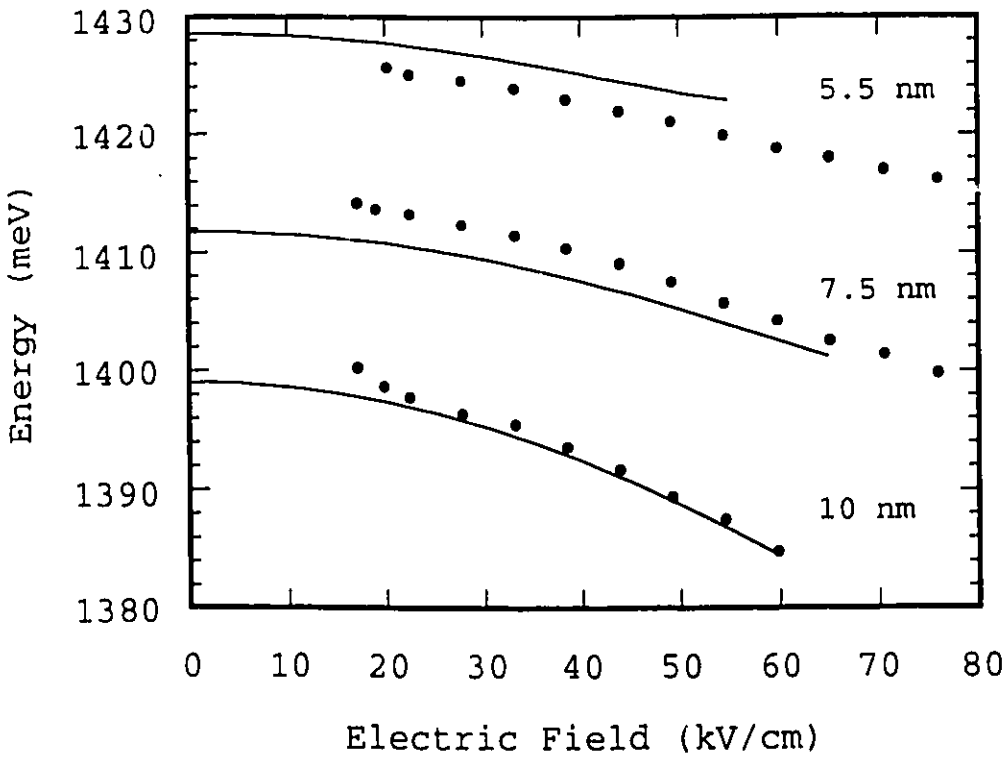

Figure 21. Measured and calculated exciton transition energies for the 5.5, 7.5 and 10 nm wide $In_xGa_{1-x}As$-GaAs quantum wells.

The agreement between the calculated and measured excitonic transition energies is quite good considering the uncertainties associated with the material properties of the samples. The zero field interband transition energy E1H1 is

quite sensitive to the strained $In_xGa_{1-x}As$ well energy gap as determined by its indium fraction. For example a change of 0.25% in indium composition results in a 3 meV change in the well energy gap, while the eigenstate energies E1 and H1 change by less than 0.5 meV and 0.1 meV respectively. The uncertainty in layer thickness is on the order of a single GaAs epilayer (0.5 nm) which can cause the 10 nm quantum well eigenstate energies to shift by as much as 2 meV and alter the Stark shift by 2%. The effects of these uncertainties is worse for the narrower wells. Finally the magnitude of the electric field is accurate to within 10%.

3-9 Summary

A systematic study of the effects of the quantum confined Stark effect has been made on a series of four quantum wells. The field dependent photocurrent spectra reveals sharp excitonic peaks due to the first confined E1H1 interband transitions. Both the E1 and H1 quantum levels exhibit a quadratic red shift with increasing field. The magnitude of this effect increases with well width for wells wider than 6 nm. The magnitude of this effect is in good agreement with a single particle calculation, and over a limited field range using several variational methods. Calculations of the field dependent exciton binding energy are supported by the measured data.

Chapter 4

Experimental Results for the Superlattices

4-1 Introduction

Three superlattice samples, H145, L121 and L073, whose structures are listed in Chapter 2 Table 2, were fabricated as Schottky diodes. These samples were examined using photoluminescence (PL), photoluminescence excitation (PLE), photocurrent (PC) and electroreflectance (ER) spectroscopy at 4.5K. The PL, PLE, and low field PC data were used to characterize the samples' structures, while the photocurrent and electroreflectance data revealed the Stark ladder formation and Stark localization. The three superlattice samples H145, L073, and L121 have similar superlattice periods ranging from 10 to 11.5 nm. The indium alloy fractions of the wells range from 6.5% to 16.2% for the three samples, strongly affecting interwell coupling and hence the observed optical features.

The degree of interwell coupling for the electrons, heavy-holes, and light-holes in the three superlattices is linked to their miniband-widths, the energy difference between the mini-zone edge and mini-zone centre. Both the first electron miniband Γ and π points for L121 are confined as shown in figure 22, having a miniband-width of 16 meV. The second electron minizone edge level ($E\pi 2$) is just above the confining potential. Both the first heavy-hole minizone centre and edge, $H\Gamma 1$ and $H\pi 1$, are nearly coincident in energy and are confined in the heavy-hole superlattice potential. The first light-hole minizone centre, $L\Gamma 1$, is also confined.

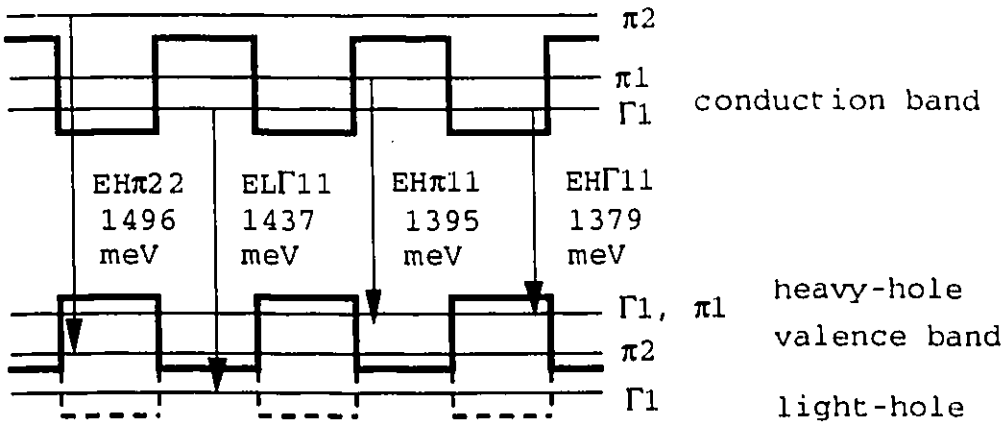

Figure 22. Energy diagram for L121 including calculated interband transition energies.

The electron miniband-width for H145 is 25 meV with its Γ and π points confined in the superlattice (fig. 23A). The heavy-hole miniband-width is 1 meV and is confined to the heavy-hole superlattice potential. The three observed excitonic transitions for H145 are indicated in the figure. The electron miniband-width for L073 is approximately 42 meV with the π point being unconfined (fig. 23B). The heavy-hole miniband-width is 4 meV being confined to the heavy-hole superlattice potential. The small miniband-widths for the heavy-holes for all three samples suggest that these states are strongly localized in each well, while the increased electron miniband-widths indicate strong electron interwell coupling. L073 having the strongest interwell coupling exhibits the most pronounced Stark ladders, while L121 having little interwell coupling displays the weakest optical features for the Stark ladders of the three samples.

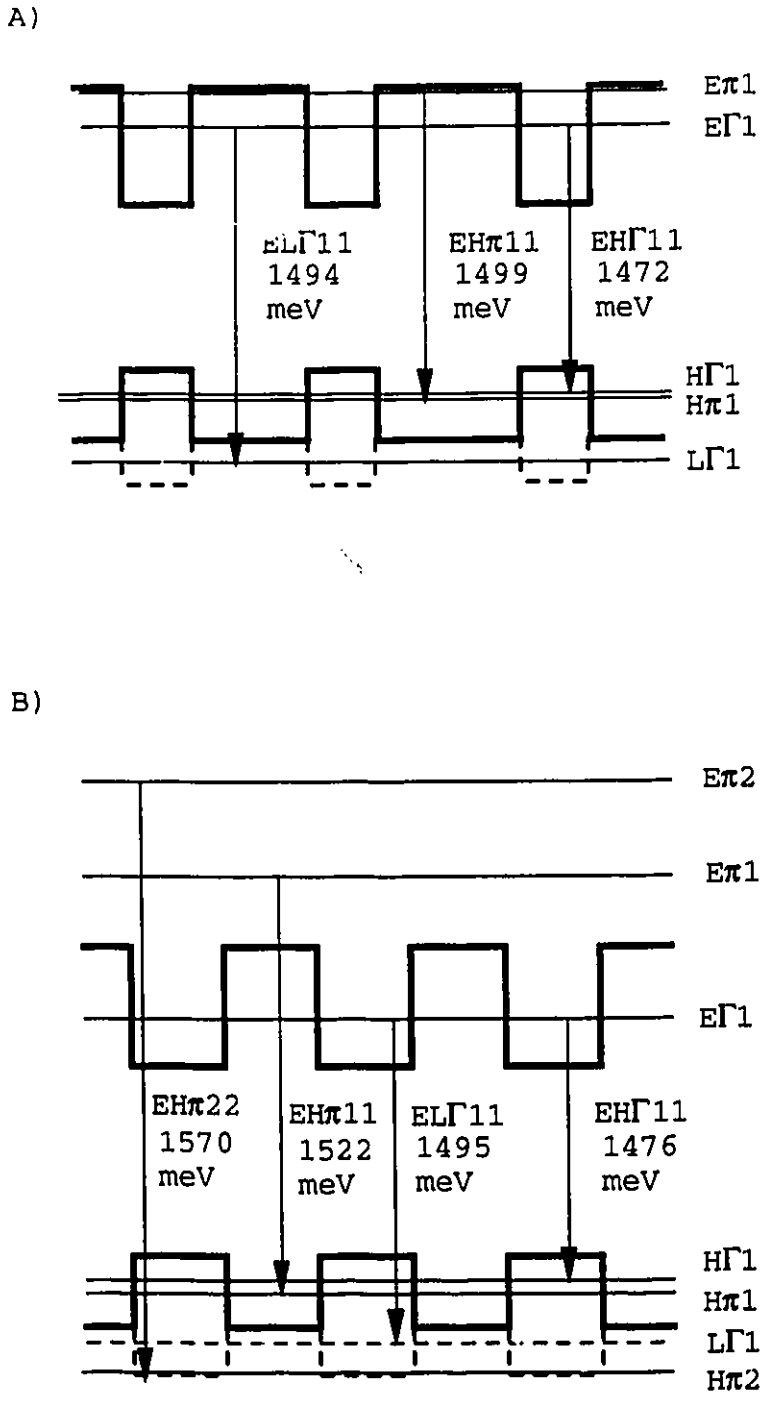

Figure 23. Superlattice potentials and interband transitions for A) H145, B) L073.

4-2-1 Low Field Spectra for Sample L121

The sample L121 was the most extensively studied of the three superlattice structures. PL, PLE, PC, and ER measurements were made on the same sample as the x-ray measurements mentioned in Chap 2. 4.5K PL and PLE measurements were performed prior to the fabrication of L121 into Schottky diodes. The photoluminescence measurements were performed using the 30 mW excitation from a Ti:Sapphire laser, set to 850 nm, below the absorption edge of the GaAs substrate. The PLE emission, from the low energy side of the lowest energy PL peak (EHΓ11), was selected by the spectrometer set to 907.5 nm with a 0.5 nm resolution. The Ti:sapphire wavelength was then scanned from 850 to 900 nm. The Ti:Sapphire laser was used for both the PL and PLE experiments to ensure that the same portion of the sample was being examined. The zero field PL, PLE, weak field electroreflectance and PC spectra are shown in figure 24. Both the PL and PLE spectra exhibit weak PL emission due to the low absorption of the Ti:Sapphire laser radiation by the superlattice. By the same token the Ti:Sapphire radiation is illuminating the cap, buffer, superlattice structure, as well as the n' substrate. This results in a weak broad background PL emission in addition to the sharp exciton emission from the first electron to first heavy-hole mini-zone centre (EHΓ11) interband transition at 1372 meV. This is slightly Stokes shifted (3 meV) from the PLE data, indicating recombination possibly involving impurities.

The PLE spectrum has in addition to the EHΓ11 peak at 1375 meV, shows structures at higher energies which are identified as the first electron to light-hole exciton transition

(ELΓ11) at 1439 meV. A peak is observed at 1394 meV which is close to the calculated first electron to first heavy-hole mini-zone edge (EHπ11) interband transition. The flatband voltage for the three superlattice samples ranges from 0.8 to 0.9V, at bias greater than 0.4V the exciton transitions observed in the PC spectra are reduced in intensity, eventually merging with the background photocurrent signal. The PC spectrum, taken at 0.4V bias has the same two major peaks at 1377 and 1438 meV as observed in the PLE spectrum. The PC data also reveal the second electron to second heavy-hole mini-zone edge (EHπ22) exciton transition at 1491 meV. The electroreflectance spectrum, taken at 0.75V bias, reveals peaks consistent with the above interband transitions appearing to be first derivative like with respect to energy. However this cannot be confirmed without curve fitting using the lineshape function given by equation (62). The energies of these exciton peaks from the PL, PLE, and weak field PC spectra are listed in table 4. The agreement between excitonic transition energies obtained from the PLE and PC data is quite good. This is to be expected since both provide a measure of the absorption spectra.

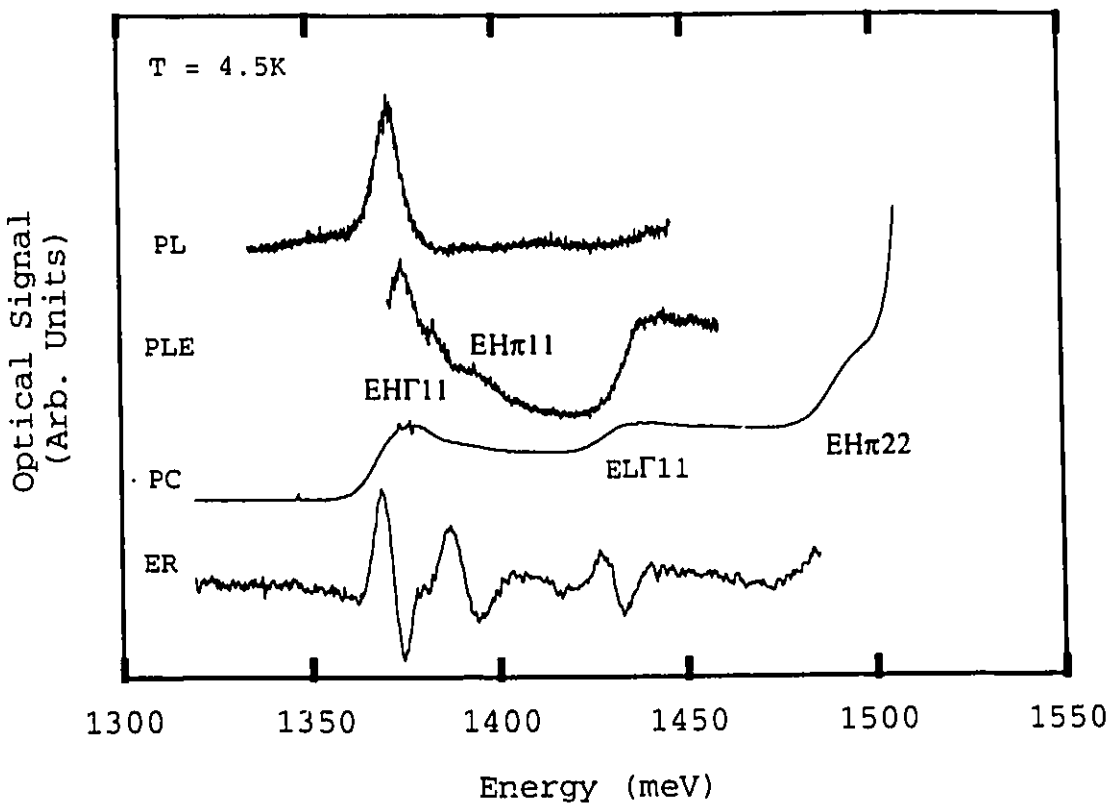

Figure 24. PL, PLE, PC, and ER Spectra for L121.

The interband transition energies for L121 are calculated using Bastard's envelope formalism [13] with the layer thicknesses and alloy compositions being obtained from the x-ray data and growth conditions, as well as from fitting the PC and PLE data. These interband transition energies are listed in table 4. The lattice constants, effective masses, and bandgaps used in these calculations are interpolated from Landolt-Bornstein [66]. The indium fraction in the wells varies slightly across a grown wafer, with this in mind the interband transition energies are also calculated for a well

indium fraction of 17%, up slightly from the x-ray measurements of 16.2%. This results in a better agreement between the measured exciton transition energies and the calculated interband energies, where a 4 to 5 meV exciton binding energy is used for the EHΓ11 exciton transition. This binding energy for the superlattice should be close to the $In_xGa_{1-x}As$ bulk value of about 4 meV [9]. Dignam and Sipe [47] calculate exciton binding energies of 5 meV and 8 meV for a 10 nm and 12 nm period $Al_{.3}Ga_{.7}As$-GaAs superlattice respectively. This suggests that the 4 to 5 meV exciton binding energy used for the $In_xGa_{1-x}As$-GaAs superlattices studied here is not unreasonable.

Table 4

Excitonic and interband transition energies for L121 in meV

	measured			calculated	
				from	fitted
transition	PLE ±2	PL ±1	PC ±2	x-ray	17%
EHΓ11	1375	1372	1377	1386	1379
EHπ11	1394			1402	1395
ELΓ11	1439		1438	1442	1437
EHπ22			1491	1499	1496

4-2-2 Low field spectra - H145 and L073

The 4.5K weak field photocurrent and electroreflectance spectra for H145 are plotted in figure 25. The PC spectrum taken at 0.5V bias has two peaks which are identified as the heavy-hole mini-zone centre exciton transitions (EHΓ11) at 1468 meV, and broad peak at 1490 meV which appears to be a mixture of the heavy-hole mini-zone edge (EHπ11) and the light-hole zone centre (ELΓ11) exciton transition. The peak labelled 'B' at 1475 meV is at the same energy as the p=0 Wannier Stark ladder which strengthens as the applied electric field is increased (see below section 4-3-2). The electroreflectance spectrum taken very near flatband conditions (0.75V) reveals a slightly red shifted EHΓ11 transition near 1465 meV. This red shift is expected as the reduced electric field causes the transitions to merge towards the zero-field energies. The peak labelled B is estimated to be at 1475 meV, the same as obtained from the PC spectrum. The presence of this peak is unexpected since Bleuse's tight binding model requires the p=0 Stark ladder to disappear under flatband conditions. The ER spectra shows two strong features at the EHΓ11 and EHπ11 transition energies, as well as additional unidentified weak oscillations . The ER spectrum also displays the GaAs bandedge exciton transition near 1513 meV.

The measured exciton and calculated interband transition energies are presented in table 5. The x-ray measurements for H145 yield a superlattice period of 11.6 nm with an average alloy composition of 3.2% for the whole structure. The x-ray measurements were not performed on the same sample as was used for the optical experiments. Here a well width

of 2.5 nm and barrier width of 9.0 nm are used in the calculations, with the alloy composition of the wells being adjusted to 12.8% In to obtain a fit to the PC spectrum. This alloy composition for the wells yields an average of 2.8% for the whole structure, down slightly from the x-ray data of 3.2%.

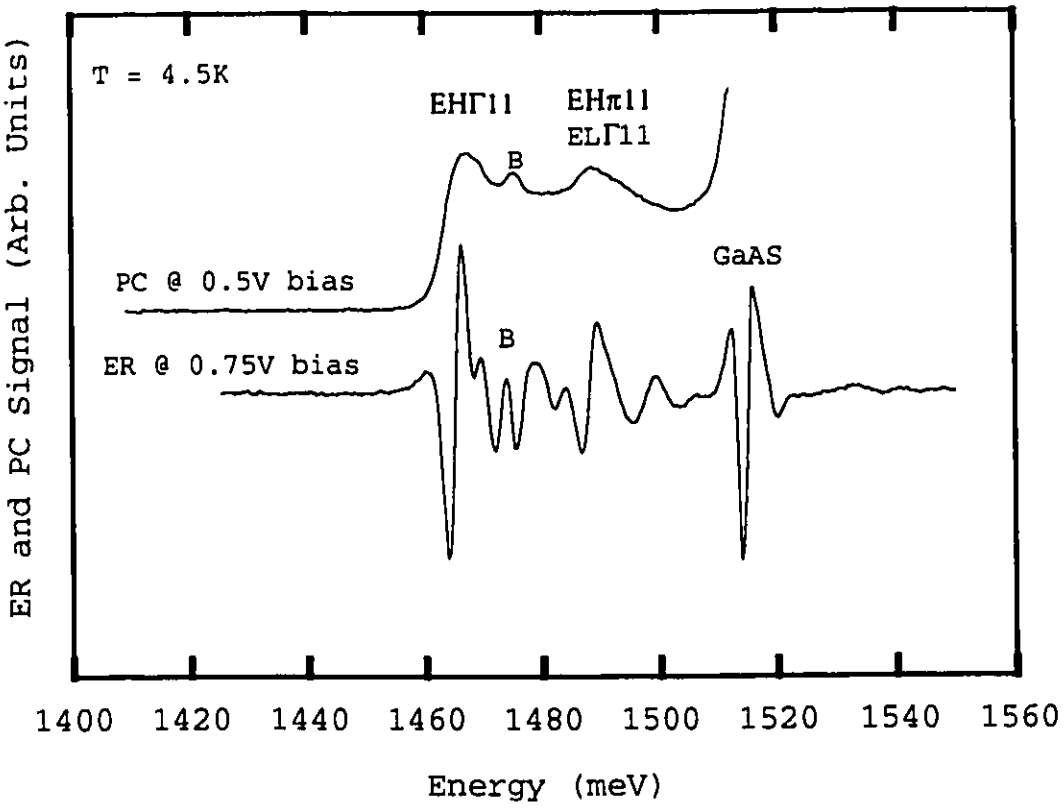

Figure 25. Low field PC and ER spectra for H145.

Table 5

Exciton and interband transition energies for H145. Calculations performed for $In_{.125}Ga_{.875}As$ with a 9 nm barrier and 2.5 nm well.

Transition	Calculated (meV)	measured PC (±1 meV)
EHΓ11	1472	1468
EHπ11	1499	1490 mixture
ELΓ11	1494	
B		1475

The weak field photocurrent spectrum for L073, plotted in figure 26, exhibits the two confined exciton transitions for the heavy-hole (EHΓ11), and light-holes (ELΓ11) at 1470 and 1490 meV respectively. A peak labelled 'B' is observed at 1482 meV which is at the same energy as the p=0 Wannier Stark ladder, indicating that the applied field of 3 $kVcm^{-1}$ has initiated the Wannier Stark localization. The electroreflectance data taken at 0.8V bias and plotted in figure 26 reveals quite complicated structure. However it is possible to correlate several of the structures with the exciton transitions observed in the PC spectrum. In addition, an intense ER signal is seen for the GaAs exciton transition as well as an adjacent weak structure possibly due to the mini-zone edge exciton transition EHπ11. The second electron to heavy-hole excitonic transition EHπ22 is observed near 1560 meV, indicating a miniband-width of 48±8 meV in good agreement with the calculated value of 46 meV. The measured exciton transition and calculated interband transition energies for L073 are listed in table 6.

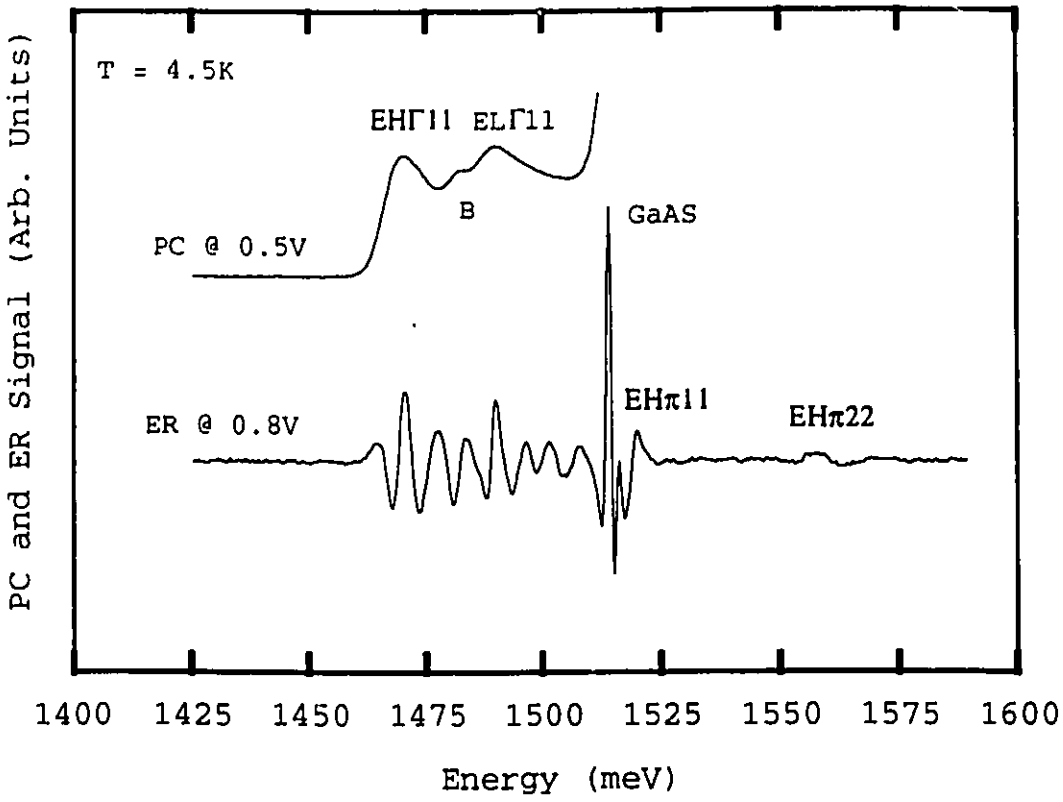

Figure 26. Electroreflectance and photocurrent spectra for L073 taken near flatband conditions.

Table 6

Exciton and interband transition energies for L073

transition	Calculated (meV)	measured PC (±1 meV)
EHΓ11	1476	1470
ELΓ11	1495	1490
EHπ11	1522	
EHπ22	1570	
B		1482

4-3 Field dependent spectra - Wannier Stark ladders

The weak field spectra for the three superlattices, plotted in figures 24-26, reveal optical features associated with the superlattice at flatband conditions. The application of an electric field in the longitudinal or growth direction now induces Stark localization of the electrons and the formation of Wannier Stark ladders which are observable in both the photocurrent and electroreflectance spectra. The ER and PC spectra for the three samples as a function of the applied bias are discussed below.

4-3-1 PC and ER field dependent spectra for sample L121

The bias dependent photocurrent spectra for sample L121 are plotted in figure 27 for biases ranging from 0.4V (4 $kVcm^{-1}$) to -1.4V (25 $kVcm^{-1}$). The near flatband spectrum, V_{BIAS} = 0.4V shows the superlattice excitonic transitions EHΓ11, ELΓ11 and EHπ22. Increasing the applied field causes the structure at

1377 meV to increase in intensity, emerging as the p=0 electron to heavy-hole Wannier Stark ladder. A weak shoulder on the low energy side of the p=0 ladder is seen to move to lower energies with bias and is identified as the p=-1 ladder. The p=0 ladder is seen to grow in intensity, while the p=-1 ladder is reduced in intensity as the applied field is increased. This is caused by the field induced localization of the wave functions into single quantum well like states, where the overlap integral between electron and heavy-hole states in the same wells increases, and overlap between adjacent wells is diminished by the application of a field.

A peak is also observed to form on the high energy side of the p=0 ladder at 1391 meV, labelled A'. The energy of A' is consistent with the calculated zero field EHπ11 interband transition. However, it should not survive at large electric fields. The nature of this peak will be discussed later. The weak field ELΓ11 exciton transition broadens as the field is increased, with a weak but observable blue shift.

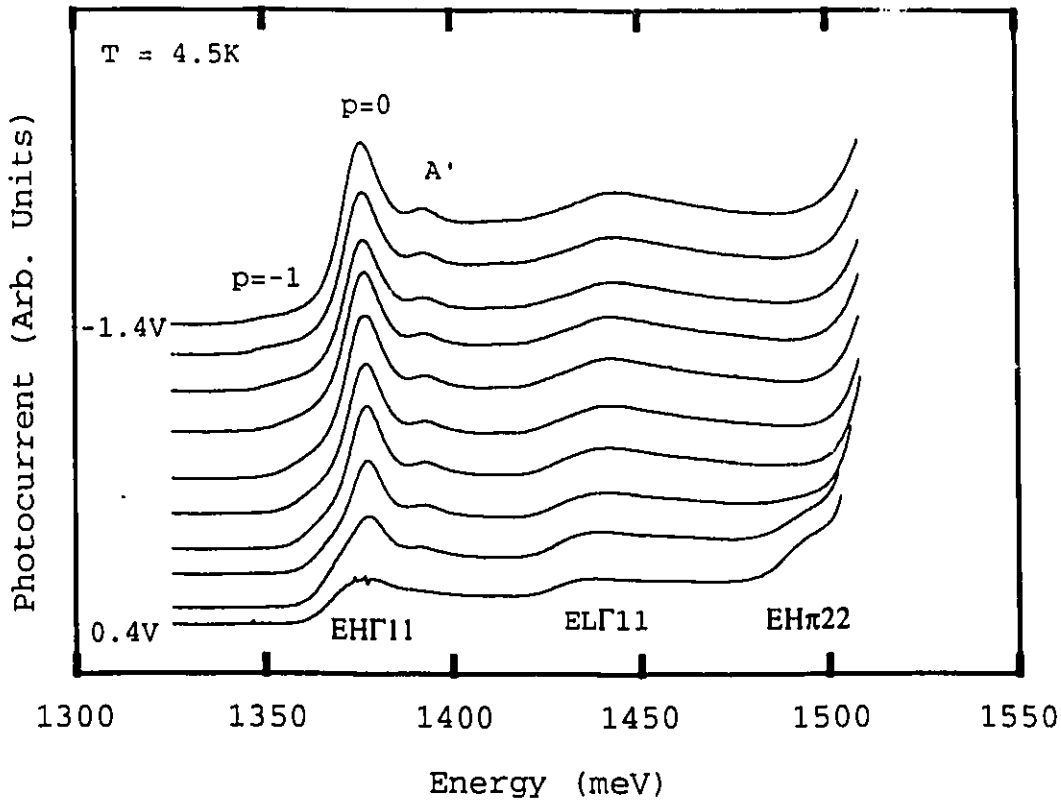

Figure 27. PC spectra for L121 versus applied bias. Bias steps are every 0.2V.

The electroreflectance data for L121 at several bias voltages are plotted in figure 28. The near flatband, V_{BIAS} = 0.75V, spectrum reveals the three confined exciton transitions, Γ11, EHπ11, and ELΓ11. Structures consistent with the p=0 and p=-1 ladders are clearly visible as the reverse bias applied to the sample is increased. A weak shoulder splits away from the p=0 ladder towards higher energies and is identified as the p=1 Stark ladder. This ladder was not visible in the PC spectra. The electron to light-hole mini-

zone centre exciton ER structure near 1430 meV appears to split into 2 structures as the bias is increased to -1.25V, indicating the formation of the p=-1 and 1 light-hole Wannier Stark ladders. Finally a weak structure, A', is seen on the high energy shoulder of the p=0 Stark ladder similar to that observed in the PC data.

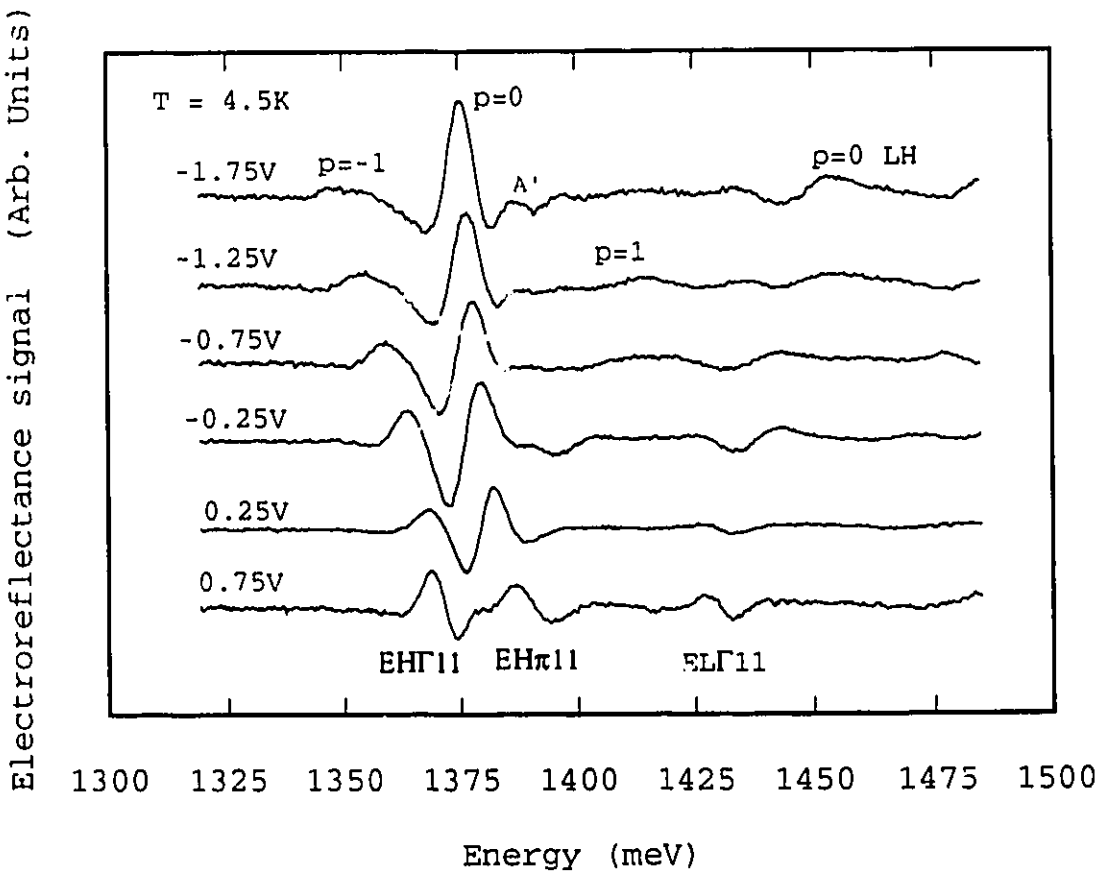

Figure 28. Bias dependence of ER spectra for L121 showing formation of Wannier Stark ladders.

4-3-2 PC and ER field dependent spectra for H145

The field dependent photocurrent spectra for H145, taken at 0.25V increments, are plotted in Figure 29, with the near flatband spectrum taken at 0.5V bias displaying the superlattice transitions EHΓ11, ELΓ11, and EHπ11. The p=0 Stark ladder emerges from the peak 'B' in the 0.5V spectrum as the field is increased towards the -2.5V bias. This suggests that at the 0.5V bias or 1.3 $kVcm^{1}$ field has already initiated the Stark ladder localization. The peak associated with the ELΓ11 and EHπ11 transitions first undergoes a slight red shift, then moves towards higher energies as the p=1 Stark ladder The EHΓ11 peak in the 0.5V spectrum is seen to split into several structures in the 0.25V and 0V spectra, then red shift as the p=-1 and -2 Stark ladders, and a weak peak labelled 'c'. The feature labelled c is due to Coulomb interactions between the Stark ladders, and is also observed in sample L073, and other $In_xGa_{1-x}As$-GaAs [72] and $Al_xGa_{1-x}As$-GaAs superlattices [35]. Finally a weak shoulder, labelled 'A' at 1482 meV, on the high energy side of the p=0 Stark ladder is seen at large applied fields. The origin of the shoulder is not known, though it has been observed in several InGaAs superlattices including: samples L120, L121, by Soucail et al.[11] and by Saker et al. [72]. The structures A and c will be discussed more fully in Chapter 5.

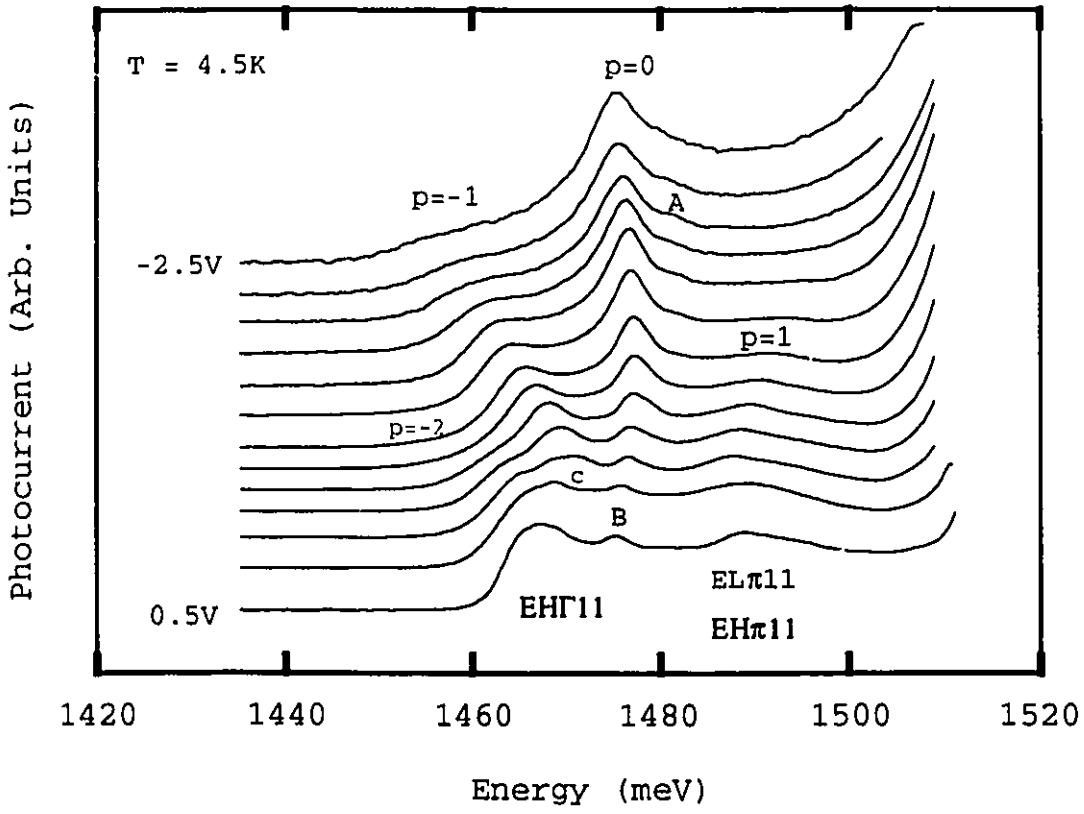

Figure 29. Bias dependent photocurrent spectra for H145. Bias increment is 0.25V.

The bias dependent electroreflectance spectra for H145 are plotted in Figure 30. The near flatband spectra taken at 0.75V bias reveals a quite complex behaviour with structures due to the superlattice exciton transitions being clearly visible. A number of additional features are also seen but have not been identified. Increasing the applied field results in a strong peak forming near 1475 meV which is the p=0 Stark ladder. Two structures on the low energy side are

seen to split away as the field is increased and are assigned as the p=-1 and -2 Stark ladders. In a similar fashion the p=1 Stark ladder undergoes a strong blue shift on the high energy side of the p=0 ladder. The applied field simultaneously quenches the GaAs exciton ER signal, indicating its field induced ionization.

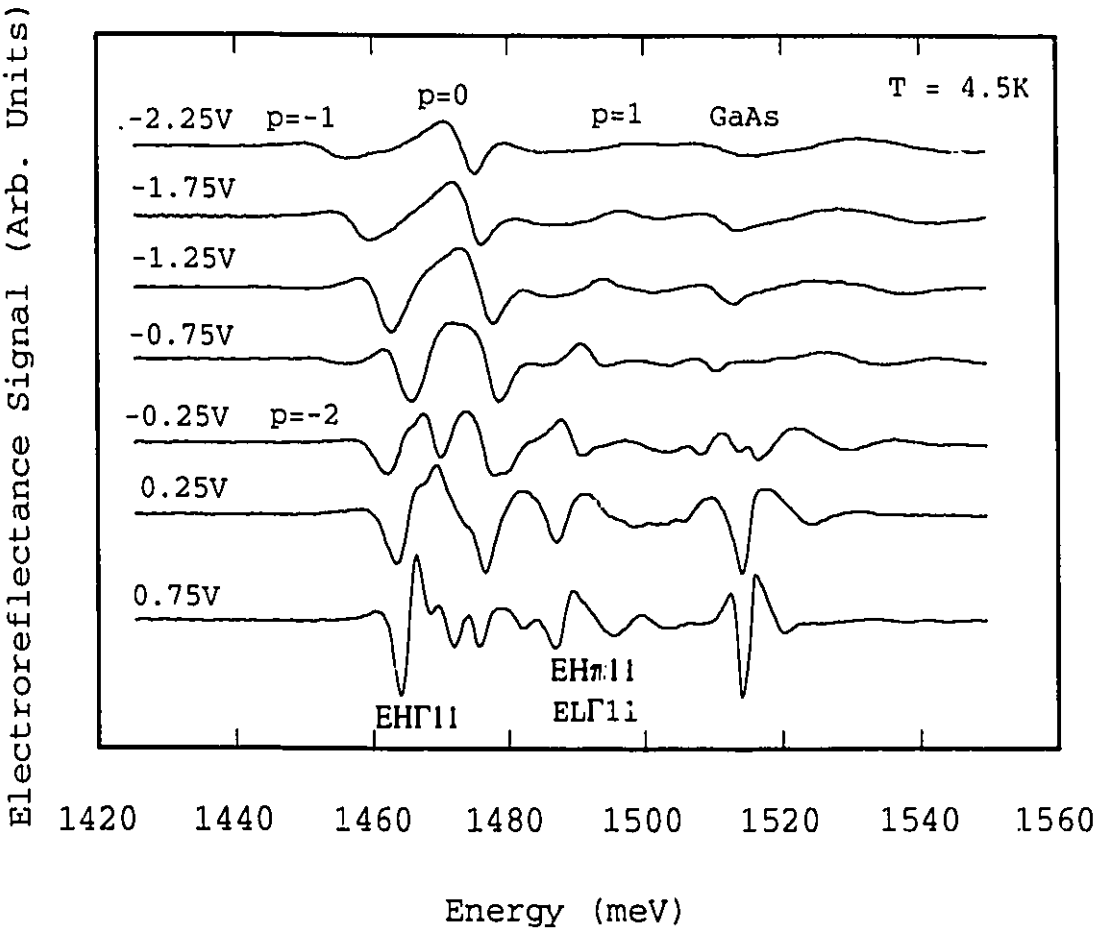

Figure 30. Bias dependence of ER spectra for H145.

4-3-3 PC and ER field dependent spectra for L073

L073 has the greatest interwell coupling of the three superlattice samples studied and is expected to have the most visible Stark ladder peaks. The photocurrent spectra as a function of the applied bias is shown in figure 31. The near flatband spectrum taken at 0.7V bias reveals the exciton transitions between the confined electron to heavy-hole and electron to light-hole levels EHΓ11 and ELΓ11. The EHΓ11 peak broadens then splits into distinct structures as the bias is reduced to 0.5V and 0.3V. These structures are identified as the p=-2, and -1 Stark ladders as the bias is made more negative. The p=0 Stark ladder is observed as a weak peak at 1482 meV in the 0.5V spectrum ($F=4kVcm^{-1}$), then undergoes a blue shift of 2 meV as the bias is reduced to 0.1V ($F=10kVcm^{-1}$) and becomes more intense. At bias voltages more negative than this the p=0 Stark ladder shifts towards lower energies by about 6 meV with the peak broadening. The ELΓ11 excitonic transition at 1490 meV is seen to shift to higher energies with increasing field and is assigned as the p=1 Stark ladder. A very weak shoulder on the p=1 Stark ladder is identified as the p=2 Stark ladder. Unlike the two previous samples, L121 and H145, L073 does not have the structure A, on the high energy side of the p=0 Stark ladder.

The electroreflectance data for bias voltages ranging from 0.7V to -0.7V are plotted in figure 32. The low field spectra taken at 0.7 and 0.5V reveal quite complicated structures. Two factors contribute to this complexity. The first is due to the degree of interwell coupling which is dependent upon the applied field. Strong interwell coupling exists in this sample at zero applied field, permitting the

electrons to move in a translationally invariant environment, yielding a third derivative like ER spectrum. The second source is due to the number of observed transitions, which for weak fields involve Stark ladder transitions to all 10 wells in the superlattice yielding up to 10 visible ER features. However, these same features can not be readily identified without extensive curve fitting.

The high field ER spectra shows less complex features. The extended superlattice states have decoupled at these high applied fields yielding the ladder like progression in energy for the isolated quantum wells. Under these conditions the translational symmetry is lost, resulting in a first derivative like ER spectrum for each transition. The onset of the first derivative like behaviour is observed for L073 (figure 32) to occur at bias voltages negative of 0.3V where the p=-2, -1, and 1 Stark ladders are seen to split away from the p=0 Stark Ladder transition. The p=0 Stark ladder itself only becomes a distinct feature at bias voltages negative of -0.3V (F= 15 $kVcm^{-1}$).

This is in contrast to H145 where the p=0 Stark ladder becomes distinct at - 0.75V (8 $kVcm^{-1}$), and for L121 where this occurrs near 0.25V (6 $kVcm^{-1}$). These two samples have smaller miniband-widths, so that their superlattice behaviour is expected to be quenched at lower fields.

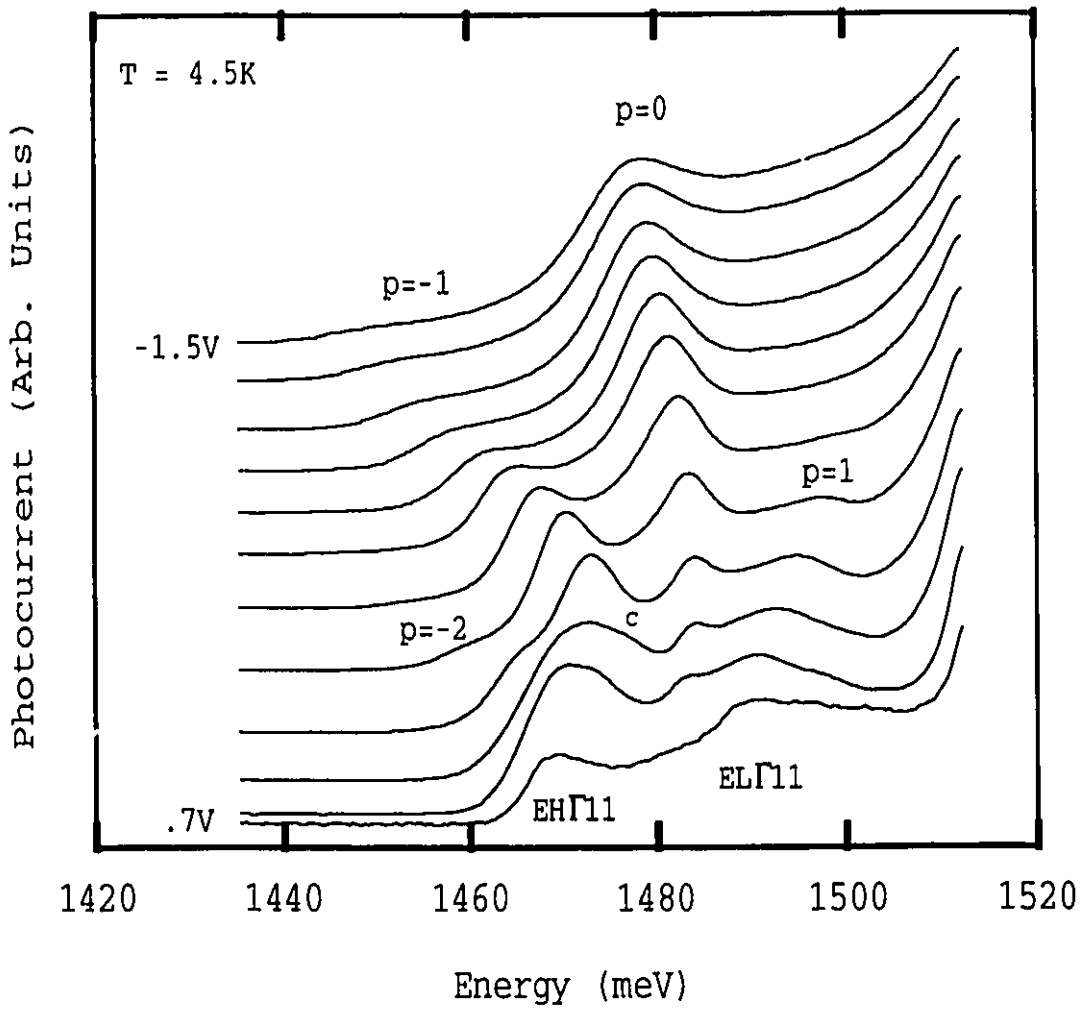

Figure 31. Photocurrent spectra for L073. Bias increment is 0.2V.

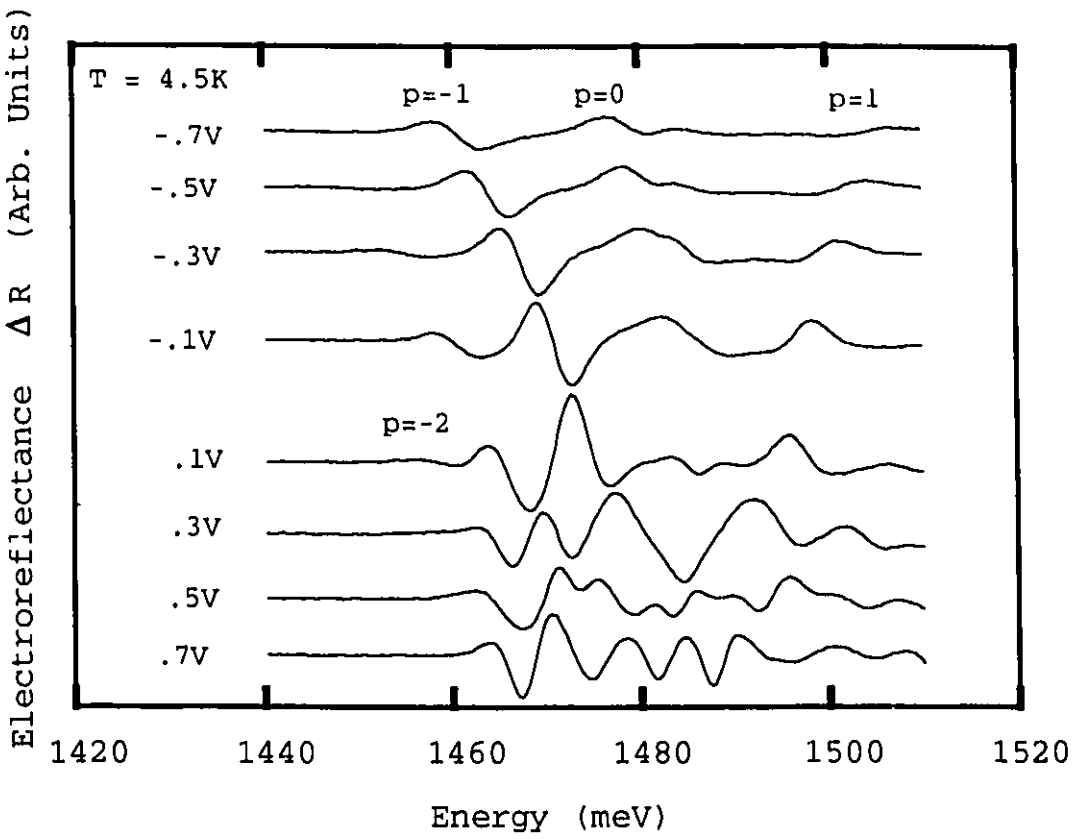

Figure 32. Bias dependent electroreflectance spectra for L073.

4-4 Calculated Stark ladder intensities

The intensities of the Stark ladders in the observed PC spectra are related to the overlap of the electron and hole wavefunctions. The weak-field electron wavefunction extends over several superlattice periods providing an overlap to more than one heavy-hole state, yielding both the p=0 and p≠0 Stark ladders. The application of the electric field rapidly localizes the electrons reducing the overlap to the adjacent

heavy-hole states, hence reducing the p≠0 Stark ladder intensities. The Stark ladder oscillator strengths are determined in part by the degree of interwell coupling for the electrons at zero field. L121 has the lowest interwell coupling, while L073 has the greatest interwell coupling, so that L121 should have weak p≠0 Stark ladders and L073 strong p≠0 ladder intensities. This is supported by the measured photocurrent spectra where only the p=0 and p=-1 Stark ladders are visible for L121 (fig. 27). H145 reveals the p=-2 through p=+1 ladders (fig. 29), and L073 with the greatest interwell coupling exhibits the p=-2 through p=+2 stark ladders (fig. 31).

The field dependence of the Stark ladder intensities are calculated as the overlap between the single particle Stark ladder wavefunctions, Wannier functions, for both the electrons and heavy-holes (equ. 47). This calculation neglects the electron-hole Coulomb interaction so that only a general picture of the absorption spectrum for the superlattice is obtained. The single particle model also treats each Wannier function describing the electron wave function as being identical, and similarly the heavy-hole wave functions. This results in equal oscillator strengths for both plus and minus Stark ladders having the same index. The results of these calculations are presented below in figures 33-35.

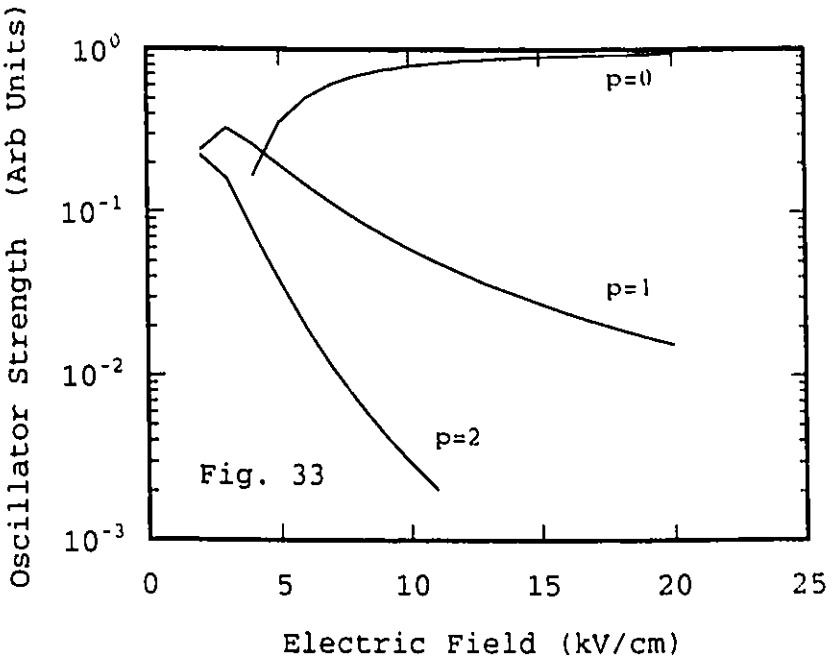
Oscillator Strength (Arb Units)
10^0
10^{-1}
10^{-2}
10^{-3}
p=0
p=1
p=2
0
5
10
15
20
25
Electric Field (kV/cm)

Fig. 33

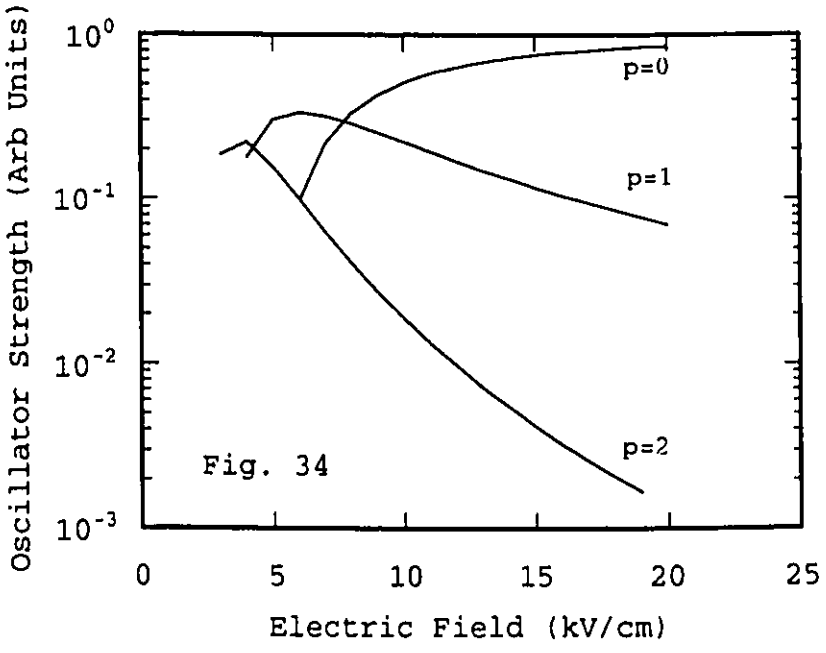
Oscillator Strength (Arb Units)
10^0
10^{-1}
10^{-2}
10^{-3}
p=0
p=1
p=2
0
5
10
15
20
25
Electric Field (kV/cm)

Fig. 34

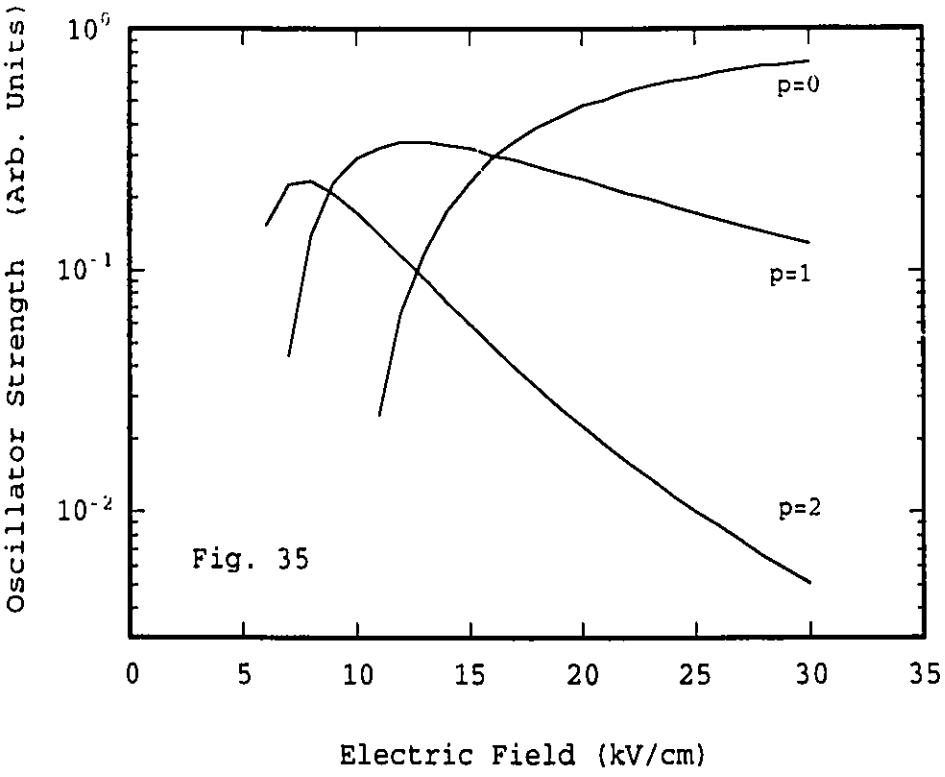

Figures 33-35 Calculated oscillator strengths for the p=0, 1 and 2 Stark ladders. Top previous page (fig. 33) L121, bottom of previous page(fig. 34) H145, above (fig. 35) L073.

The calculated field dependent oscillator strengths for the three samples show similar features. The p=0 Wannier Stark ladder transition oscillator strength, for all three, gains in strength as the electric field is increased from zero, then plateaus to a constant value near F=15 $kVcm^{-1}$. This is consistent with the extended superlattice states coalescing into single quantum well like states with the application of a field. The p=±1 ladders initially increase in oscillator

strength and then decay as the field is increased. The rate of this decrease is dependent upon the samples miniband-width, with the oscillator strength for the narrow miniband-width sample L121 decaying quite rapidly, the p=±1 ladder for L073 decaying slowly in comparison. The p=±2 ladders have a more pronounced dependence on the electric field.

This behaviour can be obtained from the asymptotic expansions of the Bessel functions used to calculate the oscillator strengths. The high field expansion of equation (47) for the p=0 Stark ladder tends to unity, while the asymptotic expansion for the p=1 Stark ladder $J_1^2(-2|\lambda|/qFd) \approx (\lambda/qFd)^2$ and for the p=2 Stark ladder the expansion is $J_2^2(-2|\lambda|/qFd) \approx (\lambda/qFd)^4$. This shows that the p=2 Stark ladders must decay more rapidly than the p=1 ladders with applied field. This expansion also shows that the large miniband width superlattices have less field dependence than the narrow miniband with superlattices, where $|\lambda|$ is one fourth the zero field miniband width. These calculations suggest that for applied fields less than 20 $kVcm^{-1}$ the p=1 and 2 Wannier Stark ladders should be visible in photocurrent measurements for both H145 and L073, but not for sample L121. The p=0 Stark ladder should be visible for all three samples.

Our calculated oscillator strengths show a similar field dependence as obtained by Dignam and Sipe [36]. However, they obtain stronger oscillator strengths for the minus ladders than the plus ladders, which is attributed to the Coulomb interaction which they have included in their calculations.

The photocurrent spectra for the three samples, plotted in figures 27, 29, and 31 confirm our calculations for the relative Stark ladder oscillator strengths. However, the measured PC spectra show the minus Stark ladders as having considerably greater oscillator strength than the plus ladders, in agreement with the calculations of Dignam and Sipe.

4-5 Description of the measured Field Dependent Stark Ladder Energies

The measured exciton transition energies, from their PC spectra, for the three superlattices as a function of the applied field are shown in figures 36 through 38 (symbols). The calculated interband transition energies are also plotted as solid lines. The procedure used to obtain the calculated curves is discussed in section 4-10. The electric field applied to the samples is calculated as the difference between the flatband voltage (0.8V) minus the applied bias, divided by the depletion layer width of the sample. This depletion layer thickness is given by the sum of the cap layer, the 10 period superlattice, and buffer layers and is 1.0 μm for L121, 1.9 μm for H145 and 720 nm for L073.

The three samples show similar Stark ladder behaviour at applied fields greater than 10 $kVcm^{-1}$. In this field range the Stark ladders are seen to split away from the isolated quantum well exciton transition energies for each of the three samples. The minus Stark ladders have slightly steeper slopes and the plus ladders have shallower slopes than given by the tight-binding model. The Stark ladder states are

assumed to be single quantum well like at these applied fields, with the ladder energies being given by the product of the ladder index and the superlattice period, which for the electron to heavy-hole transitions is pqFd, and for the electron to light-hole transitions is (p+1/2)qFd. The measured Stark ladders for H145 and L073 do not extrapolate back to a common origin at zero field as is expected from the tight-binding model. This is due to the Coulomb interaction between the electron and heavy-holes, where each Stark ladder has a different exciton binding energy. The p=0 and p=-1 Stark ladders for L121 appear to converge to a common origin, indicating that both Stark ladders have the same exciton binding energy.

The measured weak field ($F<5kVcm^{-1}$) Stark ladder spectra for the minus ladders seem to converge towards the miniband π points for the three samples, while the p=1 ladder for H145 converges towards the heavy-hole miniband-zone edge ($EH\Gamma 11$). This convergence of the Stark ladders to the miniband critical points, Γ and π, is expected since at zero field the Stark ladder system is fully described by the Krönig-Penney model in the limit of an infinite superlattice. The plus ladders for L073, in contrast, tend to an energy far less than the heavy-hole miniband zone-edge ($EH\pi 11$) and appear to converge towards the $EL\Gamma 11$ miniband zone-centre for the light-hole transition. These two Stark (p=1 and 2) ladders may be a mix of light-hole and heavy-hole transitions, though their slopes suggest a heavy-hole like Stark ladder.

The two samples H145 and L073 have weak structures labelled 'C' lying between the p=-2 and p=-1 stark ladders at fields

less than 10 $kVcm^{-1}$. These structures seem to bridge from the p=-2 ladders at the weakest fields and merge into the p=-1 ladders at fields near 6 $kVcm^{-1}$. It is difficult to assign the Stark ladder indices in this field range since their oscillator strengths are nearly the same. The designation for the p=-1 and the peak 'C' could easily be reversed.

The sample L121 also has a distinct quantum well like peak labelled A' nearly 16 meV higher than its p=0 Stark ladder. H145 also displays a weak shoulder nearly 5 meV higher than its p=0 ladder. In both cases these peaks seem to follow the field dependence of the p=0 Stark ladders. Neither the structures labelled A and C are expected from the tight-binding model or the single particle numerical calculations. This suggests that these models provide an incomplete description of the Wannier Stark ladders.

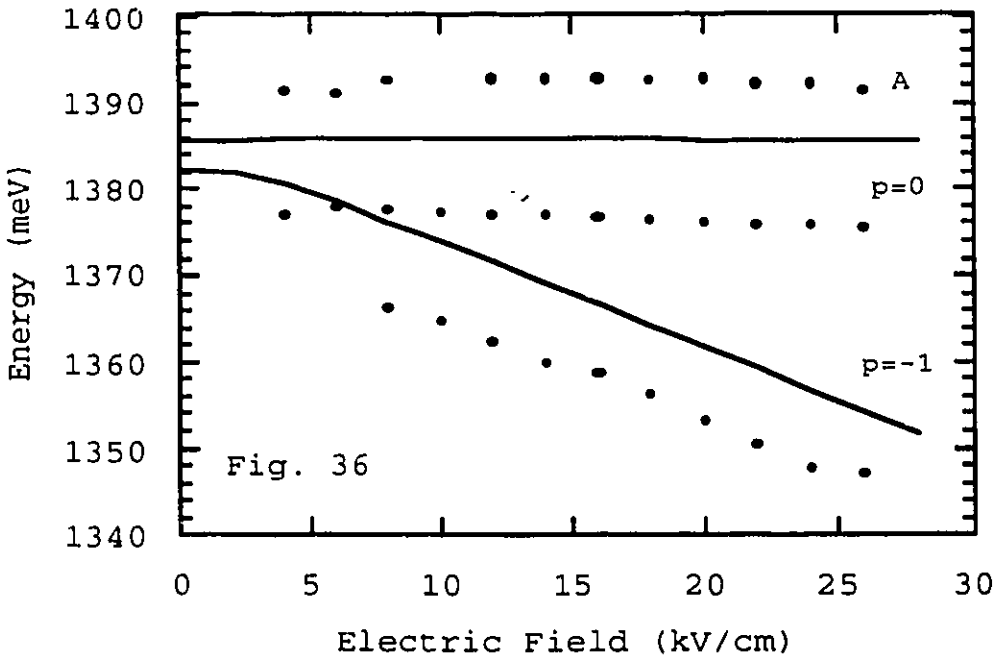

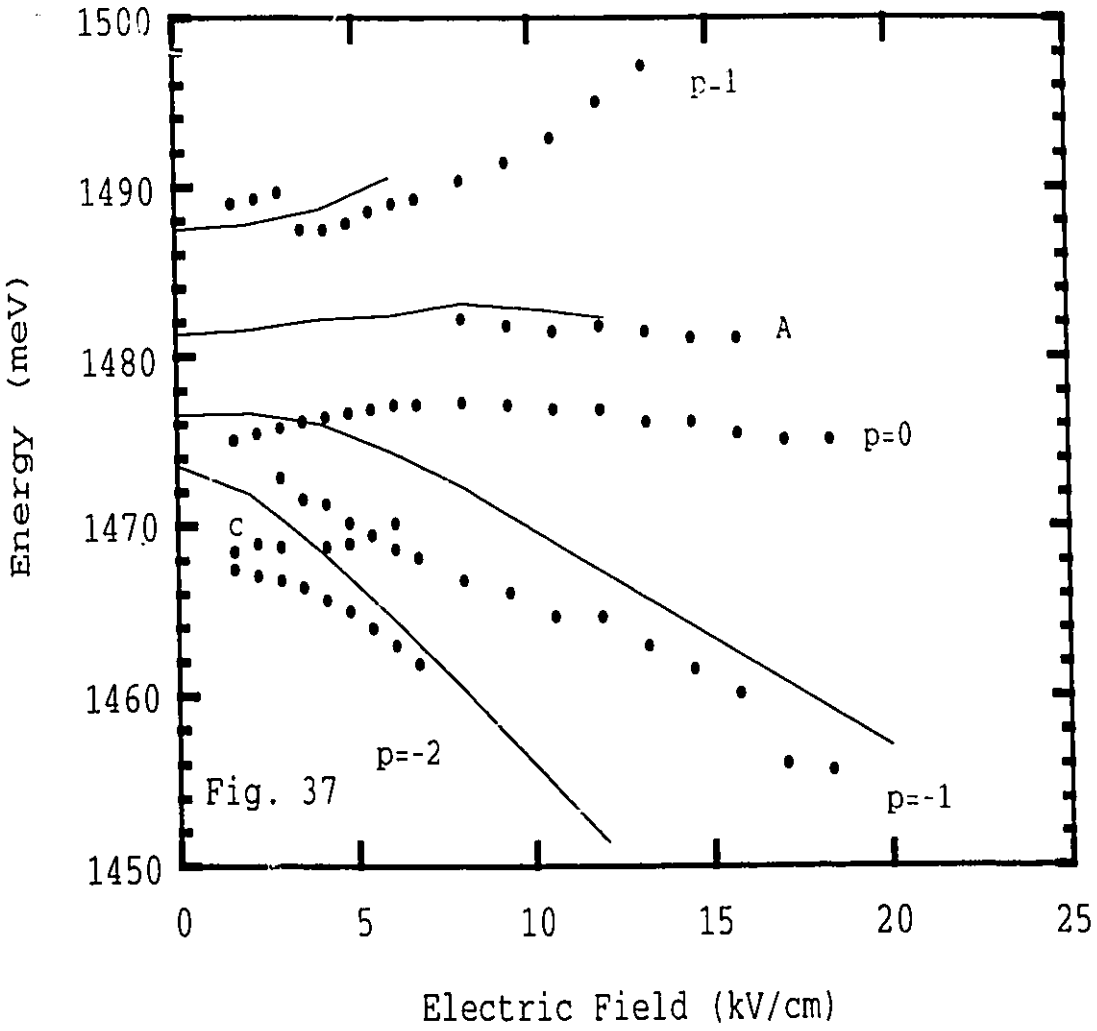

Figures 36 and 37. Calculated interband transition energies (solid curves), and measured exciton transition energies for L121 in figure 36 previous page, and H145 figure 37 above.

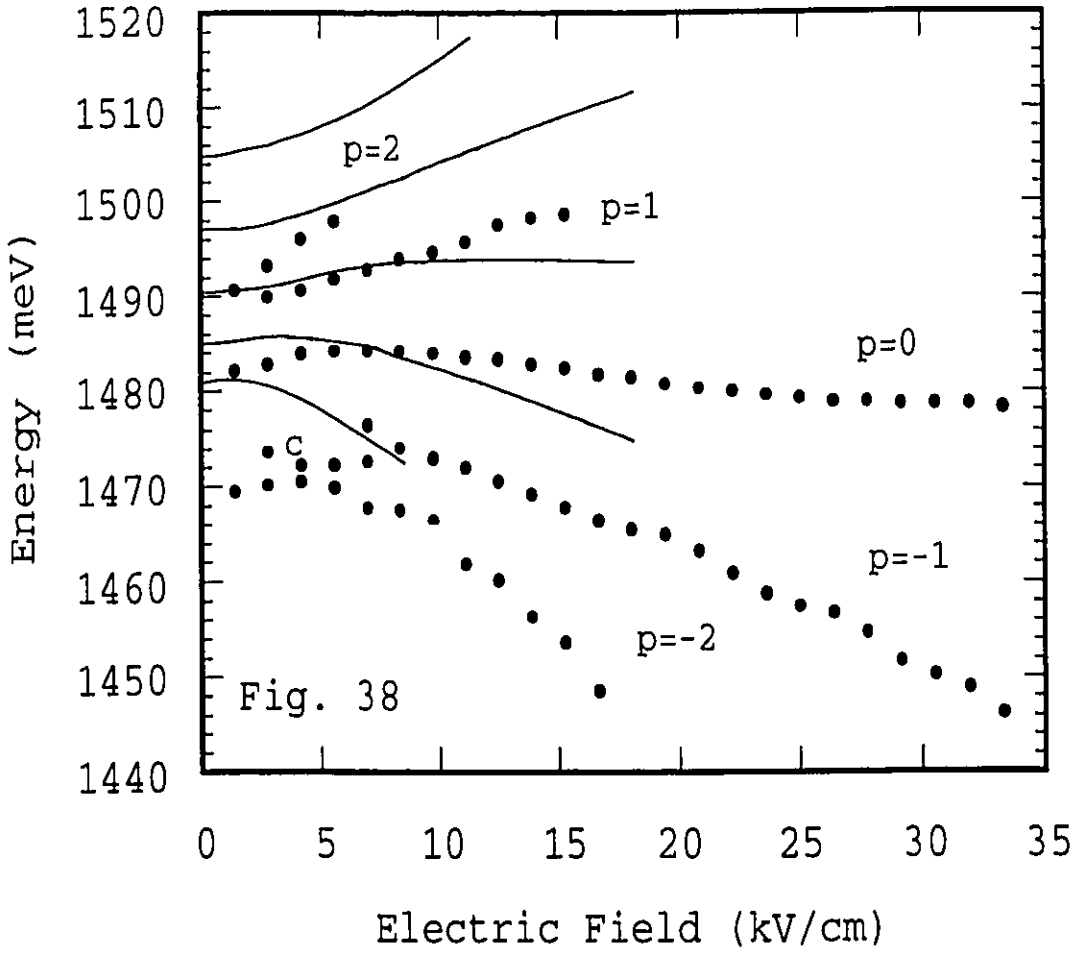

Figure 38 . Measured Stark ladder exciton transition energies (symbols) and calculated Stark interband transition energies (solid lines) for L073.

4-6 Calculated Stark ladder structures - single particle model

The Stark ladder interband transition energies for the superlattices L121, H145, and L073 are calculated as the sum of the electron Stark ladder, the strained $In_xGa_{1-x}As$ layer energy gap, and the heavy-hole quantum well eigenstate

energy. The Coulomb interaction is not included in these calculations. This method of breaking the system into separable electron, and heavy-hole terms, and neglecting the Coulomb interaction is the single particle model. In this particular calculation the heavy-holes states are assumed to be strongly localized (ie. single quantum well like) with their eigenstate energies for the first level, H1, being given by the transcendental function (equ. 5). The strained energy gap for the $In_xGa_{1-x}As$ layer is obtained using equation (1).

The derivation of the tight-binding model, Chapter 1 section 12, assumes large fields where Stark localisation has occurred ie. for $qFd/|\lambda| >> 1$, where $|\lambda|$ is one fourth of the zero-field miniband-width. This implies that the tight-binding model is valid for fields greater than 5 $kVcm^{-1}$ for the electron Stark ladder. This criteria also indicates that the heavy-hole states may be treated as single quantum well like for all fields. The Stark ladder energies are calculated for the electron levels using either the transfer matrix method discussed in Chapter 1 section 4 (L121 and H145), or by numerical integration method described in Chapter 1 section 8 (L073).

4-6-1 Electron Stark ladders

The electron and heavy-hole Wannier Stark ladders for the small electron miniband-width superlattice, L121, are calculated using both the transfer matrix method (Tmat) and Bleuse's tight-binding model [33]. The measured photocurrent and electroreflectance spectra for L121 indicates interwell

coupling extending over 3 wells, as opposed to the 10 wells making up the sample. Hence, both 5 and 11 well electron superlattice calculations are used to simulate the measured Stark ladder energies. The well and barrier regions being divided up into 20 segments each. The zero field eigenenergies obtained from the transfer matrix method for the 5 well superlattice (figure 39 solid curves) are distributed in energy between superlattice Γ and π points. The energies of the end ladders (p=-2 and 2) converge to the Γ and π points as the number of wells increases in the calculation as is expected (fig. 40 solid curves). The spacing between the eigenstate energies also decreases as demonstrated by the plot for the 11 well electron superlattice. The application of an electric field in the direction of the superlattice causes the eigenstate energies to split away from their zero field values, with the slopes asymptotically approaching the tight binding model as the field increases (figures 39 and 40 dashed curves).

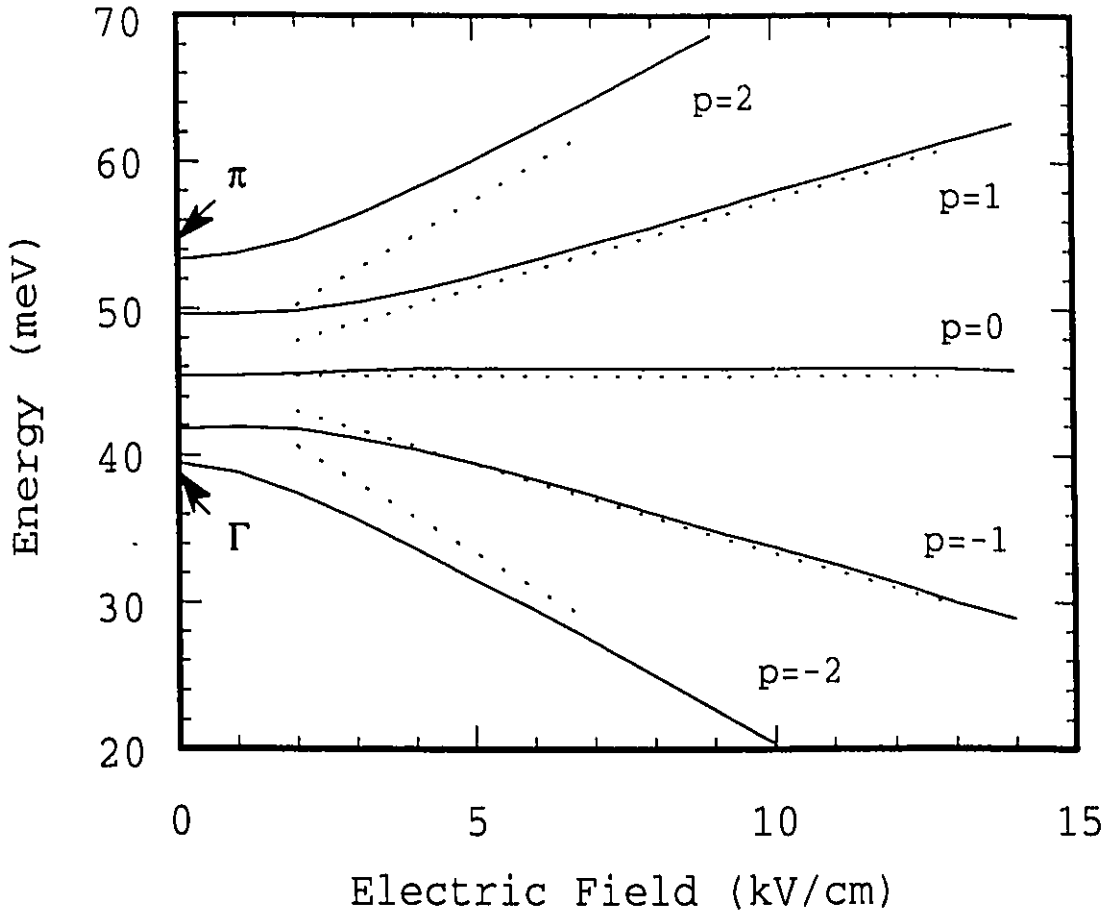

Figure 39. Calculated Wannier Stark ladder for electron levels in a five period superlattice. Transfer matrix calculations are plotted as solid lines, while tight-binding results are given by dashed lines. The bottom of the well is taken to be at 0 meV.

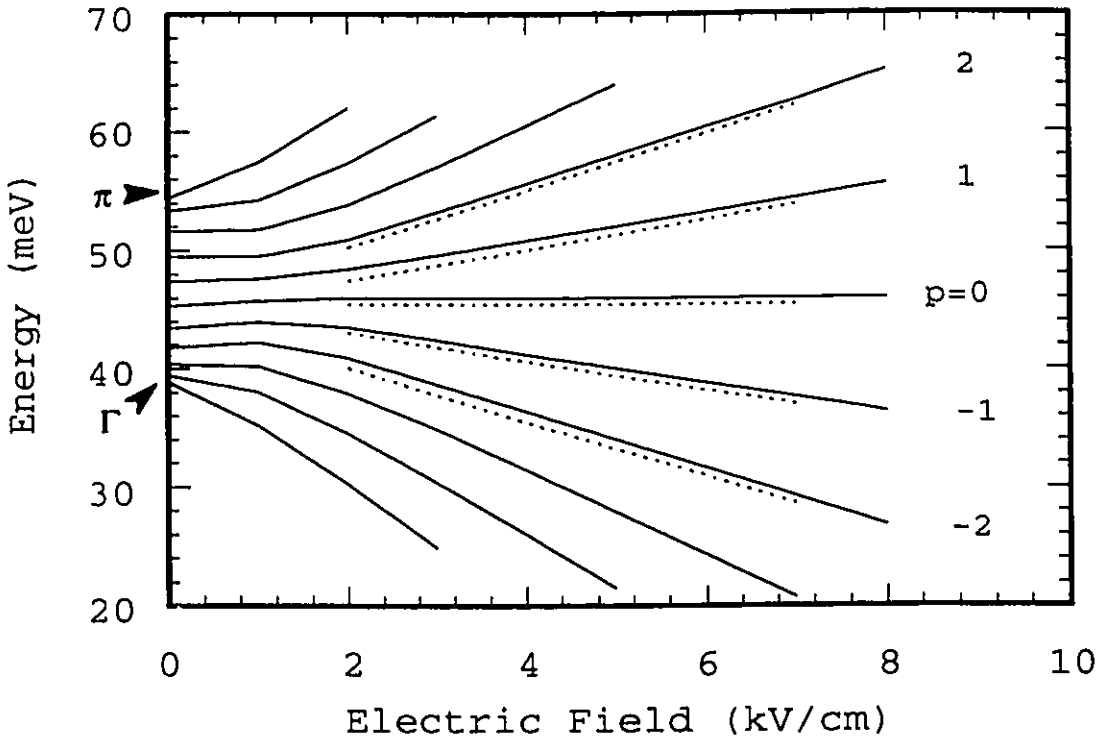

Figure 40. Calculated electron Stark ladders for the 11 well structure.

4-6-2 Heavy-hole ladders

The zero-field, heavy-hole miniband-width for L121 is 0.65 meV implying that both the tight-binding and transfer matrix calculations are valid for fields as low as 0.2 $kVcm^{-1}$. Both methods yield Stark ladder slopes being given by qpFd. A plot of the Wannier Stark ladders for the 5 well heavy-hole superlattice using the Tmat calculation in figure 41 reveals this narrow miniband-width at zero field, as well as the Stark ladder formation for fields less than 1 $kVcm^{-1}$. The formation of heavy-hole Wannier Stark ladders in figure

41 at very weak fields indicates the rapid onset of heavy-hole localization. This permits, as argued in Chap 1, that the heavy-holes can be treated as single quantum well like states for all applied fields, whereas the electron states which localize at fields approaching 5 kVcm^{-1} can be treated as single quantum well like only at large fields. The electron to heavy-hole transitions should reflect the more complex electron eigenstate energies at weak fields, before coalescing into the Wannier Stark ladders at the higher applied fields.

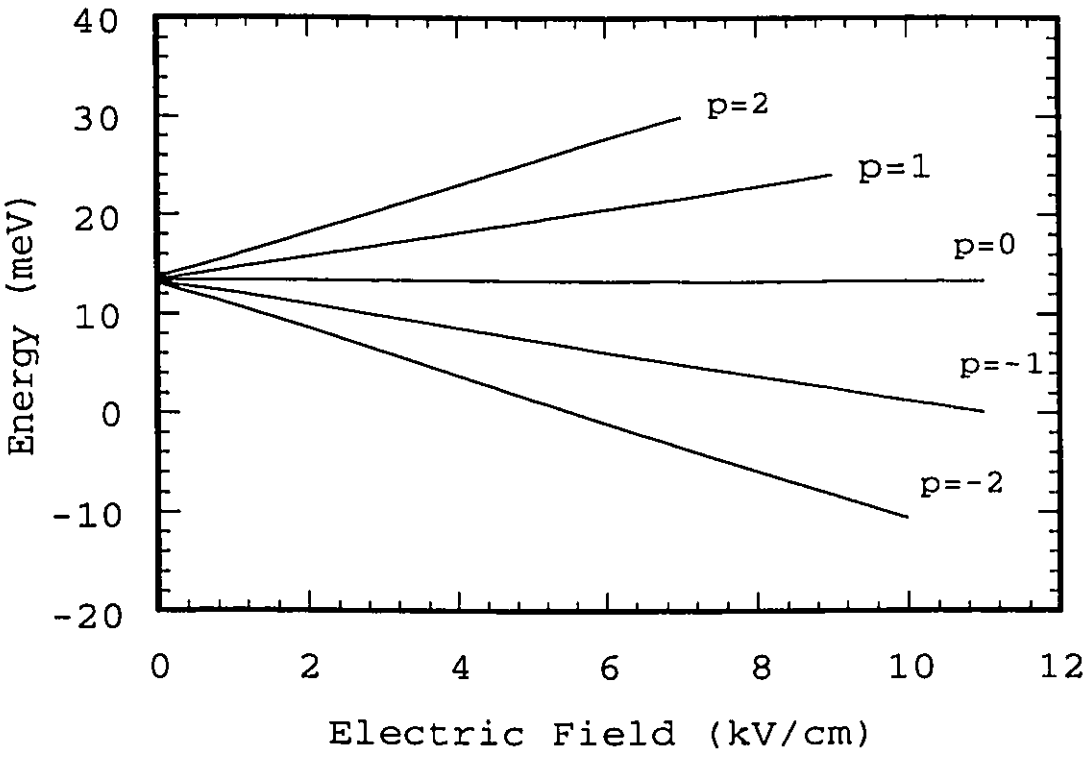

Figure 41. Calculated heavy-hole Wannier Stark ladders for 5 well structure using the transfer matrix method. The bottom of the well is at 0 meV.

The calculated Stark ladders using the transfer matrix method for the electrons and heavy-holes show the same behaviour as obtained by McIlroy [23] who used the matrix method but with the Hamiltonian being transformed to yield Airy function solutions (equ. 20). Our results are also similar to those of Hagon and Jaros [73] who have used a pseudopotential calculation. The weak field behaviour of the electron Stark ladders (figures 39 and 40 solid curves) indicates a repulsion of the electron levels away from the single quantum well energy as obtained from the tight-binding model. It should be noted that both Dignam and Sipe [35,47] and Whittaker [74] have shown that the single particle calculations are invalid at weak fields due to the Coulomb interaction between carriers in the various Stark ladder levels.

4-7 Comparison between calculated interband and measured exciton transition energies.

The calculated interband transition energies for L121, plotted in figure 36, show good agreement with the measured excitonic transition energies for applied fields in the range of 5 to 25 $kVcm^{-1}$. The calculated p=0 ladder is 9 meV higher than the measured p=0 exciton transition energy for applied fields greater than 5 $kVcm^{-1}$. This difference in energy is close to the calculated exciton binding energy of 8.5 meV for the 6 nm wide quantum well as plotted in figure 16. The energy difference between the calculated and measured p=-1 Stark ladders is 8 meV, greater than expected for the oblique exciton of 4 meV. The binding energy of the 'oblique exciton is discussed in section 4-8.

Sample H145 shows a similar agreement between the calculated interband and measured exciton transition energies for the Stark ladders (figure 37). The energy difference between the calculated and measured p=0 Stark ladders is nearly 6 meV, slightly lower than the calculated exciton binding energy for the 2.5 nm wide quantum well of 8 meV. The energy difference for the p=-1 Stark ladder is 4 meV the same as the calculated value. The energy difference for the p=1 and -2 Stark ladders is about 2 meV, though the calculated p=1, and the measured p=-2 Stark ladders do not extend sufficiently high in electric field to permit an accurate comparison between the calculated and measured exciton binding energies. Neither of the two structures labelled A and c are obtained from our calculations.

The conduction band potential wells for L073 were too shallow to be treated using the transfer matrix method. Hence this sample was modelled using the numerical integration method for a 7 well structure. There appears to be reasonable agreement between the calculated and measured Stark ladders for the p=0, -1, and -2 ladders, but not for the positive Stark ladders. Whereas the calculated p=2 Stark ladder tends towards the superlattice EHπ11 point at 1505 meV for zero electric field, the measured p=1 and 2 Stark ladders converge to the light-hole excitonic transition energy ELΓ11 at 1490 meV. The exciton binding energy for the p=0 Stark ladder is measured as 11 meV, higher than the expected 8.5 meV. Similarly the p=-1 oblique exciton binding energy appears to be too large at 10 meV.

4-8 Calculation of the oblique exciton binding energy

The 'oblique' exciton refers to the Coulomb interaction between electrons and holes confined in adjacent wells. Hence, each of the Stark ladder exciton transitions has an associated Coulomb interaction. It is possible, within the context of the single band or effective mass model, to calculate the binding energies for each of the Stark ladders. This is most easily done for large fields where the electron and heavy-hole levels have coalesced into single quantum well like states. The calculated electron Stark ladder plotted in figure 39 suggests that the electron localization occurs near 5 $kVcm^{-1}$ for L121.

The model of Soucail et al. [48] is used to calculate the oblique exciton binding energies as a function of superlattice period. In this model the superlattice period determines the binding energy, as opposed to the relative widths of the well and barrier regions. The zero field single quantum well like functions (equ. 56) are used for both the electron and heavy-hole states with the heavy-hole quantum wells being translated from the electron well by one period of the superlattice. The weak field ($F<20$ $kVcm^{-1}$) perturbation to these zero field states reduces the calculated binding energies by less than 0.2 meV. The p=1 exciton binding energy remains nearly constant for fields ranging from 5 to 15 $kVcm^{-1}$ [49], while the p=-1 oblique exciton energy is reduced by less than 1 meV. Our calculated oblique exciton binding energy of 4.4 meV for a 9 nm superlattice period is in excellent agreement to that of Dignam and Sipe, who calculate a value of 4.4 meV for a 9 nm period $Al_xGa_{1-x}As$-GaAs superlattice. The calculated binding

energies for the p=±1 ladders are plotted below in figure 42. The p=0 exciton binding energy is obtained by setting the superlattice period to zero and solving for the isolated quantum well exciton binding energy, with results similar to that plotted in figure 16.

These calculated binding energies are only valid in the limit of high electric fields where the superlattice states have localized into single quantum well like states. The low field superlattice exciton binding energies can not be obtained using these functions.

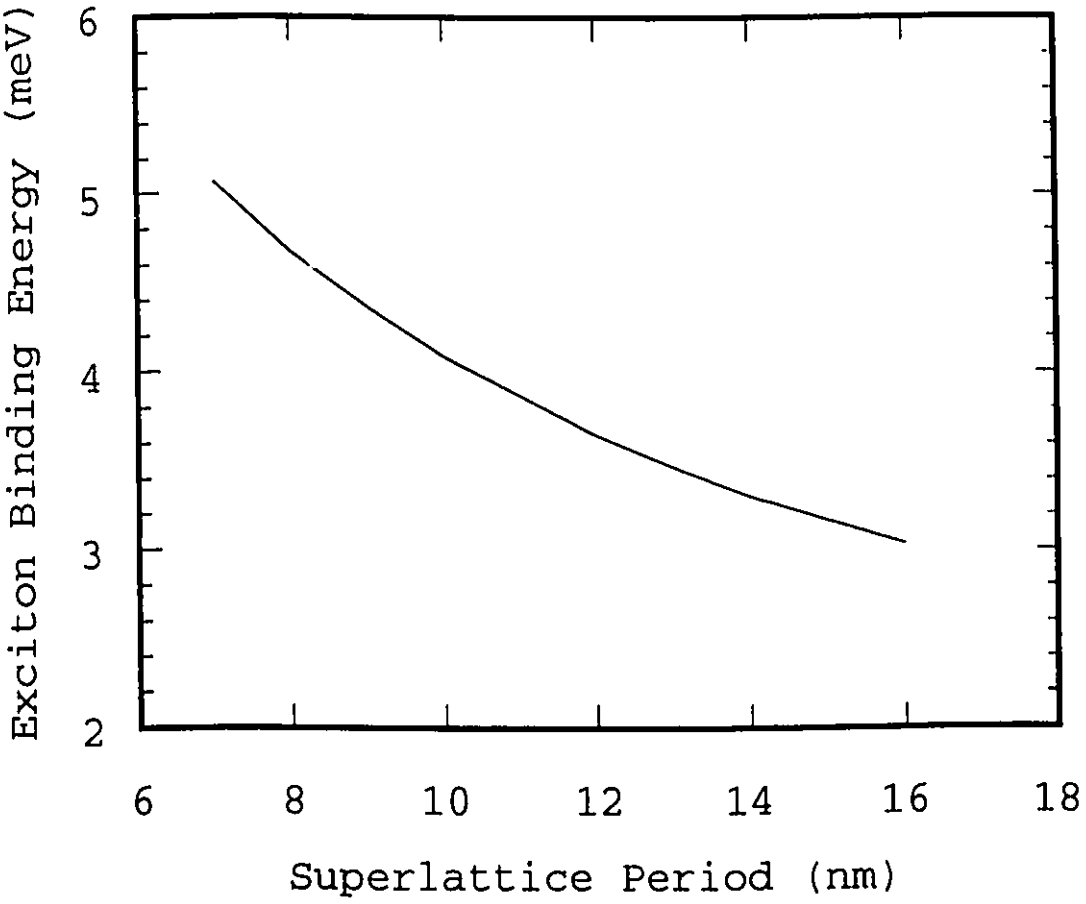

Figure 42. Calculated 'oblique' exciton binding energy versus superlattice period.

4-9 Summary

A systematic study has been made of the Stark ladder formation and Stark localisation for a series of three superlattices. These superlattices have similar superlattice periods but with increasing indium content in the $In_xGa_{1-x}As$ well layer. The increased In content results in progressively deeper quantum wells, and reduced interwell coupling for both electron and heavy-holes. The application of an electric field in the growth direction decouples the wells making up the superlattice giving rise to the Wannier Stark ladders. The observed photocurrent spectroscopy data for L121, having a high 17% In content in the wells, has two visible Stark ladders . H145 with a 13% In well content reveals four Stark ladders, and L073 with the lowest indium content of 6.5% shows five Stark ladders. The slopes of the Stark ladders at fields greater than $10kVcm^{-1}$ agree well with the tight-binding results.

Bleuse's [33] tight-binding model is used to calculate the field dependence of the Stark ladders, the oscillator strengths for the Stark ladder transitions, as well as the binding energies associated with the p=0 and p=1 Stark ladders. A numerical calculation of the Stark ladder energies is also performed. The results of these calculations are found to be in good agreement with the observed Stark ladder data.

Five features are observed in the photocurrent spectroscopy data which are not adequately explained by the tight-binding model or our single particle numerical calculations; these are: 1) The observed asymmetry in the oscillator strengths

for the plus and minus ladders is not calculated. 2) The low field behaviour of the Stark ladders deviates strongly from the calculated eigenenergies. 3) The high field Stark ladder slopes do not extrapolate to a common energy at zero applied field. 4) The structures labelled 'c' in the low field spectra for H145 and L073 are neither obtained in the single particle calculations, nor identified. 5) The peaks A observed on the high energy side of the p=0 Stark ladders are not calculated or identified.

The first four features are explained by Dignam and Sipe [35-36] using a tight-binding model which includes the Coulomb term. The last feature 5) is not obtained in their calculations. The origin of these five features is discussed in the next chapter.

Chapter 5

5-1 Exciton Stark ladders

The single particle calculations that have been performed in this thesis yield good agreement for the three samples, L073, L121 and H145 at large fields where the Stark localization has occurred. However at weak fields the single particle model breaks down, failing to predict the weak field Stark ladder structures including the anticrossings of the negative Stark ladders. The origin of these anticrossings is due to the Coulomb interaction, where each Stark ladder transition has, in general, a different exciton binding energy. At weak fields the Stark ladders can have similar energies, resulting in a mixing of states, leading to a transfer of oscillator strengths between adjacent levels. This is most pronounced for the negative index Stark ladders [36].

Dignam and Sipe [35-36] as well as Whittaker [74] have shown that the Coulomb term must be included in the Hamiltonian. Dignam and Sipe refer to their model as a two well exciton calculation. They write the eigenstate functions for the superlattice as a Bloch like function of the form,

$$\Psi_p^{\kappa} = \frac{1}{\sqrt{N}} \sum_{\ell,m} e^{i\kappa md} b_\ell^p \Phi_\ell(\rho, z_e - md, z_h - md). \qquad (63)$$

d is the superlattice period, κ the wavevector, N the normalization constant, b_ℓ^p the expansion coefficients. $\Phi_\ell(\rho, z_e - md, z_h - md)$ is the two well exciton wavefunction localized about the m^{th} well. The function Φ_ℓ consists of a

1-S like exciton wavefunction $\lambda\exp(-\lambda\rho)$, an electron wavefunction $f_1(z_e)$ and the heavy-hole wave function $f_\ell(z_h - \ell d)$ located ℓ superlattice periods away from the electron wavefunction. The two well exciton wave function is written as,

$$\Phi_\ell = \left(\frac{2}{\pi}\right)^{\frac{1}{2}} \lambda e^{-\lambda\rho} f_\ell^e(z_e) f_\ell^h(z_h - \ell d) \tag{64}$$

The electron and heavy-hole functions $f_\ell(z_e)$ and $f_\ell(z_h - \ell d)$ are the field perturbed isolated quantum well wave functions (equ. 61) that are obtained variationally in the same way as we have performed for the field perturbed exciton binding energy in Chapter 1, section 1-15. The wave function Φ_ℓ is then obtained by variationally solving for the exciton term $\lambda\exp(-\lambda\rho)$ as a function of the electron-hole separation ℓ. A tight-binding calculation is then performed over all electron-hole separations (ℓ), and well sites of the superlattice (m).

Dignam and Sipe simplify their calculations by noting that the only states accessible via optical excitation are states with $\kappa=0$. Furthermore only a finite basis set is required, hence they truncate their calculations to electron-hole separations of less than 20 superlattice periods. They have performed these calculations for the two superlattices L121 and H145 which are plotted in figures 43 and 44.

The exciton Stark ladders plotted for sample L121 in figure 43 show a strong p=0 Stark ladder emerging at 1378 meV as the field increases past 10 $kVcm^{-1}$. The relative strength of the Stark ladders is indicated by the size of the symbols used to

indicate the Stark ladder energies. The p=-1 and p=+1 ladders are seen to split away with increasing field, with the minus Stark ladder showing greater oscillator strength. The relative Stark ladder intensities are in good qualitative agreement with our observed data (fig. 27), where the p=0 Stark ladder is quite intense compared to the p=-1 ladder, while the p=1 ladder is too weak to be seen. The calculated p=-1, 0, and 1 Stark ladders converge to nearly the same energy at zero field in good agreement with the plotted data in figure 36. Finally anticrossings, labelled 'c', between the p=-1 and -2 Stark ladders are calculated for fields less than 5 $kVcm^{-1}$. These anticrossings are not observed in the spectra for L121, where their oscillator strengths are too weak to be observable.

The calculated Stark ladders for H145 reveal 5 relatively strong Stark ladders showing similar field dependence and oscillator strengths as our data plotted in figures 29 and 37. In particular the anticrossing of the minus Stark ladders 'c' are calculated and observed in the same energy and electric field range.

There is good qualitative agreement between the calculated and measured Stark ladders, confirming the necessity of including the Coulomb interaction in the Stark ladder calculations. However the two unidentified features A and A' observed in our data for L121 and H145 are not obtained in these calculations involving the 1-S hydrogen like exciton term. A further calculation was performed utilizing the 2-S exciton for the sample H145 resulting in the formation of a weak Stark ladder 3 meV above the p=1 Stark ladder plotted in figure 44, which is not observed in our data.

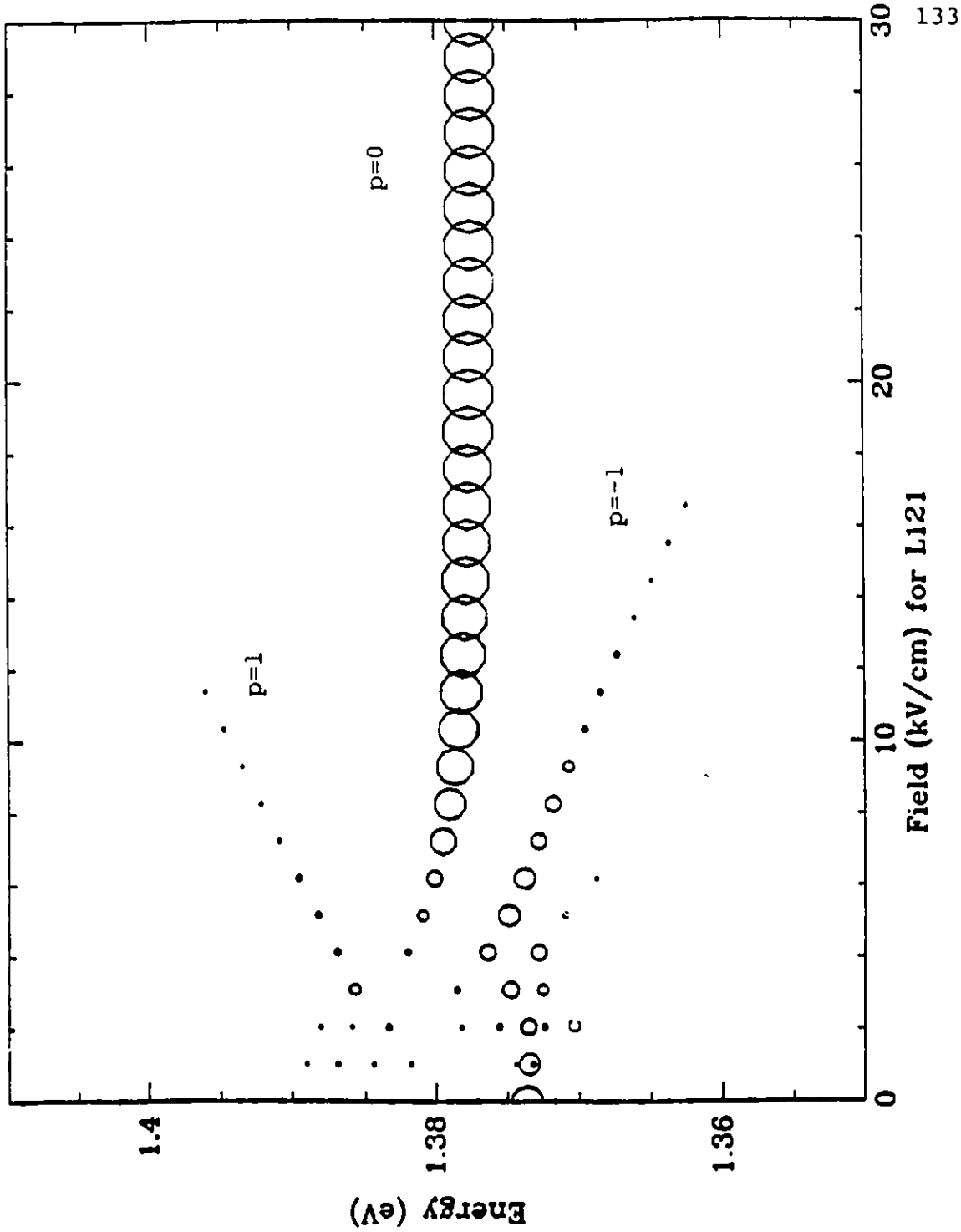

Figure 43. Plot of exciton Stark ladders for L121. Symbol size indicates relative Stark ladder oscillator strength.

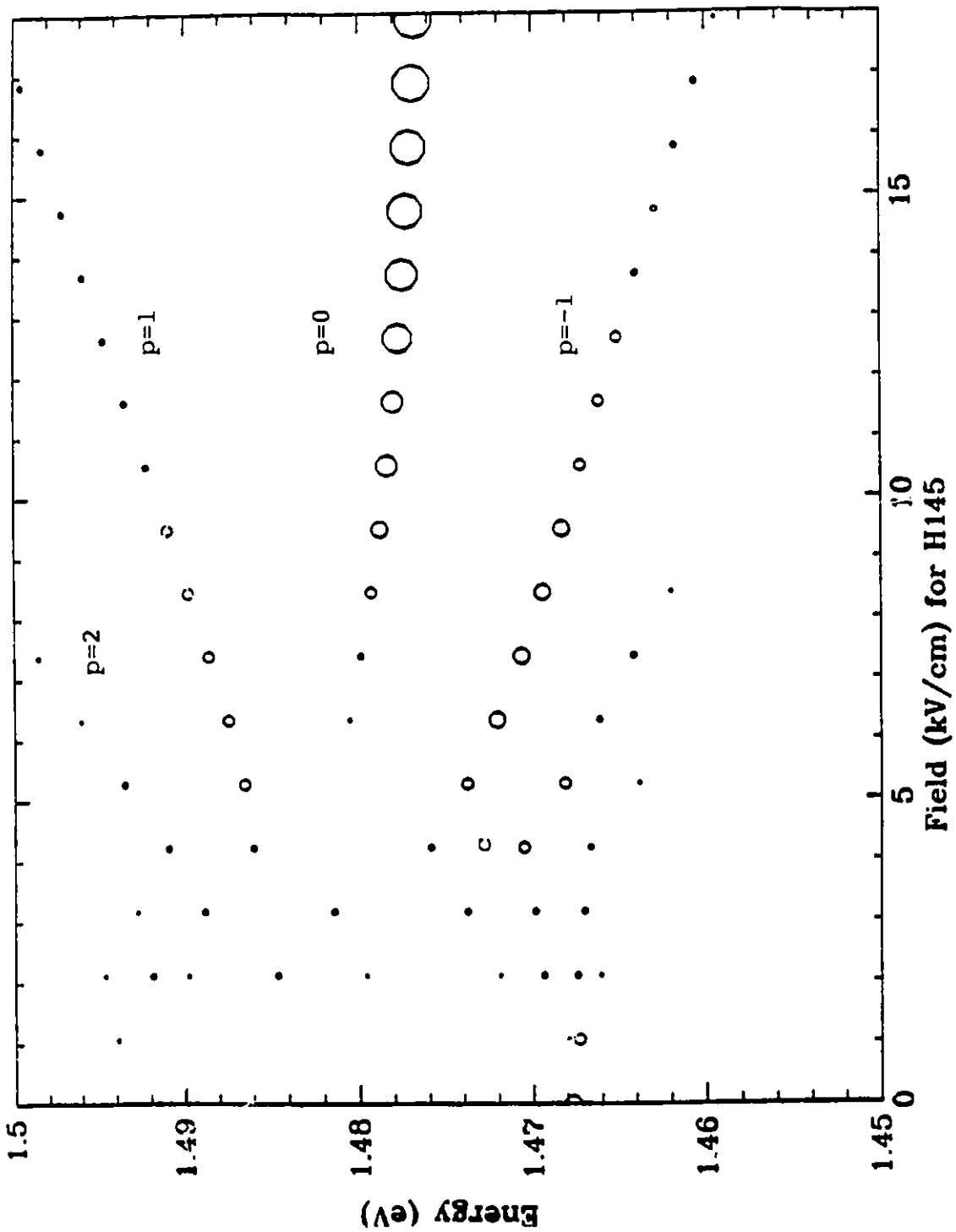

Figure 44. Plot of exciton Stark ladders for H145.

5-2 The peaks A and A'

The structures labelled A and A' observed in the photocurrent and electroreflectance spectra of L121 and H145, figures 27-30, and 36-37, are not accounted for by either our single particle calculations or the exciton Stark ladder calculations of Dignam and Sipe [35]. The origin of these peaks is not understood though it has been observed in both $In_xGa_{1-x}As$-GaAs [11-12,72] and $Al_xGa_{1-x}As$-GaAs [75] superlattices. Saker et al. [72] observed a similar peak in their PC spectra of an $In_xGa_{1-x}As$-GaAs superlattice arguing that it was due to end effects. Here the last well in the superlattice is embedded in a semi-infinite barrier on the one side, and a superlattice barrier on the other. This is in contrast to the remaining wells which are surrounded by the superlattice barrier. Huang [76] has shown that this end effect gives rise to a higher single quantum well interband transition energy for the p=0 Stark ladder in an $Al_xGa_{1-x}As$-GaAs superlattice.

Soucail et al. [11] and Gibb et al. [12] have also observed the structure A in an $In_xGa_{1-x}As$-GaAs sample as a weak shoulder on the high energy side of the p=0 Stark ladder. They suggest that it was due to a quantum well in the superlattice being a monolayer thinner than expected. This can occur if islands of GaAs form at the $In_xGa_{1-x}As$-GaAs interface causing a portion of the $In_xGa_{1-x}As$ wells to be a layer thinner, alternately the whole well can be thinner. A change by one layer of thickness (0.5 nm) for L121 and H145 increases the E1H1 exciton transition by 6 and 10 meV respectively, neither in particularly good agreement with the measured shifts of 16 meV for L121 and 5 meV for H145.

Other suggestions have included the existence of Tamm states at the $Al_xGa_{1-x}As$-GaAs interfaces [75,77], and a transition not involving the exciton such as a transition to the n=0 Stark ladder continuum [72] which can generate the higher energy peaks 'A'.

5-3 End Effects

One of the potential sources for the peak A is an end effect which is common to all of the fabricated samples, where the last well at each end of the superlattice sees a different environment than the others. The end wells are embedded between a thick barrier on the one side and a thin barrier layer on the other. This is in contrast to the remaining wells in the superlattice which are embedded between two barrier layers. Saker et al. [72] argue that this end effect gives rise to a higher single quantum well interband transition energy for the p=0 Stark ladder. The effects of the semi-infinite barrier layer were calculated using the numerical method described in Chapter 1 section 8, for the conduction band potential profile shown below in figure 45. Varying the semi-infinite barrier layer from 5 to 40 nm causes the lowest quantum well eigenstate energy level E1 to vary by less than 2 meV for L121 and H145. This is too small to account for the measured energy differences of 5 and 16 meV for H145 and L121 respectively. The heavy-holes are more tightly confined to the valence band potential wells and are negligibly affected by the width of this semi-infinite barrier.

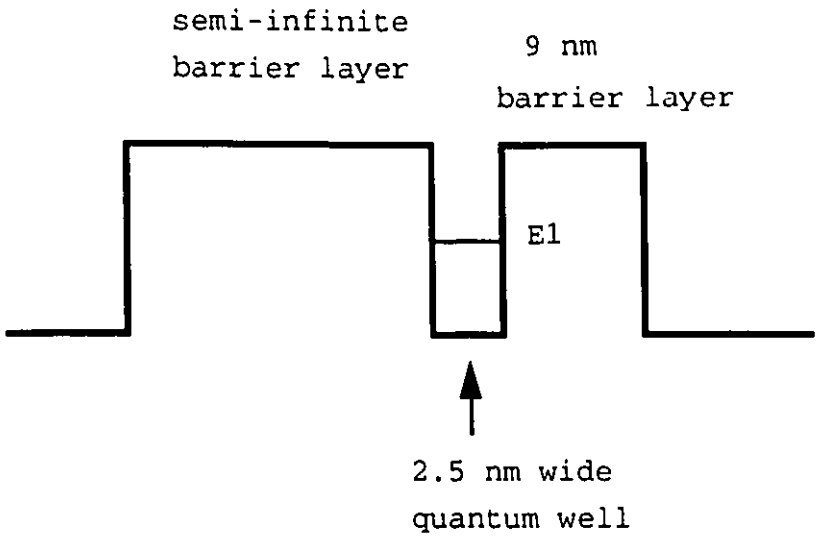

Figure 45. End quantum well potential profile used to calculate effects of thick barrier width. Barrier height is 95.6 meV for H145.

5-4 Surface Effect

A surface effect may also occur when the end well of superlattice is quite close to the surface. H145 for example has only an 18 nm GaAs cap layer between the surface and the first quantum well making up the superlattice. This sample makes use of a 10 to 20 nm thick semi-transparent gold front contact, hence the potential experienced by the electron in this layer is expected to be different than in the GaAs cap layer. Ohno et al.[75] have referred to this surface potential as a Tamm state in their calculations and measurements of an $Al_xGa_{1-x}As$-GaAs superlattice. They have used an AlAs surface potential at one end of their superlattice with no cap barrier layer as we have used in figure 46. This is representative of sample H145

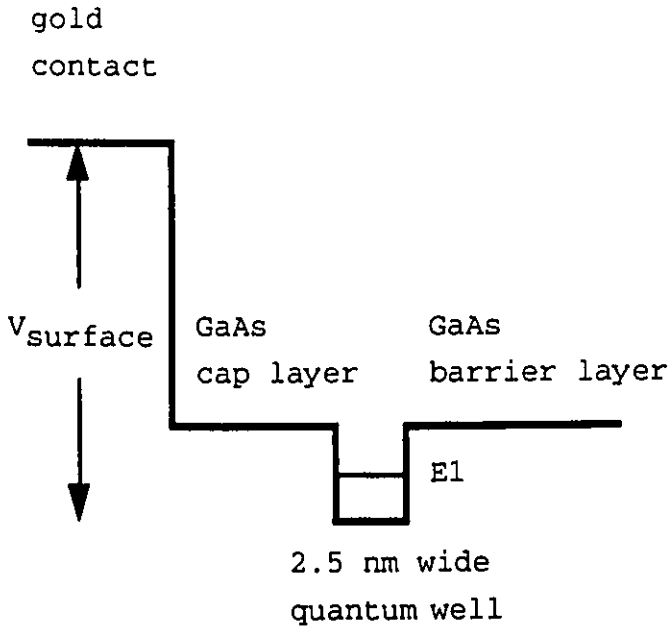

Figure 46. Potential profile used to calculate the effects of a surface potential such as from a gold front contact. Calculations are performed as a function of the surface potential $V_{surface}$ for two GaAs cap layer thicknesses, 9 and 18 nm.

The well and barrier masses used in calculating the curves in figure 47 are .066 and .0665m_0. The free electron mass is used for the surface potential layer. The surface potential of the semi-transparent gold window is varied from 95 to 500 mV with respect to the bottom of the $In_{.128}Ga_{.812}As$ quantum well potential. An energy shift of less than 0.2 meV is calculated for the E1 quantum well level when an 18 nm wide GaAs cap layer is used (fig. 45 curve A) indicating that the wave function is not penetrating into the surface potential layer. Reducing the cap layer to 9 nm increases the

penetration of the wave function into the surface potential raising the calculated energy shift to about 1.5 meV (fig. 47 curve B). Further reduction of the cap layer thickness to 5 nm enhances the effect of the surface potential to about 6 meV (fig. 47 curve c).

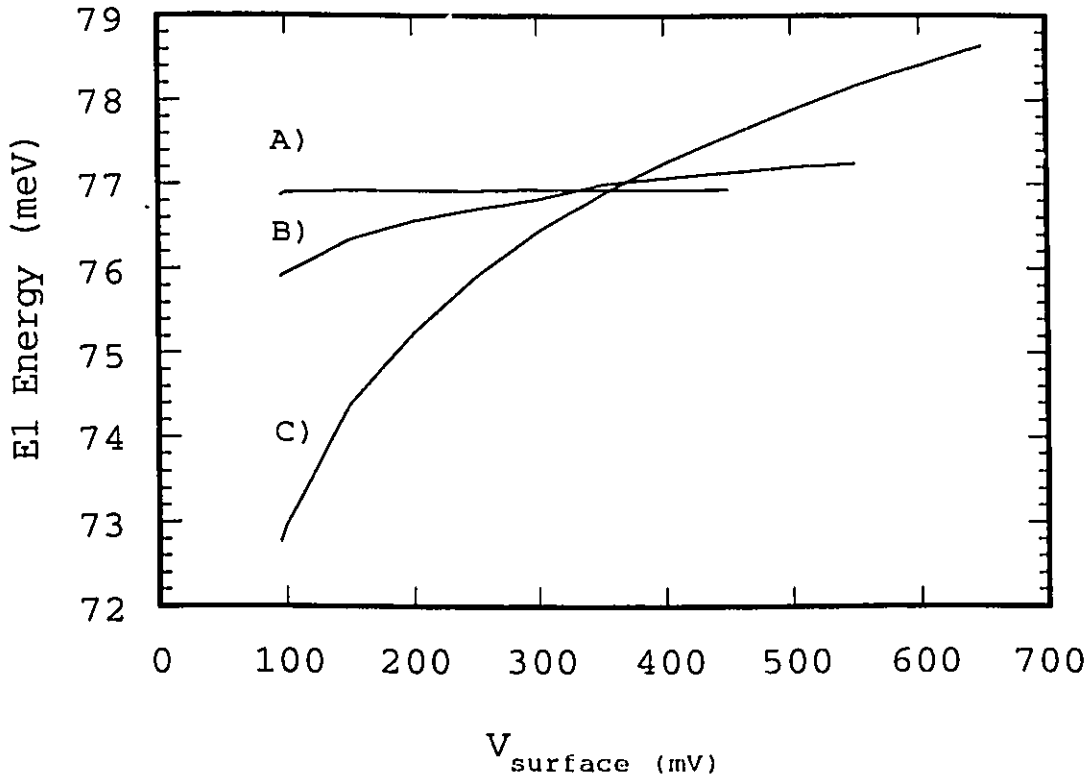

Figure 47. Calculated E1 quantum well eigenstate energy for the end quantum well as a function of the surface potential. A) 18 nm wide GaAs cap layer, B) 9 nm wide cap layer, C) 5 nm wide cap layer.

5-5 Tamm States

The atoms in the semiconductor beneath the surface, for the most part, form complete covalent bonding to their

neighbours. The surface atoms however are presented with a broken chain, resulting in dangling surface bonds. These dangling bonds can result in electronically active surface or Tamm states. In a similar fashion the $In_xGa_{1-x}As$-GaAs interface at each layer of the superlattice represents a surface which may result in active states. The Krönig-Penney model used in this thesis has assumed an ideal $In_xGa_{1-x}As$-GaAs interface. However, it is not unreasonable to expect the existence of electronic states localised at these interfaces. This surface state can be modelled as a potential added to the edge of the quantum wells as shown in figure 48. The potential profile for L121 was chosen for this calculation, where a 6 nm well width and 110 mV barrier potential are used. 0.1, 0.2, and 0.5 nm wide Tamm state potentials are included in the 6 nm well width, and the Tamm state depth is varied from -200 mV to 100 mV. The narrow Tamm state widths of 0.1 and 0.2 nm are perhaps physically plausible, but yield energy shifts to the E1 quantum well states of less than 4 meV (fig. 49 curves A and B). The effects of the wider 0.5 nm wide Tamm state approaches the effects of changing the well width by a monolayer (fig. 49 C).

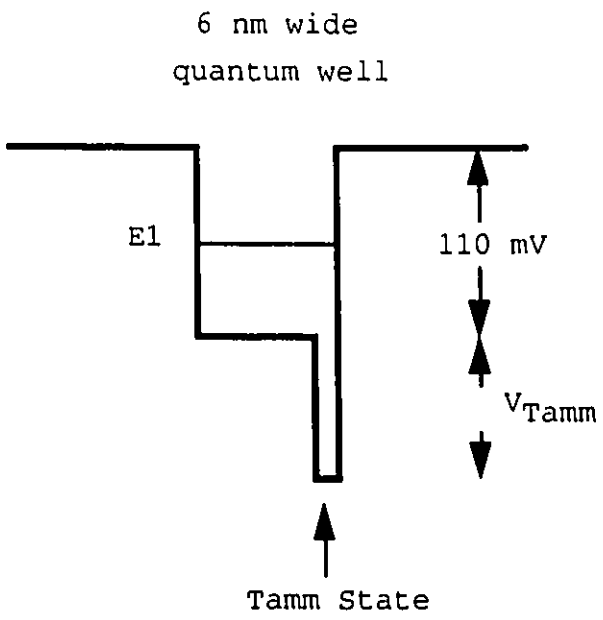

Figure 48. Potential profile used to calculate the effects of a Tamm state embedded at the $In_xGa_{1-x}As$-GaAs interface for L121.

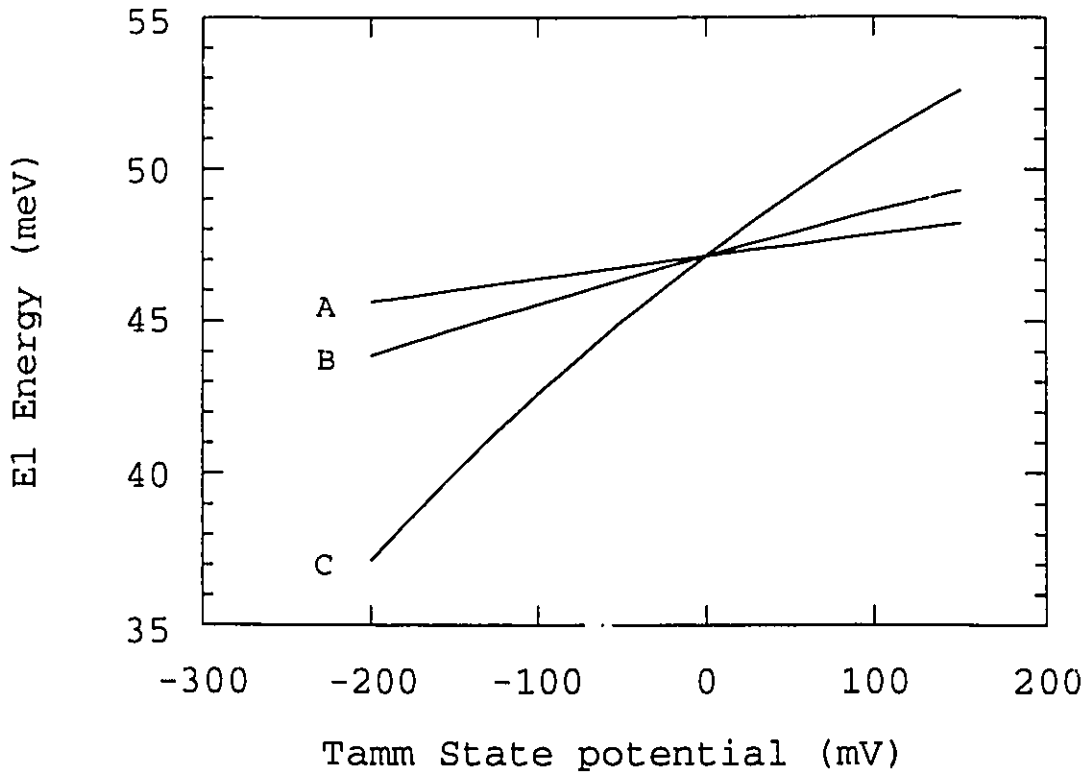

Figure 49. Effect of a Tamm state potential on the E1 quantum well energy for L121. A) 0.1 nm, B) 0.2 nm, C) 0.5 nm Tamm state width.

5-6 Summary

The calculations performed by Dignam and Sipe for the two samples H145 and L121 show good agreement with the measured photocurrent spectra. In particular, their model correctly predicts the field dependent exciton transition energies for the Stark ladders, the measured asymmetry in oscillator strengths between the plus and minus Stark ladders, as well as generating the observed anticrossings at weak fields.

This is a considerable improvement over the single particle calculations.

However their model failed to predict the structures A and A' observed in the photocurrent spectra for H145 and L121. Attempts at calculating these features as being due to end effects, Tamm states, or well width fluctuations, have also failed to generate these features. Hence, these two features are not understood at present.

Conclusions

The effects of a perturbing static electric field in the longitudinal or growth direction on a series of quantum wells and superlattices have been measured using photocurrent and electroreflectance spectroscopy. The application of an electric field to the single quantum well gives rise to a quadratic red shift of the lowest exciton transition energy E1H1, termed the 'quantum confined Stark effect' (QCSE). The magnitude of this effect is dependent upon the quantum well depth and width, and good agreement between experimental data and calculations for the QCSE is achieved, within the single particle model. Furthermore the field dependent reduction of exciton binding energy associated with the E1H1 exciton transition is measured and calculated, also showing good agreement.

The perturbation of the superlattice by an electric field generates a ladder like progression in eigenstate energies (Wannier Stark ladders) that vary linearly for applied fields greater than $5kVcm^{-1}$. The Stark ladders appear as distinct peaks in the photocurrent spectra, whose oscillator strengths vary with the degree of coupling between adjacent wells. L073 having a 46 meV miniband-width reveals up to 5 distinct Stark ladders, while L121 having a 16 meV miniband-width reveals 2 Stark ladders. The oscillator strengths for the positive index Stark ladders are observed to be greater than the minus Stark ladders for all three samples studied. The field dependence of the Stark ladders increases in complexity as the applied field is reduced to zero, with anticrossings being observed between the minus index Stark ladders.

Finally the two samples L121 and H145 reveal a distinct structure on the high energy side of the p=0 Stark ladder, whose origin is not known.

Electroreflectance data provided a means of measuring transitions above the GaAs bandedge, as well as observing several Stark ladder transitions at high applied fields which were not observed in the photocurrent spectra. The high field electroreflectance spectra exhibited a simple lineshape which is expected for isolated quantum wells, confirming the localization of the Stark ladder states. The weak field ER spectra was quite complex revealing a third derivative like behavior, indicating the interwell coupling expected for the superlattice under flatband conditions.

The overall good agreement between the tight-binding model or the numerically calculated interband Stark ladders, and the measured Stark ladders confirms the validity of these two approaches for electric fields greater than 5 $kVcm^{-1}$. The observed anticrossings between the minus Stark ladders, the asymmetry of the Stark ladder oscillator strengths, and the unidentified peaks A in the photocurrent spectra demonstrate that this is an incomplete description. This is further confirmed by the exciton Stark ladder calculations performed by Dignam and Sipe which reveal the formation of the anticrossings at weak fields, and the asymmetry of the Stark ladder oscillator strengths.

The observed peaks on the high energy side of the p=0 Stark ladders, labelled A, have been attributed to layer fluctuations between the quantum wells, and end effects due to the last well in the superlattice structure including Tamm

states. These effects have been modelled in this study, none of which has provided a convincing description of the observed photocurrent spectra. However, recent work by Ohno et al.[78], where the end wells of two $Al_xGa_{1-x}As$-GaAs superlattices were altered to simulate Tamm states, yielded distinct peaks in their photocurrent spectra. A similar study using $In_yGa_{1-x}As$-GaAs superlattices may indicate the origin of the peaks observed in the samples L121 and H145.

The weak field photocurrent spectra for the superlattices have revealed quite complex structures, especially the electroreflectance spectra. It would prove useful to simplify the experiment by incorporating fewer wells and barriers in the superlattice, thereby reducing the number of observed Stark ladder transitions at weak fields. This should simplify the analysis of the data with respect to the exciton Stark ladder calculations of Dignam and Sipe.

Finally, the strained quantum well and superlattice structures are of technological importance for the manufacture of high efficiency diode lasers, photodetectors and optical modulators.

References

1 E.E. Mendez, G. Bastard, L.L. Change, L. Esaki, M. Morkoc, R. Fischer, Phys. Rev. B. **26** 7101 (1982)

2 D.A.B. Miller, D.S. Chelma, T.C. Damen, A.C. Gossard, W. Wiegmann, T.H. Wood, C.A. Burrus, Phys. Rev. Lett. **56** 2173 (1984)

3 T.E. Van Eck, P. Chu, W.S.C. Chang, H.H. Wieder, Appl. Phys. Lett. **49** 135 (1986)

4 G.H. Wannier, Rev. Mod. Phys. **34** 645 (1962)

5 M. Saitoh, J. Phys. C: Solid State Phys. **5** 914 (1972)

6 H. Fukuyama, R. Bari, H.C. Fogedby, Phys. Rev. B **8** 5579 (1973)

7 F. Bentosela, V. Grecchi, F. Zironi, J. Phys. C: Solid State Phys. **15** 7119 (1982)

8 E.E. Mendez, F. Agullo-Rueda, J.M. Hong, Phys. Rev. Lett. **60** 2426 (1988)

9 J. Bleuse, P. Voisin, M. Allovon, M. Quillec, Appl. Phys. Lett. **53** 2632 (1988)

10 K. Fujiwara, Jap. J. Appl. Phys. **28** L1718 (1989)

11 B. Soucail, N. Dupuis, R. Ferreira, P. Voisin, A.P. Roth, D. Morris. K. Gibb, C. Lacelle, Phys. Rev. B. **41** 8568 (1990)

12 K. Gibb, C. Lacelle, A.P. Roth, B. Soucail, N. Dupuis, P. Voisin, B.Y. Hua, E. Fortin, Mat. Res. Soc. Symp. Proc. **160** 667 (1990)

13 G. Bastard Phys. Rev. B. **24** 5693 (1981)

14 F.H. Pollak, M. Cardona, Phys. Rev. **172** 816 (1968)

15 F.H. Pollak, Surf. Sci. **37** 863 (1973)

16 P.F. Yuh, K.L. Wang, Phys. Rev. B. **38** 13307 (1988)

17 G. Bastard "Wave Mechanics applied to Semiconductor Heterostructures" Monographies de Physique Les Editions

de Physique 1990

18 R.A. Smith "Wave Mechanics of Crystalline Solids" 2nd ed. Chapman-Hall Ltd. (1969)

19 L. Vina, E.E. Mendez W.I. Wang, L.L. Chang, L.Esaki, J. Phys. C: Solid State Phys. **20** 2803 (1987)

20 E.J. Austin, M. Jaros, Phys. Rev. B. **31** 5569 (1985)

21 E.J. Austin, M. Jaros, J. Phys. C: Solid State Phys. **18** L1901 (1985)

22 P.C. Klipstein, P.R. Tapster, N. Apsley, D.A. Anderson, M.S. Skolnick, T.M. Kerr, K. Woodbridge, J. Phys. C: Solid State Phys. **19** 857 (1986)

23 P.W.A McIlroy, J. Appl. Phys. **59** 3532 (1986)

24 D.C. Hutchings, Appl.Phys. Lett. **55** 1082 (1989)

25 M.G. Shorthose, J.F. Ryan, J. Phys: Condens. Matter. **1** 2041 (1989)

26 G. Bastard, E.E. Mendez, L.L. Chang, L. Esaki, Phys. Rev. B. **28** 3241 (1983)

27 D.A.B Miller, D.S. Chelma, T.C. Damen, A.C. Gossard, W. Wiegmann, T.H. Wood, C.A. Burrus, Phys. Rev. B. **32** 1043 (1985)

28 P. Voisin, J. Bleuse, C.Bouche, S. Gaillard, C. Alibert, A. Regreny, Phys. Rev. Lett. **61** 1639 (1988)

29 F. Agullo-Rueda, E.E. Mendez, J.M. Hong, Phys. Rev. B. **40** 1357 (1989)

30 D.M. Whittaker, M.S. Skolnick, G.W. Smith, C.R. Whitehouse, Phys. Rev. B. **42** 3591 (1990)
D.M. Whittaker, Superlattice and Microstruct. **7** 375 (1990)

31 D. Emin, C.F. Hart, Phys. Rev. B. **36** 7353 (1987)

32 P. Voisin, G. Bastard, M. Voos, Phys. Rev. B. **29** 935 (1984)

33 M.J. Bleuse "Effects electro-optiques dans les

superreseaux semiconducteurs" PhD thesis, Universite Pierre et Marie Curie, Dec. 21 (1988)

34 J. Bleuse, G. Bastard, P. Voisin, Phys. Rev. Lett. **60** 220 (1988)

35 M.M. Dignam, J.E. Sipe, Phys. Rev. Lett. **64** 1797 (1990)

36 M.M. Dignam J.E. Sipe, Phys. Rev. B. **43** 4097 (1991)

37 G. Bastard E.E. Mendez, L.L. Chang, L. Esaki, Phys. Rev. B. **26** 1974 (1982)

38 R.L. Greene, K.K. Bajaj, Solid State Commun. **45** 831 (1983)

39 R.L. Greene, K.K. Bajaj, D.E. Phelps, Phys. Rev. B. **29** 1807 (1984)

40 W. Trzeciakowski, A.P. Roth, Superlat. and Microstr. **6** 315 (1989)

41 H.Q. Hou, Y. Segawa, Y. Aoyagi, S. Namba, J.M. Zhou, Phys. Rev. B. **42** 1284 (1990)

42 J.A. Brum, G. Bastard, Phys. Rev. B. **31** 3893 (1985)

43 D.A.B. Miller, D.S. Chelma, T.C. Damen, A.C. Gossard, W. Wiegmann, T.H. Wood, C.A. Burrus, Phys. Rev. B. **32** 1043 (1985)

44 S. Hong, J. Singh, J. Appl. Phys. **61** 5346 (1987)

45 K. Gibb, A.P. Roth, Solid State Commun. **80** 811 (1991)

46 R.H. Yan, F. Laruelle,L.A. Coldren, Appl. Phys. Lett. **55** 2002 (1989)

47 M.M. Dignam, J.E. Sipe, Phys. Rev. B. **41** 2865 (1990)

48 B. Soucail, R. Ferreira, P. Voisin, A.P. Roth, D. Morris, K. Gibb, C. Lacelle, "20th International Conference on the Physics of Semiconductors". World Scientific. **2** 1501 (1990)

49 F. Iikawa, F. Cerdeira, C. Vazque-Lopez, P. Motisuke, M.A. Sacilotti, A.P. Roth, R. A. Masut, Phys. Rev. B. **38** 8473 (1988)

50 I. Bar Jospeph, C. Klingshirn, D.A.B. Miller, D.S. Chelma, V. Koren, B.I. Miller, Apply. Phys. Lett. **50** 1010 (1987)

51 R.T. Collins, K.V. Klitzing, K. Ploog, Phys. Rev. B. **33** 4378 (1986)

52 K. Yamanaka, T. Fukunaga, N. Tsukada, K.C.I. Kobashi, M. Ishii, Apply. Phys. Lett. **48** 840 (1986)

53 R.T. Collins, L. Vina, W.I. Wang, L.L. Chang, L. Esaki, K.V. Klitzing, K. Ploog, Phys. Rev. B. **36** 1531 (1987)

54 K. Gibb,C. Lacelle, Q. Sun, E. Fortin, A.P. Roth, Can. J. Phys. **69** 447 (1991)

55 P.W. Yu, G.D. Sanders, K.R. Evans, D.C. Reynolds, K.K. Bajaj, C.E. Stutz, R.C. Jones, Phys. Rev. B. **38** 7796 (1988)

56 P.W. Yu, G.D. Sanders, K.R. Evans, D.C. Reynolds, K.K. Bajaj, C.E. Stutz, R.C. Jones, Appl. Phys. Lett. **54** 2230 (1989)

57 L. Vina, R.T. Collins, E.E. Mendez, W.I. Wang, Phys. Rev. B. **33** 5939 (1986)

58 H.Q. Le, J.J. Zayhowski, W.D. Goodhue, Appl. Phys. Lett. **50** 1518 (1987)

59 K.Kohler, H.J. Polland, L. Schultheis, C.W. Tu, Phys. Rev. B. **38** 5496 (1988)

60 L. Vina, R.T. Collins, E.E. Mendez, W.I. Wang, Phys. Rev. Lett. **58** 832 (1987)

61 F.H. Pollak, O.J. Glembocki, SPIE. Spectroscopic Characterization Technologies for Semiconductor Technology III, **946** 2 (1988)

62 H. Shen, S.H. Pan, F.H. Pollak, R.N. Sacks, SPIE. Spectroscopic Characterization Technologies for Semiconductor Technology III, **946** 36 (1988)

63 P.C. Klipstein, P.R. Tapster, N. Apsley, D.A. Anderson,

M.S. Skolnick, T.M. Kerr, K. Woodbridge, J. Phys. C: Solid State Phys. **19** 857 (1986)

64 M. Nakayama, I. Tanaka, T. Doguchi, H. Nishimura, K. Kawashima, K. Fujiwara, Solid State Commun. **77** 303 (1991)

65 M. Nakayama, I. Tanaka, H. Nishimura, K. Kawashima, K. Fujiwara, Phys. Rev. B. **44** 5935 (1991)

66 Ladolt Bornstein "Numerical Data and Functional Relationships in Science and Technology" **22** (1988)

67 R. People, S.K. Sputz, Phys. Rev. B. **41** 8431 (1990)

68 M.J.C.S. Haines, N. Ahmed, S.J.A. Adams, K. Mitchel, I.R. Agool, C.R. Pidgeon, B.C. Cavenett, E.P. O'Reilly, A. Ghiti, M.T. Emeny, Phys. Rev. B. **43** 11944 (1991)

69 E. Fortin, B.Y. Hua, A.P. Roth,Phys. Rev. B. **39** 10887 (1989)

70 D. Coffey J. Appl. Phys. **63** 4626 (1988)

71 P.W. Yu, G.D. Sanders, K.R. Evans, D.C. Reynolds, K.K. Bajaj, C.E. Stutz, R.L. Jones. Appl. Phys. Lett. **54** 2230 (1989)

72 M.K. Saker, D.M. Whittaker, M.S. Skolnick, M.T. Emeny, C.R. Whitehouse, Superlattices and microstruct. **10** 295 (1991)

73 J.P. Hagon, M. Jaros, Phys. Rev. B. **41** 2900 (1990)

74 D.M. Whittaker, Superlattices and Microstruct. **7** 375 (1990)

75 H. Ohno, E.E. Mendez, J.A. Brum, J.M. Hong, F. Agullo-Rueda, L.L. Change, L. Esaki, Phys. Rev. Lett **64** 2555 (1990)

76 F.Y. Huang Appl. Phys. Lett. **57** 1669 (1990)

77 S.G.Tikhodeev, Solid State Commun. **78** 339 (1991)

78 H.Ohno, E.E. Mendez, A. Alexadrou, J.M. Hong, Surface Science **267** 161 (1992)